Nature of the Source Regions for Post-collisional, Potassic Magmatism in Southern and Northern Tibet from Geochemical Variations and Inverse Trace Element Modelling

H. M. WILLIAMS[1]*, S. P. TURNER[2†], J. A. PEARCE[3], S. P. KELLEY[1] AND N. B. W. HARRIS[1]

[1]DEPARTMENT OF EARTH SCIENCES, THE OPEN UNIVERSITY, WALTON HALL, MILTON KEYNES MK7 6AA, UK
[2]DEPARTMENT OF EARTH SCIENCES, WILLS MEMORIAL BUILDING, THE UNIVERSITY OF BRISTOL, BRISTOL BS8 1RJ, UK
[3]SCHOOL OF EARTH SCIENCES, CARDIFF UNIVERSITY, PO BOX 914, MAIN BUILDING, PARK PLACE, CARDIFF CF10 3YE, UK

RECEIVED JUNE 27, 2002; ACCEPTED AUGUST 4, 2003

Neogene potassic lavas in northern and southern Tibet have different isotopic ($\varepsilon Nd_{(i)}$ north, −5·5 to −10·3; south −8·8 to −18·1) and major element signatures suggesting derivation from separate sub-continental lithospheric mantle (SCLM) sources. Inverse trace-element modelling shows that the southern Tibet magmas were derived by 1–2% partial melting of a phlogopite and amphibole peridotite, and that the northern samples were derived by 3–4% partial melting of a phlogopite peridotite. In both cases, melting is inferred to take place in the spinel stability field. Both sources show large ion lithophile element (LILE) enrichment relative to the high field strength elements (HFSE), and heavy rare earth element (HREE) depletion relative to primitive mantle. LILE/HFSE enrichment suggests subduction-related metasomatism; HREE depletion is indicative of prior melt extraction. Extension postdates the earliest magmatism in southern and north–central Tibet by 7 Myr and 5 Myr, respectively, which, in combination with the shallow depths of melting inferred for the Tibetan samples, supports geodynamic models invoking thinning of the SCLM. The northern Tibetan magmatism and extension can be explained by convective removal of the lower SCLM; the older ages and arcuate distribution of the southern magmas are most consistent with the SCLM erosion following slab break-off.

KEY WORDS: *Tibet; lithospheric mantle; magmatism; extension*

INTRODUCTION

The processes responsible for the elevation history of the Tibetan plateau and its continuing east–west extension, orthogonal to the direction of the plate convergence between India and Eurasia, are not well understood. The onset of this extension, in the Miocene, has been inferred by several workers (Turner *et al.*, 1996; Miller *et al.*, 1999; Blisniuk *et al.*, 2001; Williams *et al.*, 2001) to have been associated with Neogene potassic and calc-alkaline magmatism and thus to be related to the process of convective removal of sub-continental lithospheric mantle (SCLM), which is triggered by distributed shortening (Houseman *et al.*, 1981). This model predicts that the Tibetan plateau will be elevated to levels unsustainable by the local boundary forces, and that the plateau will subsequently extend and collapse, resulting in an association between potassic magmatism and extension that is synchronous with, or post-dates, such magmatism (Turner *et al.*, 1992; Platt & England, 1994). In this

*Corresponding author. Present address: ETH-Zürich, Sonneggstrasse 5, CH-8092 Zürich, Switzerland. Telephone: +41 1 632 5983. Fax: +41 1 632 1080. E-mail: williams@erdw.ethz.ch
†Present address: Department of Earth and Planetary Sciences, Macquarie University, Sydney, N.S.W. 2109, Australia

Journal of Petrology 45(3)

model, a substantial part of the lower SCLM has been removed, so the prediction of the model, that melting will take place at the base of the thinned SCLM, requires mantle melting to be relatively shallow (<100 km), although this depends on the original lithospheric thickness and the amount of shortening (Platt & England, 1994). The significance of this model is that, if it is correct, the age distribution of potassic magmatism on the Tibetan plateau can be used to constrain the timing of plateau uplift, and potentially address the validity of models that link Cenozoic climate change to the uplift of the Tibetan plateau (Harrison *et al.*, 1993; Molnar *et al.*, 1993).

However, the convective removal model has been called into question because it does not explain the heterogeneous temporal and spatial distribution of the magmatism across the Tibetan plateau and there are a number of competing models for the geodynamic evolution of the Tibetan plateau that allow for the generation of potassic magmatism and, in some cases, associated extension. These include slab break-off and the creation of a 'slab window' between the broken off part of the slab and the overriding lithosphere (Davies & von Blanckenburg, 1995; Chemenda *et al.*, 2000); delamination, i.e. the wholesale removal or 'peeling off' of mantle lithosphere beneath the Tibetan plateau (Bird, 1979); southward-dipping continental subduction (Arnaud *et al.*, 1992; Tapponnier *et al.*, 2001) at the northern margin of the Tibetan plateau; and shear heating (Kincaid & Silver, 1996).

All the above models make certain predictions concerning the spatial and temporal distribution of 'post-collisional' potassic magmatism on the Tibetan plateau (here and in the rest of this paper we use the term 'collisional' to refer to the initial contact between the Indian and Asian plates and not to refer to the continuing process of plate convergence), the duration and conditions of partial melting (e.g. pressure, temperature, degrees of melting) and the nature and location of the magma source regions in the mantle lithosphere and/or the crust. The objectives of this paper are to place further constraints on the timing, the melting regimes and the nature of the source regions for the post-collisional volcanics and intrusives from northern and southern Tibet, and to evaluate these data in the light of the current geodynamic models for the evolution of the Tibetan plateau.

We present new data for suites of post-collisional volcanic and intrusive rocks from northern and southern Tibet. The southern Tibet samples include new samples in addition to those of Arnaud (1992), Arnaud *et al.* (1992) and Williams *et al.* (2001); the northern Tibet samples are those of Turner *et al.* (1996), which were reanalysed for their trace element concentrations. Additional Sr, Nd and Pb isotope analyses are presented for selected samples from the collection of Turner *et al.* (1996), to extend the isotopic dataset. New isotope and trace element data are presented for northern Tibetan samples from the collections of Pearce & Mei (1988) and Deng (1991). Combined with the data of Miller *et al.* (1999) for SW Tibet, the collection of samples studied here spans the major lithospheric terranes (Lhasa, Qiangtang, Kunlun and Songpan–Ganze) of Tibet (Fig. 1), and probably represents one of the most comprehensive suites at present available.

SAMPLE DESCRIPTIONS AND LOCATIONS

The volcanics and intrusives are distributed widely across Tibet and its major lithospheric terranes (Fig. 1). Eruptive centres and volcanic units range from cinder cones and pyroclastic deposits in the north-western regions of the plateau (Liu & Maimaiti, 1989; Deng, 1991; Arnaud *et al.*, 1992) to sequences of lava flows, pyroclastic deposits and dykes (Coulon *et al.*, 1986; Arnaud, 1992; Turner *et al.*, 1996; Miller *et al.*, 1999; Williams *et al.*, 2001) in the south. The total volume of post-collisional magmatism across the plateau is unknown, but appears to be substantial in some individual localities, e.g. 200–300 km^3 for centres in NW Tibet (Liu & Maimaiti, 1989; Deng, 1991) and 80–120 km^3 for individual localities in SW Tibet (R. Schuster, personal communication, 1999). Most samples are Miocene in age, ranging from 10 to 25 Ma in the south and 19 Ma to the present day in northern Tibet (Coulon *et al.*, 1986; Liu & Maimaiti, 1989; Deng, 1991, 1997; Arnaud, 1992; Arnaud *et al.*, 1992; Turner *et al.*, 1993, 1996; Chung *et al.*, 1998; Miller *et al.*, 1999). Magmatism in the eastern parts of the Tibetan plateau is older, 29–41 Ma (Chung *et al.*, 1998). New ^{40}Ar–^{39}Ar ages obtained for volcanics in southern and northern Tibet (Table 1; the full data are reported in an Electronic Appendix at http://www.petrology.oupjournals.org), confirm this pattern.

Lavas from the north of the plateau (Fig. 1; the Qiangtang, Songpan–Ganze and Kunlun terranes) have variable geochemical, mineralogical and textural characteristics (Deng, 1991; Turner *et al.*, 1996; Hacker *et al.*, 2000). The more mafic samples, which include rocks from the Tienchuhai, Ashikule and Heishibei areas, have olivine, orthopyroxene, clinopyroxene and phlogopite phenocrysts in a microcrystalline matrix (Arnaud *et al.*, 1992; Turner *et al.*, 1996). More evolved samples, such as those from the Dogai Coring area, have alkali feldspar and biotite as phenocryst phases in a quartz–feldspar groundmass (Turner *et al.*,

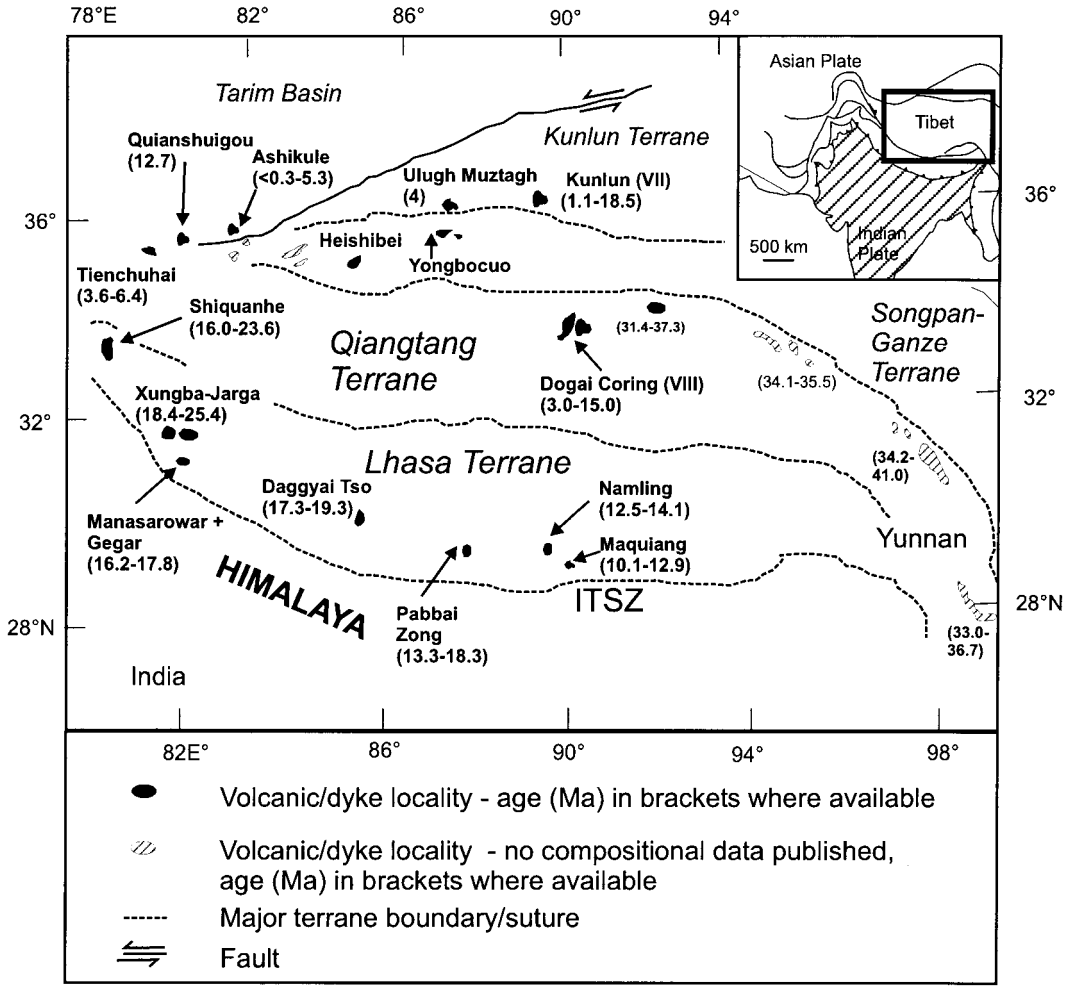

Fig. 1. Simplified map of the Tibetan plateau, showing the boundary between Indian and Asian lithosphere (the Indus–Tsangpo Suture Zone; ITSZ), other terrane boundaries and major faults. The terrane boundaries are from Dewey (1988). Volcanic localities known at present (Coulon *et al.*, 1986; Liu & Maimaiti, 1989; Wanming, 1991, 1997; Arnaud, 1992; Arnaud *et al.*, 1992; Turner *et al.*, 1993, 1996; Chung *et al.*, 1998; Miller *et al.*, 1999) are shown as fields; a black field denotes a locality for volcanics for which geochemical data are available, a hatched field indicates a reported volcanic locality for which geochemical data are not yet available, although, in some cases, geochronological data have been published in the absence of geochemical data. The inset shows the position of the Tibetan Plateau with respect to that of the Indian subcontinent.

1996). Samples from SW Tibet (Lhasa terrane, Fig. 1) have phlogopite and pyroxene phenocrysts within a microcrystalline groundmass. The exceptions are ultrapotassic dykes from the Pabbai Zong area (Lhasa terrane, Fig. 1), which have >40 modal % phlogopite phenocrysts and subordinate clinopyroxene within a microcrystalline matrix (Williams *et al.*, 2001). More evolved samples are characterized by the presence of alkali feldspar and either hornblende or biotite phenocrysts in quartz–feldspar microcrystalline matrix.

ANALYTICAL TECHNIQUES

^{40}Ar–^{39}Ar isotope analyses (Table 1) were performed at the Open University (OU), UK, using a focused IR Nd–YAG (wavelength 1064 nm) laser and automated gas extraction system. Argon isotopes were measured using a MAP 215-50 noble gas mass spectrometer, following techniques outlined by Kelley (1995). Ages were calculated using standard isochron linear least-squares regression techniques, although in cases where there was insufficient spread in the data array, the *y*-intercept was set at the atmospheric value of $^{36}Ar/^{40}Ar$. In these cases, the ages calculated are minima. Errors were multiplied by the square root of the mean square weighted deviation (MSWD), where the latter was greater than 2·5. The ages were determined relative to the biotite standard GA1550, which has an age of 98·8 Ma (Renne *et al.*, 1998).

Table 1: ^{40}Ar–^{39}Ar ages for southern and northern Tibetan lavas

Sample and location		TAS rock classification	Mineral	Data points	MSWD	Age (Ma) ± 2 SD	$^{40}Ar/^{36}Ar$ ± 2 SD
Southern Tibet							
JPT 3*	Namling Basin	andesite	bi	9 of 9	1·34	13·9 ± 0·1	295·5
JPT 5.2*	Namling Basin	dacite	bi	8 of 8	2·52	12·5 ± 0·3	295·5
JPT 8	Namling Basin	rhyolite	bi	10 of 10	5·41	13·8 ± 4·6	1178 ± 144
JPT 14.1*	Daggyai Tso	trachyte	phl	14 of 14	5·91	18·8 ± 0·5	295·5
JPT24C	Shiquanhe	trachyandesite	phl	12 of 12	1·39	24·0 ± 1·0	369 ± 117
JPT24B	Shiquanhe	trachyandesite	phl	9 of 9	1·25	22·3 ± 4·7	408 ± 205
JPT 23	Shiquanhe	megacrysts†	phl	min of 7	n.a.	21·2 ± 0·6	295·5
Northern Tibet							
Bb124	Quianshuigou	basaltic trachyandesite	phl	7 of 7	0·8	12·8 ± 2·2	269 ± 127
Norin 1105	Ashikule	trachyandesite	WR	min of 8	1·2	5·0 ± 0·5	295·5
Norin 912	Ashikule	trachyandesite	WR	min of 10	1·2	2·7 ± 1·8	295·5

phl, phlogopite; bi, biotite; WR, whole rock; min, minimum individual crystal fusion age, age calculated assuming that any initial argon present was atmospheric in composition; n.a., not analysed.
*Regression forced through atmospheric argon.
†No whole-rock data available, megacrysts were taken from clast of mafic extrusive rock entrained within an igneous agglomerate, with a matrix of fine-grained phlogopite, quartz and feldspar.

Major element and Cr concentrations were determined by X-ray fluorescence (XRF) spectrometry at the OU. Analyses were performed on fused discs and powder pellets following Potts *et al.* (1984). Trace element concentrations for the majority of samples were determined by inductively coupled mass spectrometry (ICP-MS) at Durham University, UK. Powders were dissolved using a standard HF–HNO_3 technique, and spiked with Rh, In and Bi before dilution to 3·5% HNO_3. Solutions were analysed on a Perkin–Elmer–SCIEX Elan 6000 inductively coupled plasma mass spectrometer using a cross-flow nebulizer. Appropriate corrections were made using oxide/metal ratios measured on matrix-matched standard solutions; oxide interferences were minimal for most analyses. Total procedural blanks for all elements were negligible. Reproducibility, based on repeated analyses of samples and standards, was between 1 and 3% for most elements, and analysed standard (BHVO-1, AGV-1) values deviated less than 2% from published values. The new major and trace element data are presented in Table 2.

Sr and Nd isotope analyses were performed by multi-collector inductively coupled mass spectrometry (MC-ICP-MS) on a Nu Instruments machine (OU) and by thermal ionization mass spectrometry (TIMS) on Finnigan MAT 261 and 262 machines (OU), and on the VG sector 54 system at the University of Cambridge, UK. Following dissolution using standard HF–HNO_3 techniques, Sr and rare earth elements (REE) fractions were separated using cationic ion-exchange resin columns. Nd was separated from the REE fraction using hydrogen-diethyl-hexyl-phosphate (HDEHP) columns (Richard *et al.*, 1976). Sr and Nd procedural blanks were $<0·8$ ng and $<0·3$ ng, respectively. The collected Sr and Nd fractions were evaporated and dissolved in 2% HNO_3 to give solutions for analysis by MC-ICP-MS, or were loaded (Nd in HNO_3, Sr in H_2O and 10% H_3PO_4) onto outgassed Ta filaments for TIMS.

For Sr and Nd isotope analysis by MC-ICP-MS, sample solutions were desolvated and introduced into the plasma torch using a Cetac Aridus nebulizer. The system was cleaned between analyses by aspirating 2% HNO_3 through the nebulizer for ~15 min. All analyses were carried out in static multi-collector mode. At the end of each analytical session, 2% HNO_3 and IPA (isopropyl alcohol) were alternately aspirated through the nebulizer. Peak integration times were 10 s for Sr, 8 s for Nd; baselines were collected for twice these integration times at half mass.

Ten measurements were made per block of ratios; 20 blocks were collected for Sr, 10 for Nd. The average values and errors (2 SD) of repeat analyses of the NBS 987 Sr standard and the Johnson and Matthey Nd standard during the different periods of analysis are given in Table 3. We normalized our sample Sr isotope data to our value of NBS 987 by first iteratively correcting our NBS 987 value to the accepted value of 0·710230. This gives a $^{86}Sr/^{88}Sr$ specific to the period of analysis, which is then used to normalize the sample

Table 2a: Whole-rock major and trace element compositions, southern Tibet

Sample:	JPT24A	JPT24B	JPT24C	JPT22	K89G162	20E39A	JPT7	T5B/98	JPT14.1	JPT3	JPT4	JPT5.2	JPT8	95RAS11.3	T2A	T3B	T4A	T5A
TAS classification:	TrA	TrA	TrA	Tr	Tr	Tr	TrA	dacite	Tr	andesite	dacite	dacite	rhyolite	dacite	PhT	TrA	PhT	TrA
Group:	S.-W.	S.-W.	S.-W.	S.-W.	S.-W.	S.-W.	P.Z.	P.Z.	S.-C.	S.-C.	S.-C.	S.-C.	S.-C.	S.-C.	P.Z.	P.Z.	P.Z.	P.Z.
Locality:	Shiquanhe	Shiquanhe	Shiquanhe	Shiquanhe	Shiquanhe	Shiquanhe	P.Z.	P.Z.	Daggyai Tso	Namling	Namling	Namling	Namling	Namling	P.Z.	P.Z.	P.Z.	P.Z.
Major element data are normalized to 100%																		
SiO_2	65·6	58·1	57·7	69·2	65·3	63·2	61·9	68·7	63·2	64·7	70·3	67·6	75·3	75·9	53·1	58·3	54·5	61·8
TiO_2	0·8	1·1	1·1	0·6	0·8	0·9	0·8	0·8	0·7	0·7	0·4	0·6	0·4	0·3	1·0	1·1	1·1	0·7
Al_2O_3	14·6	12·9	12·8	15·5	14·6	15·3	12·2	12·8	16·6	15·7	16·2	16·4	15·1	13·3	11·4	14·9	14·5	12·1
Fe_2O_3*	3·9	5·6	5·8	2·9	3·5	7·5	4·8	4·4	4·3	4·9	2·0	3·2	2·1	1·6	6·7	7·0	6·4	4·5
MnO	0·1	0·1	0·1	0·1	0·1	0·1	0·1	0·1	0·1	0·2	0·0	0·0	0·0	0·0	0·1	0·1	0·1	0·1
MgO	2·8	5·4	6·0	1·5	2·3	1·9	4·6	3·9	3·0	1·3	0·8	1·5	0·6	0·8	11·8	5·4	7·2	4·7
CaO	4·3	7·7	7·6	2·7	2·9	3·1	7·6	1·8	4·8	4·6	2·8	4·8	0·4	4·2	5·5	3·9	6·1	7·7
Na_2O	2·7	2·3	2·3	3·0	3·1	4·2	2·0	1·6	4·1	3·2	3·4	0·9	0·8	1·1	1·2	2·2	2·3	2·2
K_2O	4·8	5·9	5·9	4·3	7·4	3·5	5·4	5·2	2·9	4·6	4·1	4·7	5·2	2·5	8·0	6·2	6·9	5·5
P_2O_5	0·4	0·7	0·7	0·2	n.d.	0·3	0·7	0·8	0·2	0·3	0·1	0·2	0·2	0·1	1·3	0·8	1·0	0·7
Mg no.†	64	70	72	56	62	38	70	69	63	39	49	53	40	57	81	66	74	72
LOI	2·5	3·1	2·8	2·3	2·1	2·4	6·6	3·6	0·6	3·2	2·5	8·1	3·1	5·0	2·5	3·3	4·1	7·4
Sc	9·5	14·4	14·0	7·7	6·0	24·8	9·7	10·6	7·6	6·4	2·3	4·8	2·6	1·6	14	16	15	10
V	76·7	118·0	111·6	60·9	62·5	65·3	73·1	71·1	77·4	73·9	31·3	61·3	26·4	15·7	105	125	115	78
Cr	142·7	351·0	354·0	59·0	59·0	10·0	270·0	241·0	129·0	31·4	41·0	13·0	50·0	17·0	649	186	275	219
Co	16·0	30·4	27·6	9·0	9·7	32·4	19·5	15·0	14·4	11·3	3·7	8·6	3·7	3·1	36	25	26	19
Ni	71·9	195·5	180·1	n.d.	n.d.	3·9	111·7	109·5	54·0	19·5	15·2	4·8	30·4	9·9	467	105	150	114
Cu	18·8	39·2	40·8	n.d.	n.d.	n.d.	31·0	34·5	n.d.	n.d.	n.d.	n.d.	n.d.	n.d.	73	63	62	31
Zn	71·7	76·9	71·3	n.d.	n.d.	n.d.	39·6	40·9	n.d.	n.d.	n.d.	n.d.	n.d.	n.d.	76	72	69	41
Ga	23·8	18·8	18·1	26·8	20·4	16·3	12·7	14·4	21·4	17·7	16·3	19·0	18·9	11·2	16	18	20	13
Rb	359·9	462·2	438·2	326·5	540·7	66·7	257·8	276·0	91·0	116·2	146·8	206·2	314·6	70·6	642·6	325·6	398·0	283·9
Sr	372·2	733·4	723·7	221·5	574·8	659·8	715·6	469·8	949·2	802·9	651·2	471·7	158·2	3352·5	920·5	1114·6	694·1	767·5
Y	21·6	26·8	25·5	19·9	18·1	26·1	21·3	23·1	11·2	11·0	4·8	7·4	4·5	7·1	36·3	35·8	26·7	22·3
Zr	263·3	400·8	377·2	206·7	154·4	182·5	238·8	269·1	109·1	122·3	27·4	78·8	47·4	50·7	323	367·9	482·4	253·4
Nb	18·5	28·8	27·2	14·4	33·5	11·8	13·6	15·4	8·1	4·7	6·3	14·2	5·8	18·6	20·3	23·7	14·4	
Ba	1002·5	1725·8	1639·7	711·3	1321·7	948·0	1877·7	1535·1	846·5	914·4	760·5	1060·3	963·1	877·1	4220·7	2695·7	2735	1593·5
La	68·3	62·5	58·6	73·5	110·2	49·3	54·3	56·8	34·1	30·9	22·8	33·3	22·3	26·8	145·8	95·9	134·3	56·4
Ce	147·1	146·8	138·5	152·2	232·7	97·6	116·3	127·0	65·3	63·5	41·7	66·0	88·9	51·3	314·8	198·9	179·7	123·5
Pr	18·7	21·2	20·1	18·1	29·7	12·1	15·4	16·5	7·9	7·8	4·8	8·0	3·5	5·6	40·7	25·1	40·5	47·0
Nd	73·4	94·8	90·2	65·6	117·5	48·5	64·1	67·7	30·1	31·1	17·0	30·0	11·4	19·4	167·1	101·6	164·9	67·0

Table 2a: continued

Sample:	JPT24A	JPT24B	JPT24C	JPT22	K89G162	20E39A	JPT7	T5B/98	JPT14.1	JPT3	JPT4	JPT5.2	JPT8	95RAS11.3	T2A	T3B	T4A	T5A
TAS classification:	TrA	TrA	TrA	Tr	Tr	Tr	TrA	dacite	Tr	andesite	dacite	dacite	rhyolite	dacite	PhT	TrA	PhT	TrA
Group:	S.-W.	S.-W.	S.-W.	S.-W.	S.-W.	S.-W.	P.Z.	P.Z.	S.-C.	S.-C.	S.-C.	S.-C.	S.-C.	S.-C.	P.Z.	P.Z.	P.Z.	P.Z.
Locality:	Shiquanhe	Shiquanhe	Shiquanhe	Shiquanhe	Shiquanhe	Shiquanhe	P.Z.	P.Z.	Daggyai Tso	Namling	Namling	Namling	Namling	Namling	P.Z.	P.Z.	P.Z.	P.Z.
Sm	13·2	20·3	19·2	10·3	18·5	8·6	11·3	12·1	4·9	5·3	2·6	4·7	1·6	2·9	30·1	18·1	27·2	11·9
Eu	1·9	3·2	3·1	1·3	3·0	2·2	2·0	2·2	1·2	1·2	0·6	1·0	0·4	0·5	5·3	3·5	4·5	2·2
Gd	8·1	12·2	11·7	6·4	10·4	6·7	7·4	8·0	3·6	3·7	1·8	3·1	1·1	2·0	19·9	12·7	15·8	7·9
Tb	0·9	1·3	1·2	0·8	1·0	0·9	0·9	0·9	0·4	0·4	0·2	0·3	0·1	0·2	2·0	1·5	1·5	0·9
Dy	4·2	5·6	5·2	3·7	4·1	4·8	4·1	4·3	2·1	2·1	0·9	1·5	0·7	1·2	8·2	7·1	5·9	4·2
Ho	0·7	0·9	0·8	0·7	0·6	0·9	0·7	0·8	0·4	0·4	0·2	0·2	0·1	0·2	1·1	1·2	0·9	0·7
Er	1·8	2·2	2·1	1·7	1·4	2·3	1·8	2·0	1·0	0·9	0·4	0·6	0·4	0·6	2·7	3·0	2·1	1·8
Tm	0·3	0·3	0·3	0·3	0·2	0·3	0·2	0·3	0·1	0·1	0·1	0·1	0·1	0·1	0·4	0·4	0·3	0·3
Yb	1·7	2·0	1·9	1·6	1·1	2·1	1·6	1·7	0·8	0·8	0·4	0·5	0·6	0·6	2·1	2·6	1·6	1·6
Lu	0·2	0·3	0·3	0·2	0·1	0·3	0·2	0·3	0·1	0·1	0·1	0·1	0·1	0·1	0·3	0·4	0·2	0·2
Hf	7·5	10·7	10·2	6·1	6·0	4·7	6·4	7·2	3·1	3·5	1·2	2·5	2·1	1·9	8·4	9·6	12·5	6·9
Ta	1·4	1·9	1·8	1·2	2·0	0·8	0·7	0·8	0·6	0·7	0·4	0·5	1·2	0·5	1·0	1·3	1·3	0·8
Pb	43·7	47·3	44·5	43·6	113·8	21·0	50·6	49·0	28·4	33·0	36·5	44·2	60·5	41·2	10·3	52·7	59·6	47·0
Th	54·0	86·2	81·6	40·4	135·9	19·1	75·0	84·1	16·0	19·3	16·4	23·9	56·2	17·8	118·0	68·3	146·7	78·3
U	11·3	18·2	17·2	8·3	11·0	1·6	13·2	14·1	2·7	3·7	3·7	2·2	8·1	4·7	13·6	10·4	21·2	13·9

Table 2b: Whole-rock major and trace element compositions, northern Tibet

Sample:	912	1105	K702	K703	K89G185	K89G186	K89G200	KP 12.6	KP47-2	KP47-5	Bb 124	Bb121	Bq137	Bb119	Bb122
TAS classification:	TrA	TrA	BTrA	BTrA	PhT	PhT	TrA	TrA	PhT	BTr	TrA	TrA	TrA	Tr	Tr
Group:	N.-W.	N.-W.	N.-W.	N.-W.	N.-W.	N.-W.	N.-W.	N.-W.	N.-W.	N.-W.	N.-W.	N.-W.	N.-W.	N.-W.	N.-W.
Locality:	Ash	Ash	Ash	Ash	Tien	Tien	Tien	Hei	Hei	Hei	Qiang	Qiang	Qiang	Qiang	Qiang
SiO_2	58·2	62·7	53·2	56·4	52·0	52·1	57·0	61·4	52·5	54·5	59·7	60·6	63·5	62·6	63·9
TiO_2	1·8	0·7	1·9	2·0	1·8	1·9	1·4	2·0	1·6	1·6	1·3	1·5	1·5	1·6	1·5
Al_2O_3	14·3	15·1	13·9	14·9	14·3	14·8	13·9	13·8	14·5	14·3	14·7	15·1	15·2	14·5	14·5
Fe_2O_3*	7·2	6·0	7·2	7·9	9·5	9·7	7·4	7·2	7·6	8·9	5·9	7·2	5·6	7·3	5·8
MnO	0·1	0·1	0·2	0·1	0·1	0·1	0·1	0·1	0·1	0·1	0·1	0·1	0·1	0·1	0·1
MgO	4·3	1·9	4·3	4·0	5·8	4·1	4·4	2·0	4·1	4·4	2·9	2·7	3·8	1·4	1·8
CaO	5·6	5·4	10·9	6·4	7·5	7·7	6·4	5·7	9·8	7·4	7·5	4·9	1·8	3·4	5·2
Na_2O	2·6	3·2	3·0	2·9	4·0	4·7	4·0	3·0	4·6	3·5	3·3	3·4	3·6	4·1	3·1
K_2O	5·0	4·3	3·8	4·1	4·9	4·8	5·4	4·0	4·2	4·3	3·8	3·8	4·3	3·7	4·1
P_2O_5	1·1	0·7	1·7	1·2	n.d.	n.d.	n.d.	0·9	1·1	0·9	0·7	0·7	0·7	1·3	0·1
Mg no.†	60	43	60	56	60	51	60	41	57	55	55	49	62	32	43
LOI	0·0	n.d.	2·4	1·1	4·2	2·1	0·32	0·8	2·2	2·6	1·9	1·0	0·3	0·5	n.d.
Sc	10·7	14·0	10·3	11·1	9·9	9·7	9·1	7·0	19·0	16·0	8·1	8·1	5·9	6·6	7·1
V	105·7	95·1	98·8	106·9	135·3	128·1	105·5	71·2	162·0	169·0	82·3	80·1	71·8	73·6	74·5
Cr	82·7	184·1	57·0	87·0	88·0	122·0	83·0	25·5	125·0	79·0	73·4	73·4	25·1	29·3	27·7
Co	15·5	15·1	19·5	19·4	31·0	31·9	20·7	13·4	n.d.	n.d.	14·3	12·8	8·8	8·4	9·4
Ni	29·9	31·1	50·9	43·3	68·9	69·2	68·8	11·0	60·0	87·0	33·1	31·2	7·6	6·9	8·9
Cu	22·8	n.d.	34·1	26·1	31·7	29·2	18·2	n.d.	n.d.	n.d.	21·4	19·9	11·9	n.d.	n.d.
Zn	104·2	n.d.	113·2	126·0	119·7	111·1	114·4	n.d.	n.d.	n.d.	144·6	176·9	106·6	n.d.	n.d.
Ga	22·4	16·6	19·5	22·2	21·7	20·5	21·4	24·6	n.d.	n.d.	22·4	22·0	22·5	22·9	22·0
Rb	236·0	123·7	113·9	126·3	132·4	121·9	207·9	182·3	103·0	144·0	144·5	122·5	173·4	175·7	162·0
Sr	1387·4	296·4	1216·6	1176·6	2120·2	1967·7	1682·2	813·1	1621·0	1562·0	1134·9	1065·0	905·6	921·3	933·5
Y	27·4	24·9	28·1	31·7	32·0	27·6	24·4	30·1	n.d.	n.d.	23·0	20·9	20·5	22·3	20·1
Zr	600·1	72·0	432·5	532·0	451·9	451·7	327·6	572·9	348·0	399·0	524·8	500·2	484·7	565·9	596·9
Nb	45·1	14·2	43·6	49·5	42·3	39·3	36·0	63·5	n.d.	n.d.	38·1	36·8	37·3	37·6	35·8
Ba	2429	599	2133	2131	2854	2697	2287	1649	n.d.	n.d.	1844	1788	1923	2002	1968
La	141·2	36·1	153·0	177·6	190·2	178·6	162·9	173·0	154·0	165·0	160·0	152·4	186·1	204·8	184·2
Ce	285·7	69·1	275·0	318·3	373·4	349·0	310·4	337·0	287·5	304·0	302·7	286·9	347·5	377·4	341·7
Pr	33·3	7·8	35·4	40·9	43·6	40·4	34·8	38·7	n.d.	n.d.	32·7	31·4	36·8	39·3	36·1
Nd	123·3	29·3	129·9	148·5	163·8	150·2	126·7	139·7	108·0	113·5	112·7	109·3	123·7	134·8	121·3
Sm	18·1	5·5	18·8	21·3	23·3	21·4	18·0	19·9	17·3	19·4	14·9	14·7	15·8	16·9	15·5

Table 2b: continued

Sample:	912	1105	K702	K703	K89G185	K89G186	K89G200	KP 12.6	KP47-2	KP47-5	Bb 124	Bb121	Bq137	Bb119	Bb122
TAS classification:	TrA	TrA	BTrA	BTrA	PhT	PhT	TrA	TrA	PhT	BTr	TrA	TrA	TrA	Tr	Tr
Group:	N.-W.	N.-W.	N.-W.	N.-W.	N.-W.	N.-W.	N.-W.	N.-W.	N.-W.	N.-W.	N.-W.	N.-W.	N.-W.	N.-W.	N.-W.
Locality:	Ash	Ash	Ash	Ash	Tien	Tien	Tien	Hei	Hei	Hei	Qiang	Qiang	Qiang	Qiang	Qiang
Eu	3·9	1·1	3·9	4·5	5·1	4·7	3·9	3·6	3·7	4·4	3·1	3·1	3·1	3·1	3·0
Gd	12·1	5·0	13·3	15·1	15·6	14·2	11·8	13·8	n.d.	n.d.	10·3	9·8	10·2	11·3	10·0
Tb	1·3	0·7	1·4	1·6	1·6	1·5	1·2	1·5	1·4	1·5	1·1	1·1	1·1	1·2	1·0
Dy	5·6	4·2	6·0	6·9	6·9	6·2	5·2	6·4	n.d.	n.d.	4·7	4·4	4·4	4·8	4·3
Ho	0·9	0·8	1·0	1·1	1·1	0·9	0·8	1·0	n.d.	n.d.	0·8	0·7	0·7	0·8	0·7
Er	2·2	2·3	2·3	2·6	2·5	2·2	1·9	2·3	n.d.	n.d.	1·8	1·7	1·6	1·7	1·6
Tm	0·3	0·4	0·3	0·4	0·3	0·3	0·2	0·3	n.d.	n.d.	0·2	0·2	0·2	0·2	0·2
Yb	1·8	2·4	1·8	2·0	1·8	1·6	1·4	1·9	2·0	1·9	1·5	1·4	1·3	1·2	1·3
Lu	0·3	0·4	0·3	0·3	0·2	0·2	0·2	0·3	0·3	0·3	0·2	0·2	0·2	0·2	0·2
Hf	14·2	2·4	9·6	11·5	9·6	9·4	8·1	12·3	8·6	9·4	11·1	10·6	10·9	12·3	12·5
Ta	2·5	1·3	2·1	2·4	2·0	1·9	1·8	3·2	2·3	1·5	1·8	1·8	1·7	1·8	1·7
Pb	30·0	22·8	34·4	40·4	34·0	31·5	38·4	34·4	n.d.	n.d.	35·0	31·6	40·5	36·0	42·2
Th	30·5	18·0	27·0	31·9	29·4	27·5	46·3	37·7	9·0	18·0	38·5	37·3	48·7	49·0	49·2
U	5·6	4·4	4·3	4·8	4·2	4·4	9·7	7·5	n.d.	n.d.	6·3	5·1	6·1	6·3	7·5

Sample:	Bb135	Bg142	Bq140	Bq141	K9024	K9026	K9027	K9028	K9029	K9031	K9032	K9038	K9039	K9041
TAS classification:	TrA	Tr	Tr	Tr	TrA	TrA	TrA	BtrA	TrA	TrA	TrA	BTrA	TrA	dacite
Group:	N.-W.	N.-C.	K	N.-C.	N.-C.	N.-C.	N.-C.	N.-C.	N.-C.	N.-C.	N.-C.	N.-C.	N.-C.	N.-C.
Locality:	Qiang	Yong	Yong	Yong	Kunlun	Kunlun	Kunlun	Kunlun	Kunlun	Kunlun	Kunlun	Kunlun	Kunlun I	Kunlun
SiO_2	63·6	68·9	69·2	69·0	57·7	58·0	57·9	56·9	57·4	57·3	58·3	57·2	58·1	66·1
TiO_2	1·5	0·8	0·8	0·8	1·6	1·7	1·7	1·6	1·7	1·6	1·6	1·6	1·8	0·8
Al_2O_3	15·0	15·8	14·5	14·7	15·7	16·0	16·1	15·6	15·9	15·6	15·9	16·2	16·7	15·1
Fe_2O_3*	5·4	2·2	3·2	3·7	7·2	6·8	6·9	6·6	6·8	7·0	7·3	6·1	7·7	6·2
MnO	0·0	0·0	0·0	0·0	0·1	0·1	0·1	0·1	0·1	0·1	0·1	0·2	0·0	0·1
MgO	1·7	0·7	1·2	0·7	3·3	2·8	2·9	2·9	2·8	3·4	2·9	2·6	1·3	0·9
CaO	3·4	1·9	1·4	1·9	5·8	5·5	5·4	8·0	6·4	6·5	5·1	7·6	5·9	3·1
Na_2O	4·0	4·0	4·2	4·3	3·8	4·0	4·0	3·8	4·0	3·7	3·9	3·8	3·9	4·3
K_2O	4·3	5·4	5·1	4·4	3·9	4·2	4·1	3·8	4·1	3·9	4·1	3·8	3·8	3·0
P_2O_5	1·2	0·2	0·3	0·4	0·9	0·8	0·9	0·8	0·8	0·8	0·8	0·9	0·9	0·3
Mg no.†	43	46	48	31	53	50	51	52	51	55	50	52	29	26

Sample:	Bb135	Bg142	Bq140	Bq141	K9024	K9026	K9027	K9028	K9029	K9031	K9032	K9038	K9039	K9041
TAS classification:	TrA	Tr	Tr	Tr	TrA	TrA	TrA	BtrA	TrA	TrA	TrA	BTrA	TrA	dacite
Group:	N.-W.	N.-C.	K	N.-C.	N.-C.	N.-C.	N.-C.	N.-C.	N.-C.	N.-C.	N.-C.	N.-C.	N.-C.	N.-C.
Locality:	Qiang	Yong	Yong	Yong	Kunlun	Kunlun	Kunlun	Kunlun	Kunlun	Kunlun	Kunlun	Kunlun	Kunlun I	Kunlun
LOI	1·1	1·4	1·2	1·1	1·8	0·9	0·8	3·8	1·9	2·0	0·9	3·3	2·3	0·4
Sc	6·1	0·7	0·9	1·3	9·6	8·9	8·2	8·2	8·7	11·7	11·2	11·4	12·2	13·9
V	67·2	21·5	21·8	24·0	97·5	95·3	95·9	90·0	90·4	104·4	104·0	115·4	117·0	24·6
Cr	23·7	5·2	3·4	3·6	86·0	35·0	47·0	43·0	35·0	62·0	83·0	109·0	107·0	28·0
Co	7·2	3·2	3·0	2·1	17·7	15·0	14·5	14·4	15·8	17·7	16·9	19·3	19·5	6·6
Ni	8·1	2·2	4·1	1·2	34·7	21·5	21·8	21·1	23·0	36·5	36·3	40·9	56·3	2·1
Cu	n.d.	n.d.	n.d.	n.d.	4·4	19·9	17·3	18·7	21·1	24·3	23·2	n.d.	n.d.	n.d.
Zn	n.d.	n.d.	n.d.	n.d.	97·5	98·2	94·0	94·1	102·7	101·2	98·6	n.d.	n.d.	n.d.
Ga	22·7	23·1	22·3	23·6	18·9	20·3	19·4	18·9	21·0	20·1	20·8	19·2	20·5	21·0
Rb	182·6	236·7	235·0	239·4	109·8	116·4	111·3	106·7	126·2	118·4	118·6	93·6	92·6	185·8
Sr	861·0	651·5	633·8	720·2	981·9	898·7	969·0	967·9	1077·9	1001·4	1057·3	1073·7	1003·3	234·3
Y	20·4	7·4	7·9	10·2	24·1	24·0	23·4	23·0	24·6	24·8	25·6	23·4	25·7	40·2
Zr	535·9	239·8	268·9	639·0	412·2	432·4	426·1	400·7	461·6	440·5	443·8	323·7	341·1	282·0
Nb	37·6	11·3	10·7	13·7	40·9	44·9	42·6	40·6	46·6	43·7	43·9	39·2	43·0	17·0
Ba	1970	1789	1768	1763	1605·9	1672·9	1609·6	1609·7	1701·0	1731·8	1815·9	1426·7	1576·6	594·5
La	191·2	138·1	137·9	151·4	113·6	122·7	118·4	108·7	119·7	120·7	123·4	81·9	89·1	37·8
Ce	353·3	238·9	242·6	262·7	214·3	231·3	224·5	204·8	225·1	229·1	235·2	163·7	177·8	79·6
Pr	37·0	24·4	24·3	26·5	23·5	25·9	24·6	22·8	24·9	25·3	26·1	19·0	20·9	9·7
Nd	123·3	79·1	79·6	85·5	84·4	90·4	87·6	81·0	88·3	90·7	89·9	70·5	76·3	38·9
Sm	15·7	10·1	10·1	11·0	11·8	12·8	12·2	11·3	12·4	12·8	13·2	10·4	11·4	7·8
Eu	3·0	2·0	1·8	2·1	2·6	2·8	2·7	2·5	2·8	2·8	2·8	2·4	2·7	2·0
Gd	10·4	6·1	6·2	6·9	8·7	9·2	8·7	8·3	9·1	9·1	8·7	7·7	8·7	7·3
Tb	1·1	0·6	0·6	0·7	1·0	1·0	1·0	1·0	1·0	1·0	1·0	0·9	1·0	1·1
Dy	4·4	1·8	1·9	2·4	4·7	4·9	4·8	4·5	4·8	4·9	5·0	4·6	5·0	6·6
Ho	0·7	0·2	0·3	0·3	0·8	0·8	0·8	0·8	0·8	0·8	0·8	0·8	0·9	1·3
Er	1·6	0·5	0·5	0·7	2·1	2·0	2·0	1·9	2·1	2·1	2·1	2·0	2·2	3·7
Tm	0·2	0·1	0·1	0·1	0·3	0·3	0·3	0·3	0·3	0·3	0·3	0·3	0·3	0·6
Yb	1·3	0·3	0·4	0·5	1·7	1·7	1·7	1·6	1·7	1·8	1·8	1·7	1·9	3·5
Lu	0·2	0·0	0·0	0·1	0·2	0·3	0·2	0·2	0·3	0·3	0·3	0·3	0·3	0·5
Hf	11·8	6·1	6·7	11·8	8·6	9·3	9·0	8·4	9·5	9·4	9·3	7·1	7·5	6·8
Ta	1·8	0·5	0·5	0·6	2·0	2·3	2·1	2·1	2·3	2·2	2·2	2·1	2·3	1·8
Pb	42·4	71·1	76·0	97·8	31·1	25·9	32·2	25·0	28·6	31·9	25·9	21·3	22·4	20·9
Th	52·6	61·6	60·7	68·2	19·6	21·3	20·5	19·4	21·7	21·1	20·9	11·6	12·7	13·2
U	7·8	5·9	9·3	11·1	3·5	3·4	3·3	3·4	3·6	3·4	3·5	2·3	2·3	5·8

Table 2b: continued

Sample:	K9001	K9002	K9006	K9007	K9008	K9016	K9017	K9018	K9019	K9021
TAS classification:	rhyolite	dacite	TrA	TrA	TrA	TrA	TrA	TrA	TrA	TrA
Group:	C.-P.	C.-P.	C.-P.	C.-P.	C.-P.	C.-P.	C.-P.	C.-P.	C.-P.	C.-P.
Locality:	Dogai C.	Dogai C.	Dogai C.	Dogai C.	Dogai C.	Dogai C.	Dogai C.	Dogai C.	Dogai C.	Dogai C.
SiO_2	74·7	72·2	62·4	61·1	62·4	62·9	62·6	62·0	61·3	62·5
TiO_2	0·6	0·6	1·6	1·6	1·6	1·5	1·6	1·6	1·7	1·6
Al_2O_3	12·8	13·9	15·3	15·7	15·4	15·1	15·3	15·2	15·2	15·3
Fe_2O_3*	3·6	4·3	6·0	6·3	6·3	5·7	6·0	6·2	6·3	6·0
MnO	0·1	0·1	0·1	0·1	0·1	0·1	0·1	0·1	0·1	0·1
MgO	1·4	1·5	1·8	1·9	1·3	1·6	1·7	1·8	1·9	1·8
CaO	1·5	1·8	4·0	4·9	3·8	4·2	4·1	4·4	4·7	4·0
Na_2O	3·5	3·1	3·9	3·5	3·9	3·9	3·8	3·8	3·8	3·8
K_2O	1·9	2·3	4·1	4·0	4·3	4·2	4·2	4·2	4·1	4·2
P_2O_5	0·1	0·1	0·9	0·8	0·9	0·8	0·9	0·9	0·9	0·8
Mg no.†	49	46	42	43	33	41	41	42	42	43
LOI	1·4	1·8	1·1	3·0	0·9	0·8	0·9	1·0	1·9	0·8
Sc	6·9	8·3	7·3	7·2	7·0	6·1	6·6	7·2	6·9	6·4
V	59·1	68·2	84·6	72·4	80·9	67·7	78·5	80·2	85·8	75·1
Cr	77·0	76·0	18·0	15·0	21·0	40·0	18·0	16·0	21·0	15·0
Co	9·6	11·0	11·2	11·4	10·3	9·6	9·5	10·8	11·9	10·4
Ni	20·4	24·5	7·2	10·9	7·5	7·0	5·8	8·1	10·3	7·0
Cu	n.d.	n.d.	n.d.	n.d.	n.d.	n.d.	n.d.	n.d.	n.d.	n.d.
Zn	n.d.	n.d.	n.d.	n.d.	n.d.	n.d.	n.d.	n.d.	n.d.	n.d.
Ga	13·4	15·1	24·7	23·3	23·2	23·3	23·2	23·1	22·9	22·1
Rb	69·6	99·6	226·6	199·2	207·7	237·8	213·5	209·2	192·8	204·0
Sr	222·5	198·0	755·3	699·2	649·7	623·5	717·9	665·5	774·1	669·2
Y	21·9	23·8	27·8	26·7	24·6	23·5	26·2	26·6	26·3	24·8
Zr	109·2	137·7	523·1	491·8	480·6	407·0	486·0	492·4	484·6	486·1
Nb	10·3	11·6	48·6	44·5	45·1	42·7	45·0	45·8	45·7	43·0
Ba	356·7	375·8	1640·3	1457·6	1507·1	1344·5	1460·6	1521·1	1542·3	1416·2
La	29·1	29·6	148·9	138·6	138·7	131·4	139·6	145·0	140·1	136·8
Ce	57·4	59·1	281·3	263·1	253·9	251·4	263·6	262·1	265·6	257·6

Sample:	K9001	K9002	K9006	K9007	K9008	K9016	K9017	K9018	K9019	K9021
TAS classification:	rhyolite	dacite	TrA	TrA	TrA	TrA	TrA	TrA	TrA	TrA
Group:	C.-P.	C.-P.	C.-P.	C.-P.	C.-P.	C.-P.	C.-P.	C.-P.	C.-P.	C.-P.
Locality:	Dogai C.	Dogai C.	Dogai C.	Dogai C.	Dogai C.	Dogai C.	Dogai C.	Dogai C.	Dogai C.	Dogai C.
Pr	6·9	7·1	30·6	28·9	29·8	27·6	28·9	30·6	28·9	28·1
Nd	26·1	27·4	108·5	101·9	102·8	97·4	100·9	105·6	102·1	99·5
Sm	4·8	5·2	15·3	14·7	14·7	13·8	14·5	15·1	14·8	14·0
Eu	1·0	1·1	3·0	2·8	2·9	2·6	2·8	2·9	2·9	2·8
Gd	4·2	4·4	10·8	10·2	10·5	9·6	10·1	10·8	10·5	9·8
Tb	0·6	0·7	1·2	1·2	1·2	1·1	1·2	1·2	1·2	1·1
Dy	3·7	3·9	5·6	5·4	5·3	4·9	5·3	5·5	5·3	5·1
Ho	0·7	0·8	0·9	0·9	0·8	0·8	0·9	0·9	0·9	0·8
Er	2·1	2·2	2·2	2·2	2·1	1·9	2·2	2·2	2·1	2·1
Tm	0·3	0·3	0·3	0·3	0·3	0·3	0·3	0·3	0·3	0·3
Yb	2·2	2·2	1·8	1·8	1·6	1·5	1·7	1·8	1·7	1·6
Lu	0·3	0·3	0·3	0·3	0·2	0·2	0·2	0·3	0·2	0·2
Hf	3·2	3·8	11·0	10·4	10·2	9·1	10·1	10·4	10·1	10·4
Ta	0·8	0·8	2·7	2·4	2·6	2·6	2·6	2·6	2·4	2·4
Pb	8·9	12·7	41·7	69·9	29·4	28·9	44·9	37·1	38·2	39·5
Th	9·6	9·8	32·1	30·5	30·1	29·3	30·4	30·9	28·6	30·1
U	2·1	2·2	8·2	6·6	7·4	8·4	7·7	7·5	6·9	7·5

S.-W., south-west group; S.-E., south-east group; S.-C., south–central group; P.Z., Pabbai Zong group and locality; N.-W., north-west; N.-C., north–central group; C.-P., central plateau group. TrA, trachyandesite; Tr, trachyte; BTrA, basaltic trachyandesite; PhT, phonotephrite; Ash, Ashikule; Hei, Heishibei; Quiang, Quangshuigou; Tien, Tienchuhai; Yong, Yongbocuo; Dogai c., Dogai Coring. n.d., not determined. LOI, loss on ignition. It should be noted that LOI values are strongly affected by the presence of hydrous mineral phases such as micas in some samples and are thus not necessarily indicative of the level of sample alteration. The major and trace element data for samples T2A, T3B, T4A and T5A are from Williams *et al*. (2001).

*Total iron.

†Mg number calculated on the basis of 2+ cations assuming that 80% of total iron is present as FeO.

Table 3: Sr and Nd isotope data

Sample	Age (Ma)	$^{87}Rb/^{86}Sr$*	$^{147}Sm/^{144}Nd$*	$^{87}Sr/^{86}Sr$	±2 SD†	$^{143}Nd/^{144}Nd$	±2SD†	$^{87}Sr/^{86}Sr_{(i)}$‡	$^{143}Nd/^{144}Nd_{(i)}$‡	$\varepsilon Nd_{(i)}$	T_{DM}Nd (Ga)
Southern Tibet											
JPT24A§	23·2	2·80	0·11	0·715271	32[a]	0·511955	4[e]	0·714352	0·511938	−13·1	1·52
JPT24B	22·3	1·82	0·13	0·715276	8[b]	0·511914	4[e]	0·714698	0·511895	−13·9	1·94
JPT24C	24·0	1·75	0·13	0·715049	25[c]	0·511767	4[e]	0·714452	0·511747	−16·8	2·16
20E39A§	18·0	0·29	0·11	n.d.		0·512419	4[e]	n.d.	0·512406	−4·1	0·90
JPT22§	23·0	4·26	0·09	0·735148	8[b]	0·512121	4[e]	0·733744	0·512107	−9·8	1·16
JPT14.1	18·8	0·28	0·10	0·707216	8[b]	0·512021	4[e]	0·707142	0·512009	−11·8	1·32
JPT3	13·9	0·42	0·10	0·706694	25[c]	0·512357	4[e]	0·706612	0·512348	−5·3	0·95
JPT4§	13·4	0·65	0·09	0·706764	25[b]	0·512431	4[e]	0·706640	0·512423	−3·9	0·79
JPT5.2	12·5	1·26	0·09	0·706945	8[b]	0·512307	4[e]	0·706720	0·512300	−6·3	0·95
JPT8	13·8	5·75	0·08	0·711373	25[c]	0·512028	4[e]	0·710246	0·512021	−11·7	1·19
Northern Tibet											
912	1·2	0·49	0·09	0·708373	12[d]	0·512152	7[f]	0·708365	0·512152	−9·5	1·10
1105	5·0	1·21	0·11	0·710180	12[d]	0·512013	7[f]	0·710094	0·512009	−12·1	1·55
K702§	0·5	0·27	0·09	0·710180	32[a]	0·511985	7[f]	0·710178	0·511985	−12·7	1·27
K703§	0·5	0·31	0·09	n.d.		0·512110	7[f]	n.d.	0·512110	−10·3	1·13
K9026	12·4	0·37	0·09	0·708164	12[d]	0·512334		0·708098	0·512337	−5·8	0·86
K9029§	13·0	0·34	0·08	0·708242	8[b]	0·512362	4[e]	0·708179	0·512355	−5·2	0·82
K9032	11·9	0·32	0·09	0·708233	12[d]	0·512338		0·708178	0·512331	−5·7	0·87
K9039	12·5	0·27	0·09	0·707939	8[b]	0·512371	4[e]	0·707892	0·512364	−5·0	0·84
K9002§	8·7	1·45	0·11	0·714156	12[d]	0·511949	4[e]	0·713976	0·511943	−13·3	1·63
K9017§	9·0	0·86	0·09	0·708976	32[a]	0·512296	7[f]	0·708867	0·512291	−6·5	0·91
K9019§	9·0	0·72	0·09	0·709057	32[a]	0·512282	4[e]	0·708965	0·512277	−6·8	0·93
Bg142§	9·4	1·05	0·08	0·709992	12[d]	0·512110	7[f]	0·709852	0·512106	−10·1	1·04
Bq141§	9·4	0·96	0·08	0·709821	32[a]	0·512126	4[e]	0·709693	0·512121	−9·8	1·03

*$^{87}Rb/^{86}Sr = 2{\cdot}981 \times [Rb/Sr]$, $^{147}Sm/^{144}Nd = 0{\cdot}062 \times [Sm/Nd]$; concentrations of Rb, Sr, Sm and Nd are given in Table 2.
†The 2 SD error from repeat analyses of the Sr standard NBS 987 or the Johnson and Matthey Nd standard during the period of analysis are applied to the sample data, values of the NBS 987.
‡Initial isotope ratios calculated using $^{40}Ar-^{39}Ar$ eruption ages.
§Where no Ar existed for the sample the average age of the volcanic province (from Ar data on other samples) was used.
Sr standard and Johnson and Matthey Nd standard and the relevant reproducibilities are given in the main text. The period of analysis and mass spectrometer is indicated by the superscript letter (Sr, a–d; Nd, d and e): a, Nu plasma June 1999; b, TIMS MAT 261 December 1998; c, TIMS MAT 261 June 1998; d, TIMS University of Cambridge, e, TIMS MAT 262 1999; f, Nu Plasma November 1999. Sr isotope ratios were normalized to NBS 987 = 0·71023; Nd isotopes were normalized to Johnson and Matthey Nd = 0·51185, as discussed in the main text.

analyses. This approach is analogous to the common practice of normalizing TIMS data to the global value for the NBS 987 standard, using a normalization factor derived from the ratio of the measured NBS 987 to the accepted value of 0·710230. This takes exponential fractionation laws into account, whereas a linear fractionation law is normally assumed for TIMS. Finally, a correction for the interference of ^{87}Rb on ^{87}Sr in the sample analyses was made by measuring the interference-free ^{85}Rb isotope and using the recommended value of $^{85}Rb/^{87}Rb$ (0·386). The long-term average and reproducibility for the NBS 987 Sr standard measured on the Nu Instruments machine during this period was 0·710229 ± 32 (2 SD).

For Sr analysis on the Finnigan MAT 261 mass spectrometer, each sample was loaded onto a Ta single filament using high-purity Teflon-distilled H_2O and 10% phosphoric acid (H_3PO_4). Analyses involved collection of 100–120 ratios with a ^{87}Sr beam of ≥1 pA. The typical internal precision for each run was ± 10–20 2σ in the sixth decimal place. Each sample was corrected for mass fractionation during the run to $^{86}Sr/^{88}Sr = 0{\cdot}1194$. There were two main periods of TIMS Sr isotope analysis on the Finnigan MAT 261 at the OU, from June to July in 1998 and from November to December in 1998. The values and reproducibilities of the NBS 987 Sr standard during these periods were 0·710286 ± 25 (2 SD) and 0·710172 ± 11 (2 SD),

respectively. The value and reproducibility of the NBS 987 Sr standard on the VG sector 54 mass spectrometer at the University of Cambridge was 0·710258 ± 12 (2 SD). Details of procedures adopted for TIMS at the University of Cambridge have been given by Ahmad *et al.* (2000). All measured sample Sr isotope compositions were normalized to an NBS 987 value of 0·71023, and are thus directly comparable with our MC-ICP-MS data.

For standard and sample Nd analyses, the interference of ^{144}Sm on ^{144}Nd was first corrected for by measuring the intensity of the ^{147}Sm isotope and using the accepted value for ^{147}Sm/^{144}Sm (0·20667). The interference-corrected value for ^{144}Nd/^{146}Nd was then corrected to the generally accepted value for ^{144}Nd/^{146}Nd (0·7219), by assuming that that any deviation is a function of exponential mass fractionation. The derived fractionation factor was then used to perform a second fractionation correction on ^{144}Nd, this time taking fractionation effects on ^{147}Sm/^{144}Sm into account. The value of ^{144}Nd/^{146}Nd obtained from this calculation was then compared with the accepted ^{144}Nd/^{146}Nd values, and used to calculate a final fractionation factor. This was then applied to the measured ^{143}Nd/^{144}Nd. Nd isotope ratios analysed by TIMS were fractionation corrected to ^{144}Nd/^{146}Nd = 0·7219; isotope ratios were normalized to the value for the Johnson and Matthey Nd standard obtained on the Nu Plasma machine so that the data obtained on the two machines could be compared. The value and associated reproducibility of the Johnson and Matthey Nd standard obtained on the Nu Instruments machine was 0·511788 ± 7 (2 SD).

For TIMS, Nd ionization was promoted using a second Re filament; analyses required collection of 150–200 ratios with ^{143}Nd and ^{144}Nd beams ≥2 pA. Samples were corrected for mass fractionation during the run using the accepted terrestrial of ^{144}Nd/^{146}Nd. Internal precision for each run was ±5 to ±10 2σ in the sixth decimal place. The value and reproducibility of the Johnson and Matthey Nd standard during this period of analysis was 0·511758 ± 4 (2 SD). Samples were normalized to accepted value for the Johnson and Matthey Nd standard of 0·511850.

Separation of Pb was achieved using a small-scale anionic exchange technique similar to that of Mahnes *et al.* (1978). Procedural blanks were <0·3 ng. Pb isotopes were analysed by MC-ICP-MS at the OU, and were corrected for mass bias by internal normalization to ^{205}Tl/^{203}Tl (2 ppm Pb sample solutions were doped to contain 2 ppm Tl). Solutions were introduced into the plasma torch via a Cetac Aridus desolvating nebulizer. HNO_3 was found to have an affinity for Hg, resulting in significant interference of ^{204}Hg with ^{204}Pb, so the samples were prepared in 2% HCl, which was also used for cleaning between samples. All analyses were made in static multi-collector mode: peak integration times were 8 s; baselines were measured for 16 s at half mass. An analysis consisted of 10 blocks of ratios, and 10 measurements were made per block. The ratio ^{202}Hg/^{204}Hg was monitored and used to correct for interference of ^{204}Hg with ^{204}Pb. The samples were analysed in two short periods in April 1999 and June 2000. The reproducibilities and associated errors for the NBS 981 standard during the analytical sessions were: April 1999, ^{206}Pb/^{204}Pb 16·9403 ± 12, ^{207}Pb/^{204}Pb 15·497 ± 4, ^{208}Pb/^{204}Pb 36·721 ± 9; June 2000, ^{206}Pb/^{204}Pb 16·9391 ± 2, ^{207}Pb/^{204}Pb 15·497 ± 1, ^{208}Pb/^{204}Pb 36·725 ± 2. Although these errors appear low, it should be borne in mind that they are derived from two short analytical sessions with durations of a few days only, and do not constitute rigorous estimates of long-term reproducibility. Lead analyses were not undertaken between these two analytical sessions because of technical problems in 1999–2000.

RESULTS

Major and trace element geochemistry

The majority of post-collisional Tibetan volcanic rocks and associated intrusives plot above the alkali–tholeiite divide on the total alkalis–silica (TAS) plots (Le Maitre *et al.*, 1989) in Fig. 2. Northern samples plot in the basaltic trachyandesite, trachyandesite and trachyte fields and a minority plot in the phono-tephrite (the more mafic Tienchuhai and Heishebei samples in the NW group) and rhyolite fields (Dogai Coring, north–central group). The southern groups are composed predominantly of trachyandesites and trachytes, with minor dacites and rhyolites. Of the southern groups, the south-west group generally shows the highest total alkali contents (average 8·9 wt %), compared with the south–central (average 7·0 wt %) and south-east (average 6·4 wt %) groups. The latter group borders the alkali–silica divide, the most primitive sample just falling into the basaltic andesite group, and shows a slight positive tend of total alkalis against silica. The Pabbai Zong dykes show a negative correlation between total alkalis and silica contents, and have total alkali contents ranging from 9·1 wt % to 6·7 wt %.

There is a broad correlation between the TAS classification and petrography in the southern Tibetan samples: samples that lie close to or below the alkali–tholeiite divide (primarily the south–central and south-east samples) have either biotite or hornblende as a major phenocryst phase. In contrast, the majority of samples from the south-west and Pabbai Zong groups lie above the divide and have phlogopite and clinopyroxene (±orthopyroxene) as phenocryst phases.

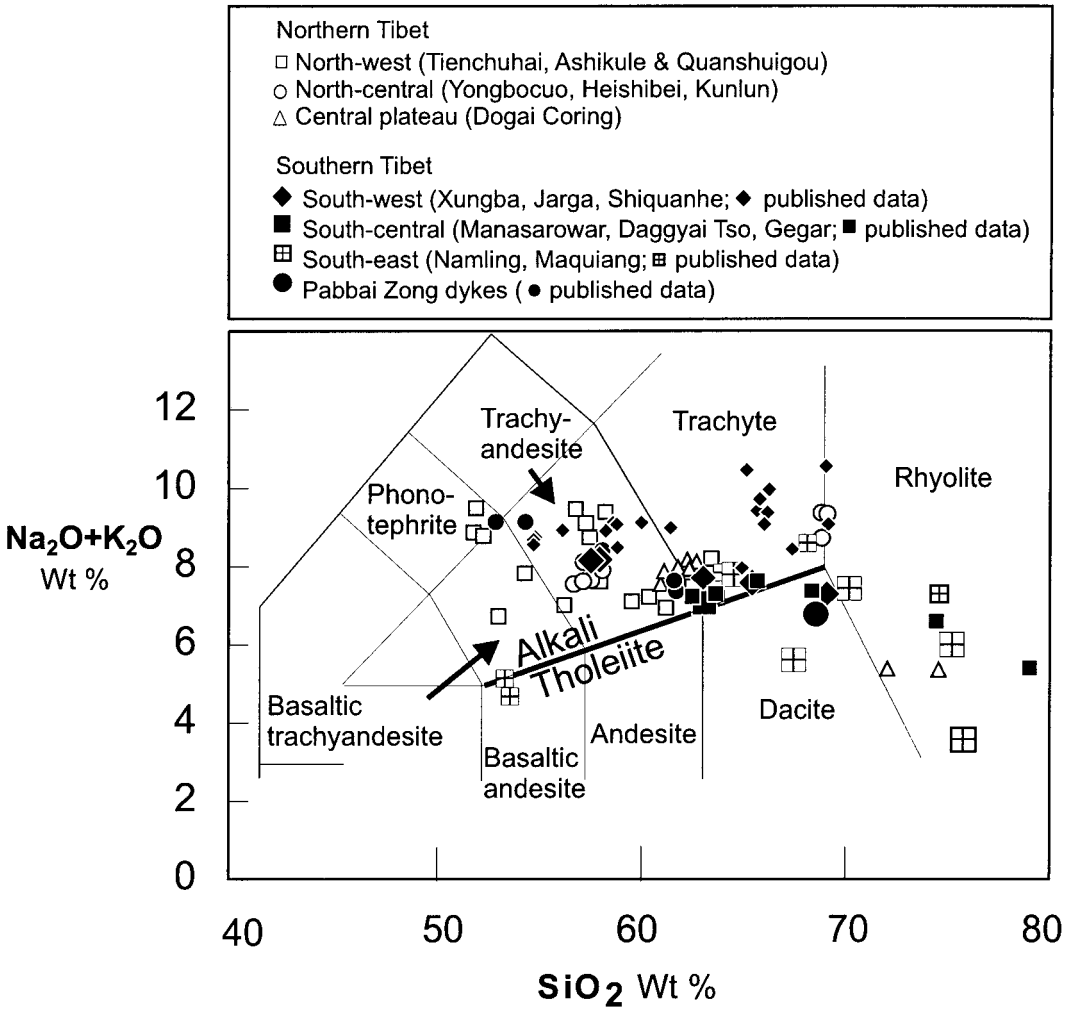

Fig. 2. Total alkalis vs silica plot for the northern and southern Tibetan volcanic sub-groups. All the major element data have been recalculated to 100% on a H_2O- and CO_2-free basis (Le Bas & Le Maitre, 1986). The samples have been grouped by their broad geographical regions rather than by their individual locality names because, in many cases, there were insufficient samples from an individual locality to form a coherent group representing cogenetic magma series. The 'north-west' group comprises samples from the Tienchuhai, Quanshuigou and Ashikule regions in northern Tibet. The 'north–central' group includes samples from Yongbocuo and Heishibei areas and from the north Kunlun [comparable with 'zone VII' defined by Turner *et al.* (1996)], whereas samples from Dogai Coring [originally referred to as 'zones VIII and IX' by Turner (1996)] make up the 'central-plateau' group. The major element data for all the northern samples are taken from Turner *et al.* (1996) (and references therein). For southern Tibet, the 'south-west' group contains samples from the Xungba, Jarga and Shiquanhe areas, the 'south–central' group is composed of samples from the Lake Manasarowar, Gegar and Daggyai Tso graben localities, and the 'south-east' group contains samples from the Namling basin and Maquiang localities. The Pabbai Zong dykes are plotted as a separate group. Data sources: the data for the Xungba, Jarga, Manasarowar and Gegar samples are taken from Miller *et al.* (1999); both new and published data (Turner *et al.*, 1996) are shown for Shiquanhe samples; new and published data (Williams *et al.*, 2001) are shown for the Pabbai Zong dykes and the Daggyai Tso samples; data for the Namling samples are new; data for the Maquiang samples are taken from Coulon *et al.* (1986).

Direct relationships between sample petrography and TAS classification are more difficult to evaluate for the northern Tibet samples as there is less information available in the literature on their petrography, and some of the samples that were reanalysed were available only in powder form.

In the Harker diagram of K_2O vs SiO_2 (Fig. 3), the majority of the northern and southern sub-groups lie within the shoshonitic field. The northern sample groups cluster tightly above the shoshonite–high K calc-alkaline divide, with the exception of a few more silicic samples from the Dogai Coring (central-plateau group) and Kunlun (NW group) localities. Within the southern Tibet groups, samples from the south-west and Pabbai Zong groups lie above or on the shoshonite–high K calc-alkaline divide at SiO_2 contents of 52–69

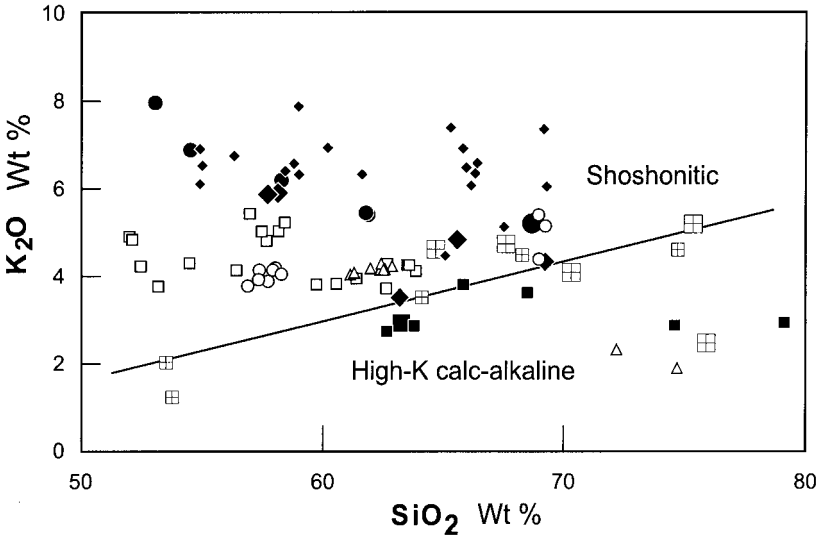

Fig. 3. K_2O vs SiO_2 plot for the northern and southern Tibetan volcanic sub-groups. Sample groups, symbols and data sources as in Fig. 2. The shoshonite–calc-alkaline divide is taken from Gill (1981).

wt %, whereas samples from the south–central and south-east groups plot in the high-K calc-alkaline field. There are no clear correlations between K_2O and SiO_2 in the south-west and south–central groups. The south-east samples have the lowest K_2O contents (average 3·6 wt %) and plot around the shoshonitic–calc-alkaline divide, spanning a wide range of silica contents (52–74 wt %) and showing a positive trend of K_2O with respect to SiO_2. The Pabbai Zong samples show a slight negative correlation between K_2O and SiO_2. In general, the less evolved ($SiO_2 < 60\%$) southern and northern samples have low K_2O/Al_2O_3 ratios (north 0·23–0·39; south 0·41–0·58; data sources as in Fig. 3), suggesting that they have the greatest affinity with the Group 1 potassic lavas (lamproites) as defined by Foley (1992*a*).

In Fig. 4, it can be seen that Fe_2O_3* (Fig. 4a), CaO (Fig. 4b) and TiO_2 (Fig. 4c) correlate positively with MgO for both the northern and southern groups, although the southern samples have lower contents of Fe_2O_3* and TiO_2 for the same MgO contents. The southern samples show a much wider range in MgO compositions relative to the northern samples. Samples from the south-west and Pabbai Zong groups have the highest MgO contents and the highest Cr contents, and exhibit positive correlations between MgO and Cr (Fig. 4d). The MgO and Cr contents of the south-east, south–central and northern sample groups are similar. Sr shows a steep positive correlation with MgO in most sub-groups (Fig. 4e). The exceptions are the south-west and Pabbai Zong groups, which show a positive correlation but with a much shallower slope, and the south–central group, where there is no significant correlation. Both the south-west and the Pabbai Zong groups define positive trends of Rb against MgO (Fig. 4f). The south-east, south–central and all northern groups show no such correlations. Samples from all the northern groups have much higher Ce contents for a given MgO content than all the southern groups but show no clear trends between MgO and Ce contents (Fig. 4g) whereas the south-west and Pabbai Zong groups both show positive correlations between MgO and Ce. The south-east and south–central groups have lower concentrations of Ce relative to the south-west and Pabbai Zong groups, and also exhibit slight negative trends of Ce against MgO. The behaviour of Sm (and the other REE) relative to MgO (Fig. 4h) is similar to that of Ce for all the southern groups. There are slight positive correlations between Sm and MgO in the north-west and north–central groups.

In Fig. 5, primitive mantle normalized multi-element diagrams illustrate the incompatible-element enriched nature of the most mafic southern and northern samples. All samples display negative Nb, Ta and Ti anomalies, which are most pronounced in the south-west and Pabbai Zong samples. Positive Pb anomalies are seen in the north–central and central-plateau groups and all southern sub-groups. The northern groups, the south-west and Pabbai Zong groups have negative Sr anomalies. In the northern groups, K also exhibits a negative anomaly with respect to U and La. Figure 5b demonstrates that there is a significant difference between the south-west and Pabbai Zong samples and the south–central and south-east groups: the latter have much lower concentrations of

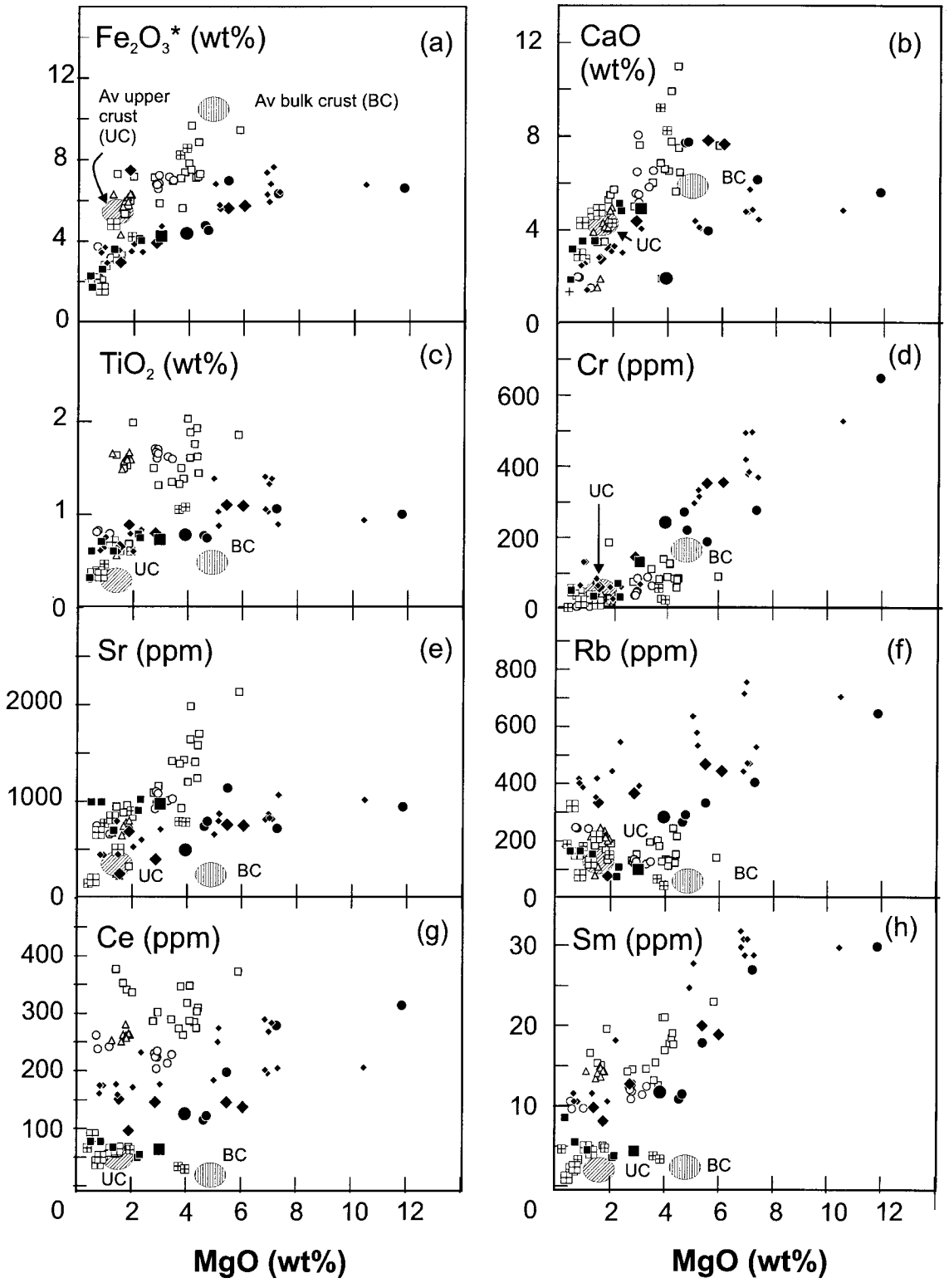

Fig. 4. Abundances of major (wt %) and trace elements (ppm) plotted against wt % MgO. Average major and trace element compositions for the bulk (BC) and upper crust (UC) (Taylor & McLennan, 1995) are shown as fields, which have been enlarged for clarity. Sample groups, symbols and the sources of the major element data are as in Fig. 2. New trace element data for northern and southern Tibet samples are given in Table 2. The trace element data for samples from the Xungba area and the CAV are from Miller *et al.* (1999), and data for three samples from the Shiquanhe area are from Arnaud (1992).

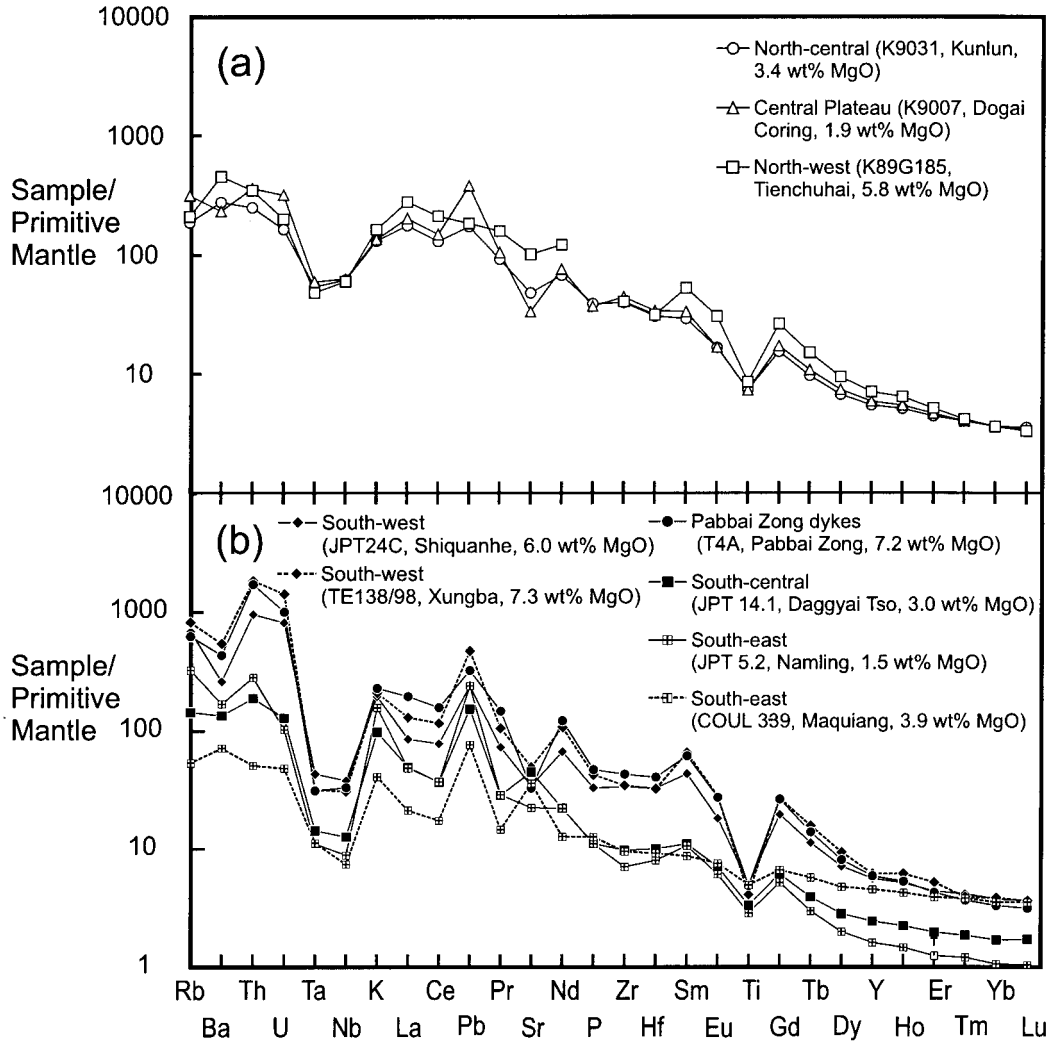

Fig. 5. Primitive mantle (Sun & McDonough, 1989) normalized multi-element plot for representative samples from the northern (a) and southern (b) volcanic sub-groups. The most primitive samples from each sub-group are plotted, and the sample names and MgO contents are shown in the legend. In the case of NW Tibet, the sample plotted does not have P_2O_5 data but was selected as this was the most primitive sample for which the most data were available. The Pabbai Zong sample plotted (T4A) is considered to be more representative of the sample group than the most primitive sample (T2A) that has extreme Sr, Nd and Pb isotopic compositions relative to other samples from Pabbai Zong. The trace element data for all the samples except TE138/98 (Miller *et al.*, 1999) and COUL 339 (Turner *et al.*, 1996) are new and are presented in Table 2.

incompatible and light REE (LREE) to middle REE (MREE) and also show much shallower slopes from Gd to Lu.

Sr–Nd–Pb isotope geochemistry

All samples have radiogenic $^{87}Sr/^{86}Sr_{(i)}$ and unradiogenic $\varepsilon Nd_{(i)}$ (Fig. 6a, Table 3). The southern groups display considerable variation in $^{87}Sr/^{86}Sr_{(i)}$ (south-west 0·714352–0·737583; south–central 0·706848–0·709554; south-east 0·704773–0·710276; Pabbai Zong 0·711573–0·739321; all ranges quoted include published data) and $\varepsilon Nd_{(i)}$ (south-west −16·8 to −4·0; south–central −11·8 to −6·4; south-east −11·7 to +1·5; Pabbai Zong −17·7 to −12·6). The northern samples show more limited variation in $^{87}Sr/^{86}Sr_{(i)}$ (north-west 0·708034–0·710178; north–central 0·707892–0·715695; central plateau 0·708141–0·713973) compared with $\varepsilon Nd_{(i)}$ (north-west −12·7 to −5·1; north–central −10·1 to −5·0; central plateau −13·3 to −6·3). The south-west and Pabbai Zong groups have similar Sr–Nd chemistry in that they show considerable variation in Sr isotope compositions at restricted Nd isotope compositions resulting in sub-horizontal arrays on the Sr–Nd isotope plot (Fig. 6a). In contrast, the northern, south-east and

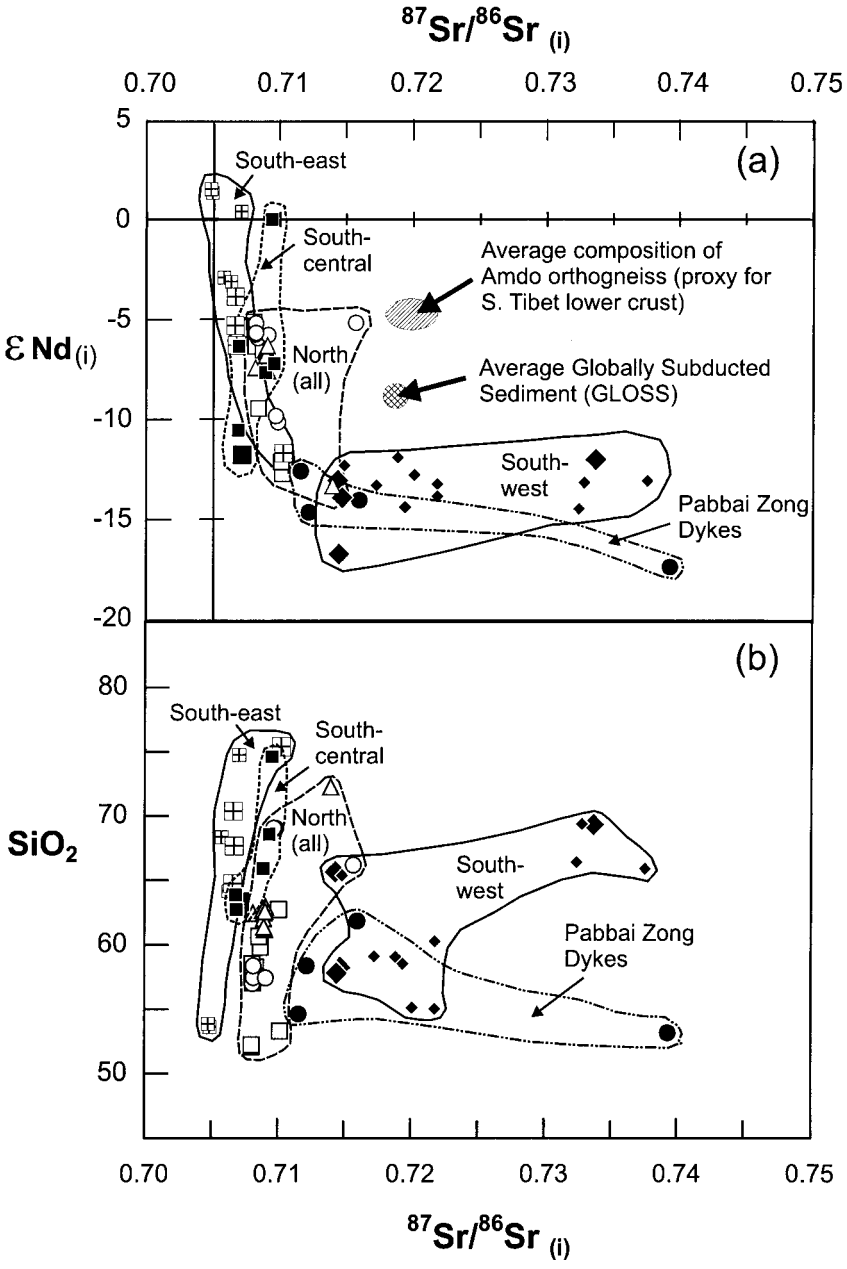

Fig. 6. (a) $\varepsilon Nd_{(i)}$ vs $^{87}Sr/^{86}Sr_{(i)}$ for northern and southern sample groups. The composition of globally averaged subducted sediment (GLOSS; Plank & Langmuir, 1998) and the Amdo orthogneiss (Harris *et al.*, 1988), a proxy for the southern Tibetan basement, are shown for reference. (b) Variation of $^{87}Sr/^{86}Sr_{(i)}$ vs SiO_2. Data sources: Turner *et al.* (1996), Miller *et al.* (1999), Williams *et al.* (2001) and Table 3. Symbols and sample groups as in Fig. 2; the error bars are smaller than symbol size.

south–central groups exhibit near-vertical arrays on the Sr–Nd plot. The Sr–Nd isotopic compositions of average Globally Subducted Sediment (GLOSS; Plank & Langmuir, 1998) and a proxy for the south Tibetan lower crust, the Amdo orthogneiss (Harris *et al.*, 1988), are shown for reference. In the plot of $^{87}Sr/^{86}Sr_{(i)}$ vs SiO_2 (Fig. 6b), it is clear that there are no strong correlations between $^{87}Sr/^{86}Sr_{(i)}$ and SiO_2 in any sample group; the south-west and Pabbai Zong groups again display similar behaviour, with near-horizontal trends of $^{87}Sr/^{86}Sr_{(i)}$ against SiO_2. The south–central, south-east and northern groups all show steep trends of $^{87}Sr/^{86}Sr_{(i)}$ against SiO_2.

Nd-depleted mantle model ages (T_{DM}; Table 3) were calculated for the northern and southern Tibetan samples assuming extraction from an upper-mantle

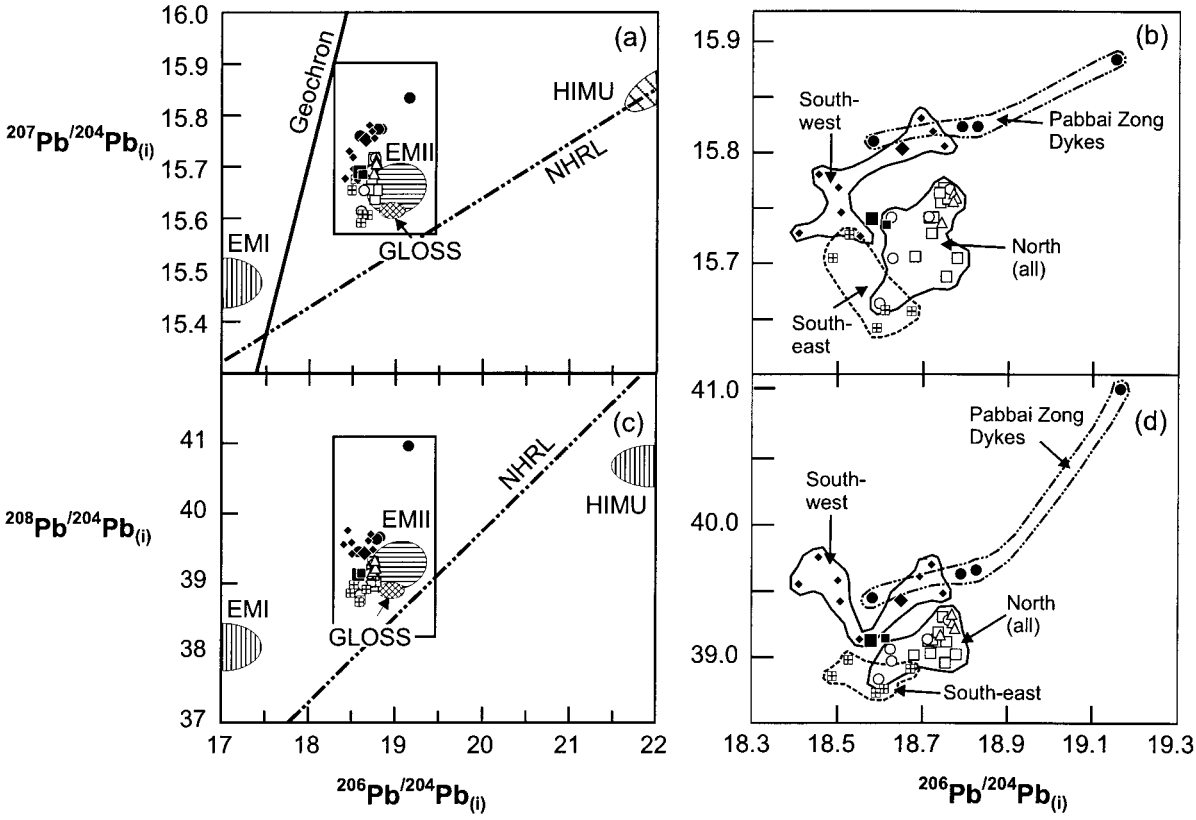

Fig. 7. $^{207}Pb/^{204}Pb_{(i)}$ (a, b) and $^{208}Pb/^{204}Pb_{(i)}$ (c, d) vs $^{206}Pb/^{204}Pb_{(i)}$. The isotopic compositions of GLOSS (Plank & Langmuir, 1998); the NHRL (Northern Hemisphere Reference Line; Hart, 1984); EMI, EMII (enriched mantle end-members); HIMU (high-μ, $^{238}U/^{204}Pb$; Zindler & Hart, 1986; Hart, 1988) are shown for reference. The symbols are as in Fig. 2 and the error ellipses are smaller than the symbol size. Data sources are Turner *et al.* (1996), Miller *et al.* (1999) and Table 4.

reservoir with present-day $^{143}Nd/^{144}Nd$ and $^{147}Sm/^{144}Nd$ of 0·513114 and 0·222, respectively (Michard, 1985). Model ages are 0·79–2·1 Ga for southern samples, and 0·82–1·6 Ga for northern samples.

On the projections of $^{207}Pb/^{204}Pb_{(i)}$ vs $^{206}Pb/^{204}Pb_{(i)}$ (Fig. 7a, enlargement 7b) and $^{208}Pb/^{204}Pb_{(i)}$ vs $^{206}Pb/^{204}Pb_{(i)}$ (Fig. 7c, enlargement 7d), the northern and southern sub-groups plot above the Northern Hemisphere Reference Line (NHRL; Hart, 1984). The northern groups show some overlap with the EMII field but do not exhibit any resolvable trends in Pb–Pb space (Fig. 7a and c). In the enlarged plots (Fig. 7b and d), the northern lavas show limited variation in their $^{207}Pb/^{204}Pb_{(i)}$ (north-west 15·68–15·72; north–central 15·61–15·72; central plateau 15·68–15·71), $^{208}Pb/^{204}Pb_{(i)}$ (north-west 38·95–39·30; north–central 38·83–39·28; central plateau 39·17–39·32) and $^{206}Pb/^{204}Pb_{(i)}$ compositions (north-west 18·68–18·77; north–central 18·59–18·76; central plateau 18·74–18·77). The southern samples show considerably more variation in their $^{207}Pb/^{204}Pb_{(i)}$ (south-west 15·67–15·78; south–central 15·68–15·69; south-east 15·59–15·68; Pabbai Zong 15·76–15·83), $^{208}Pb/^{204}Pb_{(i)}$ (south-west 39·1–39·8; south–central 39·12–39·14; south-east 38·73–38·97; Pabbai Zong 39·44–40·96), $^{206}Pb/^{204}Pb_{(i)}$ (south-west 18·41–18·74; south–central 18·58–18·61; south-east 18·49–18·67; Pabbai Zong 18·58–19·15) compositions relative to the northern samples. Interestingly, the south-east samples have $^{207}Pb/^{204}Pb_{(i)}$ and $^{208}Pb/^{204}Pb_{(i)}$ compositions that are much more unradiogenic than the other Tibetan samples, at $^{206}Pb/^{204}Pb_{(i)}$ compositions similar to the other sample groups. Neither the south-east nor the south–central sample groups define clear arrays on the Pb–Pb plots. In contrast, it appears that both the south-west and Pabbai Zong groups form positive arrays in $^{207}Pb/^{204}Pb_{(i)}$–$^{206}Pb/^{204}Pb_{(i)}$ space (Fig. 7b). Whereas the Pabbai Zong samples also define a positive trend on the $^{208}Pb/^{204}Pb_{(i)}$ vs $^{206}Pb/^{204}Pb_{(i)}$ plot, it is not clear whether the south-west group follows the same pattern. As the Pabbai Zong sample with the most radiogenic Pb isotope signatures (sample T2A; $^{207}Pb/^{204}Pb_{(i)}$ = 15·83; $^{208}Pb/^{204}Pb_{(i)}$ 40·96 $^{206}Pb/^{204}Pb_{(i)}$ 19·15) is also one of the most mafic (MgO 11·8 wt %), it is unlikely that these arrays can be explained by crustal contamination.

$^{207}Pb/^{206}Pb^*$ depleted mantle extraction model ages were calculated for individual samples by assuming radiogenic ingrowth of ^{207}Pb and ^{206}Pb after extraction of the sample's mantle source from the depleted mantle reservoir. The $^{207}Pb/^{204}Pb$ and $^{206}Pb/^{204}Pb$ ratios of the depleted mantle used in the model age calculations (15·3792 and 17·4194, respectively) were obtained from the intersection of the geochron with the NHRL (Hart, 1984), using the method of Silver *et al.* (1988). The $^{207}Pb/^{206}Pb^*$ values for the individual samples were calculated by the subtraction of the depleted mantle isotopic composition from the sample Pb isotopic compositions. The model ages were then calculated by interpolating the sample $^{207}Pb/^{206}Pb^*$ values with $^{207}Pb/^{206}Pb^*$ values calculated for different ages using the parameters of Nelson *et al.* (1985). The resulting model ages, which are 2·8–3·1 Ga for northern samples and 3·2–3·6 Ga for southern samples (Table 4), are in agreement with previous studies (Turner *et al.*, 1996; Miller *et al.*, 1999). $^{232}Th/^{204}Pb$ values of individual samples, calculated from the $^{207}Pb/^{206}Pb^*$ depleted mantle extraction model ages, are also presented in Table 4.

INTERPRETATION OF GEOCHEMICAL DATA

Evidence for residual K-bearing phases during partial melting

In Fig. 3, all three northern groups and the south-west and south–central groups form relatively flat arrays of K_2O against SiO_2. Such flat arrays suggest buffering of K_2O in these series by a K-bearing phase such as amphibole, phlogopite or K-feldspar, either during partial melting or fractionation processes. In contrast, the south-east group shows a positive array of K_2O against SiO_2, whereas the Pabbai Zong group defines a negative array on this diagram. In the case of the south-east group, the positive array is consistent with the behaviour of potassium as an incompatible element during crystal fractionation. The decrease in the K_2O contents of the Pabbai Zong samples with SiO_2 is most marked for SiO_2 contents lower than 55 wt %, and the trend becomes shallower with increasing silica contents. This trend is consistent with low-pressure fractionation of a K-bearing phase, and is in agreement with the high contents of phlogopite in the most mafic samples of this group. This observation does not in itself rule out the presence of K-bearing phases in the source region of this group; in fact, it is clear that their source region must have been highly potassic as the most magnesian samples in this group also have the highest K contents.

Examination of the behaviour of K with respect to the adjacent elements in primitive-mantle normalized multi-element diagrams (Fig. 5a and b) can reveal whether the flat arrays of K_2O vs SiO_2 formed by the northern groups and the south-west and south–central groups are the product of low-pressure fractionation, or whether they reflect residual K-bearing phases in the magma source regions. In Fig. 5a, the primitive mantle-normalized K concentrations for the north-west, north–central and central plateau groups are substantially lower than the normalized U and La concentrations (K was not compared with Nb and Ta in any of the sample groups as there are significant negative Nb and Ta anomalies in all the Tibetan samples). As this 'K anomaly' is seen in all the northern samples, irrespective of their silica contents, it implies that the 'K anomaly' is not a feature of low-pressure crystal fractionation in the crust, but is instead the product of partial melting in the presence of a residual K-bearing phase. Although the potassium contents of the northern Tibet samples are relatively high, this does not preclude the presence of residual K-bearing phases in the source region. This is because the potassium contents of the melts will also be a function of the concentration of potassium in the source region itself, the relative abundance of potassium-bearing mineral phases in the source region and the degrees of partial melting involved (potassium is enriched in small-degree partial melts).Thus, the flat arrays of K_2O vs SiO_2 seen in the northern samples may be explained by partial melting in the presence of a residual K-bearing phase, provided that the degrees of melting are small and/or the source region is enriched in potassium. The presence of residual K-amphibole or phlogopite in the source region of these rocks is consistent with high pressure ($>2·0$ GPa) experimental studies on Group 1 lamproites (Foley, 1992*a*), the group of potassic lavas to which the Tibetan samples have the most affinity (see Results section), which indicate that they are saturated with phlogopite on their liquidi.

The absence of significant Eu anomalies (indicative of residual plagioclase feldspar during melting and crystal fractionation processes) in the northern samples, in addition to the fact that the absolute concentrations of many trace elements (e.g. Sr, Rb, Ce, Sm; Fig. 4e–h) are much higher than typically observed in the continental crust (e.g. Sr, Rb, Ce, Sm; Fig. 4e–h; data source for average crustal compositions; Taylor & McLennan, 1995), implies a mantle source region. The requirement for a residual potassic phase in the magma source regions, and the high incompatible element concentrations of the samples, suggest that the source region is unlikely to have resided in the convecting asthenosphere. K-bearing clinopyroxene can be found in the deep mantle (at pressures of 5–7 GPa, for temperatures >1200°C; Tsuruta & Takahashi, 1998). However, we consider it unlikely that melting took

Table 4: Pb isotope data

	Northern Tibet					
Sample:	K702	K703	K9024	K9028	K9029	K9039
Age (Ma)	0·5	0·5	13·0	18·5	13·0	12·5
Period of analysis	a	a	a	a	a	a
U ppm	4·3	4·8	3·5	3·4	3·6	2·3
Pb ppm	34·4	40·4	31·1	25·0	28·6	22·4
Th ppm	27·0	31·9	19·6	19·4	16·0	12·7
$^{238}U/^{204}Pb$	8·0	7·6	7·1	8·8	0·1	0·1
$^{235}U/^{204}Pb$	0·1	0·1	0·1	0·1	0·0	0·0
$^{232}Th/^{204}Pb$	51·3	51·8	41·0	51·0	0·7	0·5
$^{206}Pb/^{204}Pb$	18·7578	18·7827	18·6488	18·7150	18·6852	18·6586
±2 SD	0·0012	0·0012	0·0012	0·0012	0·0012	0·0012
$^{207}Pb/^{204}Pb$	15·638	15·655	15·615	15·693	15·655	15·668
±2 SD	0·004	0·004	0·004	0·004	0·004	0·004
$^{208}Pb/^{204}Pb$	38·959	39·023	38·859	39·106	38·993	38·957
±2 SD	0·009	0·009	0·009	0·009	0·009	0·009
$^{206}Pb/^{204}Pb(i)$	8·7535	18·7785	18·5974	18·6245	18·6278	18·6125
±2 SD	0·0012	0·0012	0·0012	0·0012	0·0012	0·0012
$^{207}Pb/^{204}Pb(i)$	5·638	15·655	15·614	15·692	15·655	15·668
±2 SD	0·004	0·004	0·004	0·004	0·004	0·004
$^{208}Pb/^{204}Pb(i)$	38·956	39·021	38·833	39·060	38·969	38·934
±2 SD	0·009	0·009	0·009	0·009	0·009	0·009
$^{207}Pb/^{206}Pb^{*}$	0·1939	0·2026	0·1993	0·2592	0·2278	0·2418
T_{DM} $^{207}Pb/^{206}Pb$ (Ga)	2·78	2·85	2·82	3·24	3·04	3·13
$^{232}Th/^{238}U$ source†	7·8	7·8	7·8	8·0	7·9	7·9
Th/U source†	7·7	7·7	7·7	7·9	7·8	7·9
Th/U sample	6·3	6·7	5·6	5·7	4·5	5·5

	Southern Tibet						
Sample:	JPT24A	T2A	T3B	T4A	T5A	JPT 14.1	T11B
Age (Ma)	24·0	13·8	13·8	13·8	13·3	18·8	17·3
Period of analysis	b	b	b	b	b	a	b
U ppm	11·3	13·6	10·4	21·2	13·8	2·7	2·0
Pb ppm	43·7	10·3	52·7	59·6	47·0	28·4	25·8
Th ppm	54·0	118·0	68·3	146·7	79·3	16·0	9·4
$^{238}U/^{204}Pb$	11·3	13·6	10·4	21·2	13·8	2·7	2·0
$^{235}U/^{204}Pb$	43·7	10·3	52·7	59·6	47·0	28·4	25·8
$^{232}Th/^{204}Pb$	54·0	118·0	68·3	146·7	79·3	16·0	9·4
$^{206}Pb/^{204}Pb$	18·8718	19·8385	18·9236	18·7577	18·9307	18·6421	18·6602
±2 SD	0·0001	0·0001	0·0001	0·0001	0·0001	0·0012	0·0001
$^{207}Pb/^{204}Pb$	15·756	15·843	15·775	15·762	15·775	15·691	15·686
±2 SD	0·001	0·001	0·001	0·001	0·001	0·004	0·001
$^{208}Pb/^{204}Pb$	39·527	41·504	39·718	39·559	39·704	39·158	39·161
±2 SD	0·002	0·002	0·002	0·002	0·002	0·009	0·002
$^{207}Pb/^{204}Pb(i)$	18·6489	19·1523	18·8258	18·5817	18·7895	18·5785	18·6132

Table 4: continued

	Southern Tibet						
Sample:	JPT24A	T2A	T3B	T4A	T5A	JPT 14.1	T11B
±2 SD	0·0001	0·0001	0·0001	0·0001	0·0001	0·0012	0·0001
$^{207}Pb/^{204}Pb$(i)	15·753	15·834	15·773	15·760	15·773	15·690	15·685
±2 SD	0·001	0·001	0·001	0·001	0·001	0·004	0·001
$^{208}Pb/^{204}Pb$(i)	39·430	40·964	39·660	39·448	39·630	39·124	39·141
± 2 SD	0·002	0·002	0·002	0·002	0·002	0·009	0·002
$^{207}Pb/^{206}Pb^*$	0·3040	0·2625	0·2803	0·3276	0·2876	0·2685	0·2562
TDM $^{207}Pb/^{206}Pb$ (Ga)	3·49	3·26	3·36	3·60	3·40	3·30	3·22
$^{232}Th/^{238}U$ source†	8·1	7·5	7·7	8·4	8·3	8·0	7·5
Th/U source†	8·0	7·5	7·6	8·3	8·2	8·0	7·5
Th/U sample	4·8	8·6	6·6	6·9	5·7	5·9	4·8

The assigned errors were calculated from the reproducibility of the NBS 981 standard (2 SD) during the period of analysis, a, April 1999; b, June 2000. The standard values and long-term reproducibilities are given in the main text. The ratios of $^{238}U/^{204}Pb$, $^{235}U/^{204}Pb$ and $^{232}Th/^{204}Pb$ were calculated directly from the U, Th and Pb concentrations assuming natural isotopic abundances.
†The $^{232}Th/^{238}U$ value of the sample's source was calculated using the $^{207}Pb/^{206}Pb^*$ model age and the $^{208}Pb/^{204}Pb$(i) ratio of the sample. The Th/U of the source was calculated from the $^{232}Th/^{238}U$ value of the sample's source, assuming natural isotope abundances of Th and U. Comparison with the actual Th/U of the sample (data taken from Table 2) shows that most samples have Th/U slightly lower than that inferred for their source region.

place in the deep mantle in the presence of residual K-clinopyroxene viable as (1) residual clinopyroxene would result in near horizontal trends of CaO against MgO and SiO_2, which are not observed (CaO vs MgO, Fig. 4a; CaO vs SiO_2, not shown), and (2) the high pressures coupled with the high mantle potential temperatures required for the generation of these alkaline melts (1300–1500°C; Tsuruta & Takahashi, 1998) would result in a long melting column and significantly larger volumes of magmatism than are apparent on the Tibetan plateau.

In the south-west and south–central southern groups, the presence of such a 'K anomaly' is more difficult to verify because the abundances of Th and U are elevated with respect to Rb and Ba. One possibility is that there is a residual phase present that selectively retains Rb, Ba and K during partial melting with respect to Th and U. Another is that such a phase is residual during low-pressure fractional crystallization in the crust. On the plot of Rb vs MgO (Fig. 4f) it can be seen that Rb correlates positively with Mg in the south-west and Pabbai Zong groups. This could reflect fractionation of a Rb (and also K, Ba) bearing phase; it could also reflect assimilation of a crustal component with a low Rb and high SiO_2 content. To further resolve this issue, we need to address the degree to which crustal assimilation and fractional crystallization (AFC processes, DePaulo, 1981) can explain the trace element variations in the Tibetan samples, and examine how they may be corrected for without overprinting genuine trace and major element compositional variations that are due to partial melting processes or source region heterogeneity.

Variation of major and trace elements with MgO and correction for AFC processes

In the south-west, Pabbai Zong and all three northern groups, Sr is positively correlated with MgO (Fig. 4e), and, in the south-west and Pabbai Zong groups Rb is also correlated with MgO. These trends suggest a major role for amphibole and/or mica (e.g. biotite, phlogopite) during crystal fractionation [which does not in itself preclude the presence of these phases in the mantle or crustal source region(s) of the magmas], but could also reflect binary mixing between melts with different source region compositions or AFC processes. Crustal contamination is an unlikely mechanism to explain the positive trends with MgO, as the Rb content of the most magnesian sample (T2A, 643 ppm) is many times that of continental crust (bulk continental crust 32 ppm, upper continental crust 112 ppm; Taylor & McLennan, 1995). There are also weak correlations between Ce and Sm (and the other REE, not shown) with MgO (Fig. 4g and h) in the south-west and Pabbai Zong groups; the north-west and north–central groups also show a slight positive correlation between Sm and MgO. These trends can be considered in the

light of a number of processes: crustal assimilation, AFC, binary mixing between different melts derived from different mantle source regions, and partial melting.

Comparing the behaviour of Ce and Cr in the southern samples allows the relative importance of these processes to be evaluated, as both Ce and Cr exhibit positive correlations with MgO (Fig. 4d and g). Positive correlations of Cr with MgO are a common feature of mafic to intermediate igneous suites and are generally considered to reflect the compatibility of Cr in spinel and clinopyroxene phases. In contrast, Ce is widely regarded as an incompatible element in the majority of mantle phases (e.g. Halliday *et al.*, 1995). Although there is a slight positive correlation between Ce and Cr in the south-west and Pabbai Zong samples (Fig. 8a), which could indicate a binary mixing relationship, the array defined by the south-west and Pabbai Zong samples on the $\varepsilon Nd_{(i)}$ vs $100 \times Ce/Cr$ plot (Fig. 8b) is not consistent with a binary mixing curve between the two most 'extreme' south-west samples (20E39A and JPT24C). Therefore, the positive relationship of Ce (and Cr) with MgO must have originated through either crystal fractionation or melting, or some combination of these processes.

The sample data (Fig. 8c) are compared with models (Fig. 8d) that investigate the influence of melting and AFC processes on Cr behaviour relative to MgO. The models' details are given in the figure caption. Mg is treated as a trace element, following Pearce & Parkinson (1993). Although the behaviour of MgO is controlled by phase relationships, and more complex than allowed for, we consider that the approach adopted here is the most effective way to model trace element and major element compositions simultaneously. A more detailed study of the behaviour of MgO during melting is not required in this particular case, as we use these models simply to demonstrate that melting processes alone cannot explain the arrays defined by the south-west and Pabbai Zong samples in the Ce–Cr vs MgO plots.

Figure 8d demonstrates that the variation in Cr and MgO contents of the southern samples are most easily explained in terms of fractional crystallization, as melting trends are essentially vertical (for small degrees of melting). The effects of assimilation are negligible, as can been seen from the similarity of model curves using $r = 0{\cdot}2$ and $r = 0{\cdot}8$. This is due to the high concentrations of this element in the mafic end-members relative to the crust.

In Fig. 8f, the partial melting curves for Ce vs MgO are essentially vertical (for melt fractions of 0–4% partial melting), which is a function of the large contrast in the partition coefficients of Ce and Mg. Such vertical trends are also produced by melting eclogite or pyroxenite lithologies for the same reason. Comparison of these model curves with the sample data (Fig. 8e) indicates that partial melting processes alone cannot explain the trends of Ce vs Mg shown by the south-west and Pabbai Zong samples. In Fig. 8f, AFC curves are essentially flat, only showing large deflections and sensitivity to the value of r used in the model when there are very small fractions of remaining melt. This is a function of the extremely high Ce concentrations in the mafic end-members (T2A 315 ppm Ce; peridotite melt 127 ppm Ce) relative to the assimilant (45 ppm Ce). As it is widely accepted that the time scales of potassic magma emplacement (i.e. the period between mantle source melting and eruption or intrusion into the crust) are very short because of the high volatile contents of the magmas (Spera, 1987; Kelley & Wartho, 2000), it is unlikely that the shoshonitic Tibetan magmas had protracted fractionation histories in the crust. However, variably small degrees of partial melting can easily generate considerable variation in the Ce compositions of the resulting magmas at near-invariant MgO contents. Therefore, although neither melting nor fractionation processes alone can generate the positive array of Ce with MgO, a combination of these processes can, provided the mafic end-members in AFC processes are formed by different degrees of partial melting.

It is interesting to note that, in the melting models presented in Fig. 8d and f, a mantle peridotite source region would have to have 41·0 wt % MgO, 4706 ppm Cr and 10·5 ppm Ce to generate a 1% melt with the same composition as sample T2A. In a model where no residual melt is used [modal abundances and melt modes in parentheses: olivine 0·58 (0·19); orthopyroxene 0·27 (0·25); clinopyroxene 0·13 (0·52); aluminous spinel 0·02 (0·04)] the required composition is 41·2 wt % MgO, 4734 ppm Cr and 8·48 ppm Ce. The MgO and Cr required by this model are significantly greater than those estimated for the primitive mantle (37·8 wt % MgO and 2580 ppm Cr), which implies (if assumptions regarding the mineralogy of the mantle source region and melting regime are correct) a mantle source that has experienced earlier melt extraction events. Similarly, these calculations imply that the Ce content of the mantle source must be 5–6 times the content estimated for the primitive mantle (1·775 ppm; Sun & McDonough, 1989). A multi-stage source history with LREE enrichment following heavy REE (HREE) depletion by melt extraction could explain these observations. However, these comparisons have not taken into account differences in melting regime, the presence of hydrous phases and the source region lithology (e.g. pyroxenite or eclogite as opposed to peridotite). These issues are addressed further in the following sections.

The importance of the near-orthogonal relationships between the AFC and melting curves in Fig. 8d and f is

that they allow the effects of AFC processes to be differentiated from those of partial melting processes, and thus corrected for. Furthermore, the melting trends for all the highly incompatible to incompatible trace elements are also nearly vertical, which is a function of the large contrast in their bulk partition coefficients compared with that of MgO.

To correct for the majority of AFC processes and crystal accumulation, we have extrapolated the concentrations of all major and trace elements back to 6 wt % MgO by fitting linear least-squares regression lines to the northern and southern data arrays and using the slopes of the regressed lines to correct the data (Klein & Langmuir, 1987; see also Turner & Hawkesworth, 1995, for a graphical illustration of the technique). This process was applied to all the trace element compositions of the more mafic lavas (MgO $>2{\cdot}8$ wt %). As melting trends for all elements are nearly vertical, this correction does not hide variations in trace element concentrations that arise from partial melting processes, or from mantle source heterogeneity. This approach to fractionation correction has the major advantage that it avoids *a priori* assumptions regarding the nature of the fractionating assemblages. Only

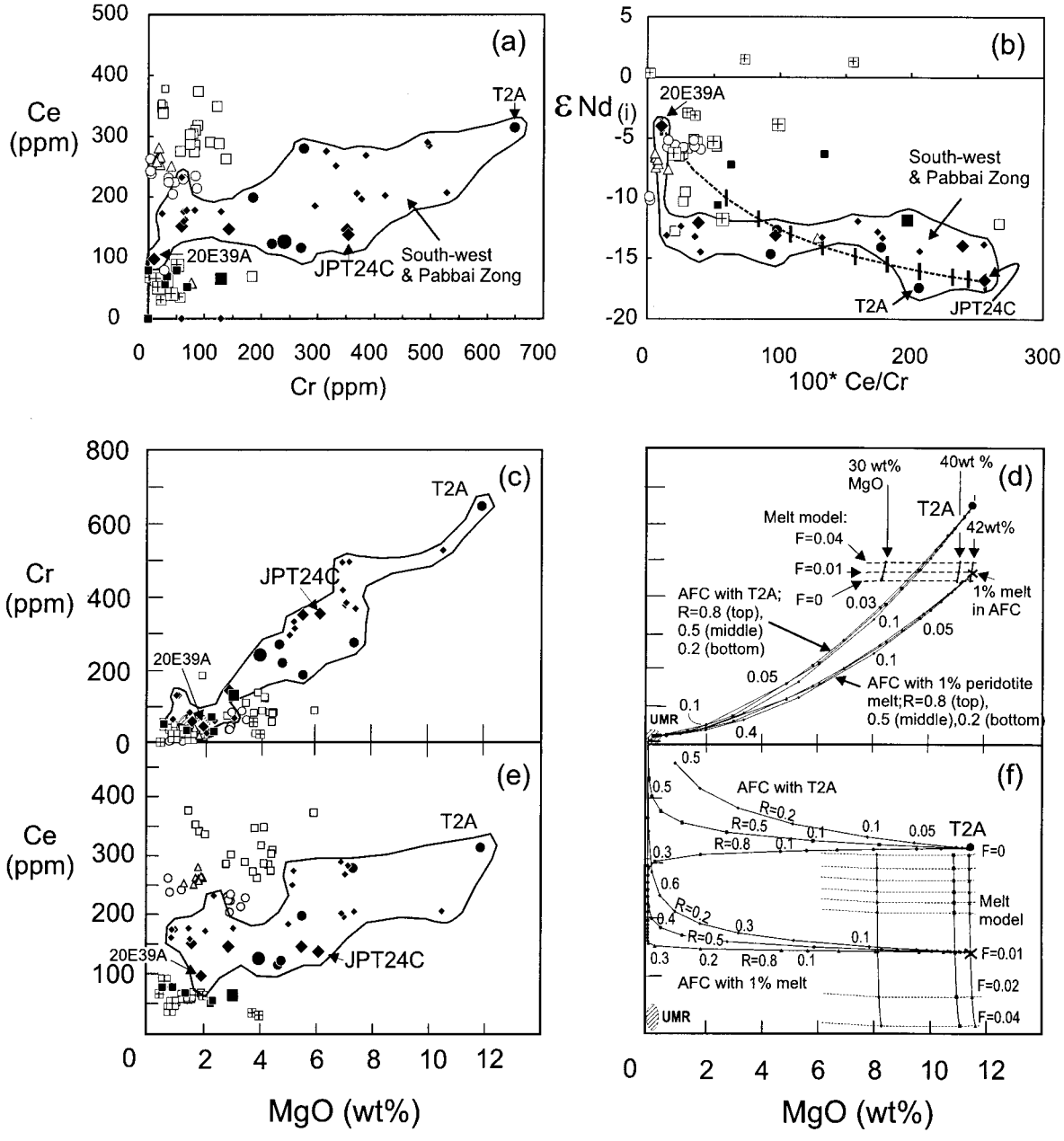

samples with MgO >2·8 wt % were used to minimize errors resulting from over-extrapolation, thus restricting the study to samples from the south-west, Pabbai Zong, north-west and north–central groups. The samples from southern Tibet were treated as a single dataset for regression and the northern samples were also treated in this way, forming a second dataset. The samples used in these two 'regression datasets' are listed in the Appendix.

Although combining sample groups may obscure minor differences between melting regimes and crustal fractionation histories in the individual locality groups, it provides a means of making broad-scale comparisons between the mantle source regions and melting regimes of potassic magmatism in southern and northern Tibet, which is one of the main objectives of this paper. Despite the fact that 6 wt % MgO is too low for the calculated compositions to be representative of primary magmas, this value is appropriate for the range shown by the available data, corrects for the majority of fractionation effects, and provides a common point for comparison of samples between, and within, the two magma groups. Given that crustal contamination is likely to accompany fractionation processes (DePaolo, 1981) extrapolation to 6 wt % MgO will also remove much of the effects of crustal assimilation.

Comparison of major element compositions at 6 wt % MgO and constraints on source lithology and composition

Comparison of major element compositions corrected to 6 wt % MgO reveals that there are considerable differences in the normalized major element compositions of the two groups: the southern samples are displaced to lower $Fe_2O_3^*{}_{(6)}$, $TiO_{2(6)}$, $CaO_{(6)}$ and higher $SiO_{2(6)}$ relative to the northern group (Fig. 9a–d). The $Al_2O_{3(6)}$ compositions of both groups are similar. Given that the regression to 6 wt % MgO will have reduced much of the effects of low-pressure crystal fractionation and crustal assimilation, the corrected major element compositions can now be compared directly with the compositions of glasses from melting experiments on peridotite, pyroxenite and eclogite starting materials. The compositions of such glasses are analogous to 'liquid compositions' produced during partial melting. The aim of such comparisons is to determine whether the differences in the major element compositions of the northern and southern samples can explained by differences in source region lithology (i.e. whether the source region consists of peridotite, pyroxenite and eclogite lithologies and in what relative proportions) or differences in mantle source region major element composition.

Fig. 8. (opposite) (a) Ce vs Cr in the southern and northern Tibetan shoshonites; symbols and groups as in Fig. 2. Individual southern samples (T2A, 20E39A and JPT24C) are identified on the diagram. Isotope and trace element data for sample T2A are from Williams *et al.* (2001); trace element and isotope data for the other two samples are presented in Tables 2 and 3, respectively. (b) $\varepsilon Nd_{(i)}$ vs 100 × Ce/Cr; symbols and groups as in Fig. 2. As in (a) the field defines the south-west and Pabbai Zong samples and the samples T2A, 20E39A and JPT24C are plotted. It is important to note that JPT24C is not the most primitive sample in the south-west–Pabbai Zong group—this is sample T2A (11·8 wt % MgO; 314 ppm Ce; 649 ppm Cr). The dashed line with tick marks is a binary mixing curve between the two samples (20E39A and JPT24C) in the south-west–Pabbai Zong group that have the most extreme $\varepsilon Nd_{(i)}$ and 100 × Ce/Cr ratios. The mixing proportions are in increments of 0·1 (10%). (c) Variation of Cr with MgO in the Tibetan samples, and (d) fractional melting curves and AFC models in Cr–MgO space. (e) Variation of Ce with MgO for Tibetan samples, and (f) fractional melting curves and AFC models in Ce–MgO space. Diagrams (c) and (d), and (e) and (f) have the same scales to facilitate comparisons between the data arrays and the model curves. The non-modal modal fractional (with 1% residual melt present) melting curves plotted in (d) and (f) are for spinel peridotite sources and melt fractions of 1–4%. The model used is a modification of a pure fractional melting model. In the case of fractional melting, the melt 'packets' are instantaneously extracted from the source before reaching equilibrium with the source region, whereas in this model, we allow 1% of the melt generated to remain in equilibrium with the source, while the rest is extracted. This 'residual melt' phase has a partition coefficient (i.e. *D* residual melt/new melt) of unity for all elements and a modal abundance of 0·01 and a melting mode (i.e. the degree to which it can enter the new melt) of 0·01. The modal abundance has the same value as the melting mode because the residual melt is fully in equilibrium with the source and the new melt. This model provides a mid-point between pure fractional melting and batch melting (where all the melt generated remains in equilibrium with the source). The mineral assemblages and melting modes (in parentheses) are as follows: olivine 0·575 (0·19); orthopyroxene 0·27 (0·25); clinopyroxene 0·125 (0·5); aluminous spinel 0·02 (0·05); residual melt in equilibrium 0·01 (0·01). Mineral–melt partition coefficients for Ce in olivine, orthopyroxene and clinopyroxene are taken from Halliday *et al.* (1995), a partition coefficient of 0·01 is assumed for spinel after McKenzie & O'Nions (1991). Mineral–melt partition coefficients for Cr and Mg are those estimated by Pearce & Parkinson (1993) for a spinel peridotite at 1200°C. Partition coefficients for Ce, Cr, Mg between melt generated and residual melt are assumed to be equal to unity, as explained above. Three starting compositions are shown, with 30, 40 and 42 wt % MgO, and all with 3·5 ppm Ce and 3330 ppm Cr. The Ce and Cr compositions are not those of primitive mantle, which are 1·775 ppm and 2580 ppm, respectively, but are selected to yield a 1% melt that corresponds to the average of the Ce and Cr compositions of the south-west and Pabbai Zong samples. The melting curves show that partial melting processes produce near-vertical trends of Ce and Cr against MgO, irrespective of whether the starting peridotite is highly magnesian (>42% MgO) or not (37·8 wt % MgO). The AFC curves in (d) and (f) are constructed after DePaulo (1981) using the primitive sample T2A as the mafic end-member, or, for comparison, a 1% melt of spinel peridotite, calculated using the melting assemblage above and which is shown on the melting curves (melt composition 11·7 wt % MgO; 127 ppm Ce, 460 ppm Cr; melt source 42 wt % MgO, 3·5 ppm Ce, 3330 ppm Cr). In both cases the average composition of the northern Tibetan Ulugh Muztagh rhyolites (McKenna & Walker, 1990) is taken as a proxy for the crustal assimilant as no equivalent is available for southern Tibet. The composition of this assimilant is 0·13 wt % MgO, 45 ppm Ce, 5 ppm Cr. The AFC curves use three different values of *R* (the ratio of assimilation to crystal fractionation): 0·2, 0·5 and 0·8, to explore the effect of varying crustal assimilation; the ticks on the AFC curves are the proportion of the melt that has crystallized.

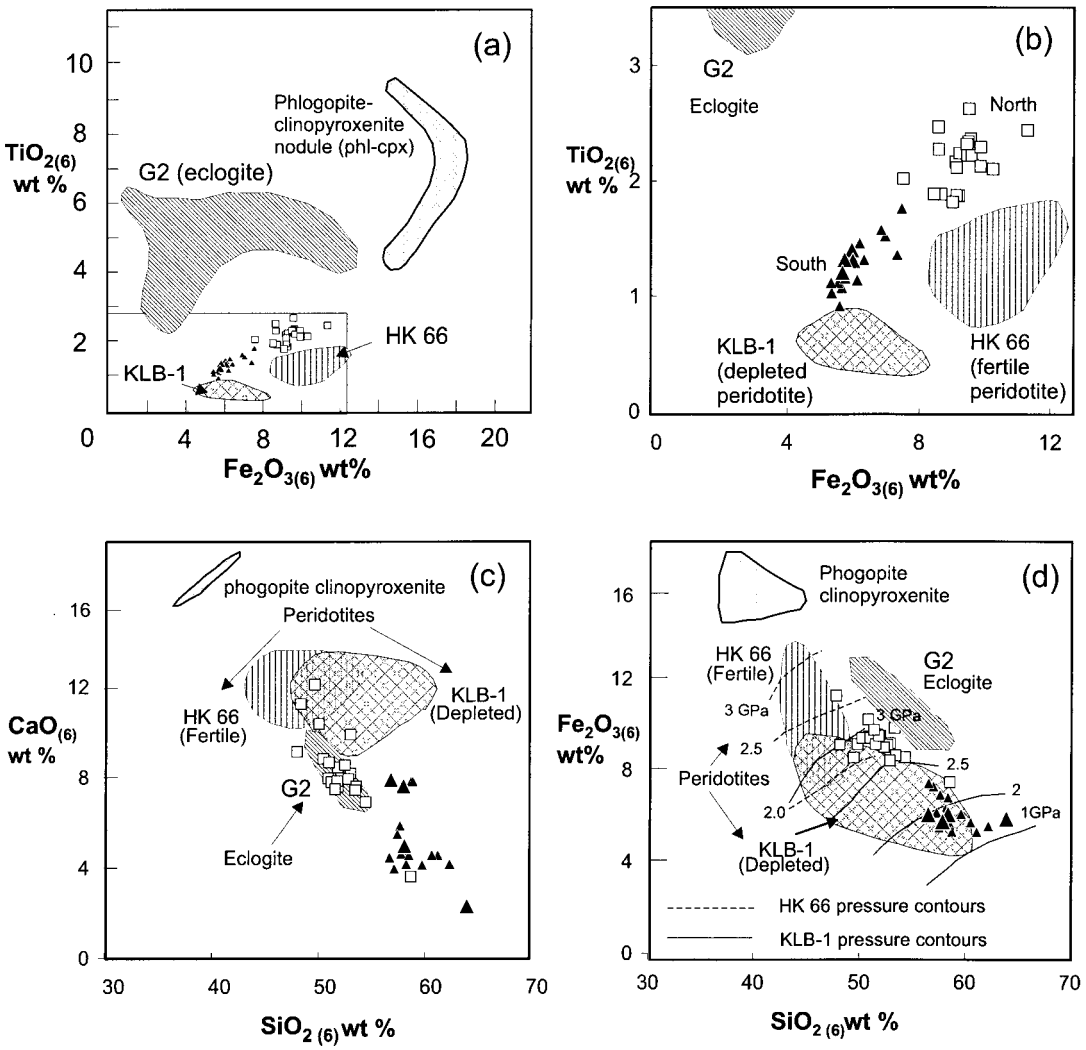

Fig. 9. (a) $Fe_2O_{3(6)}$ vs $TiO_{2(6)}$, for the northern and southern Tibetan samples; (b) enlargement of (a); (c) $CaO_{(6)}$ vs $SiO_{2(6)}$; (d) $Fe_2O_{3(6)}$ vs $SiO_{2(6)}$. The southern samples that have been treated as a single regression dataset are shown as filled triangles; large triangles denote samples for which new data are presented in this study (Table 2), small triangles denote samples for which major element data have been published (data sources are given in Fig. 2). The northern samples that were regressed to 6 wt % MgO are shown as open squares; all the major element data from these samples are from the sources listed in Fig. 2. The shaded fields define the compositional ranges of glasses [normalized to $MgO_{(6)}$ by addition of Fo_{90}] produced in peridotite, eclogite and pyroxenite melting experiments at a range of pressure and temperature conditions (see main text for details).

We made a compilation of the major element compositions of glasses produced by partial melting experiments on a natural anhydrous fertile spinel peridotite (HK-66; Hirose & Kushiro, 1993), a natural anhydrous depleted spinel peridotite (KLB-1; Takahashi, 1986; Hirose & Kushiro, 1993; Hirose & Kawamoto, 1995; Hirose, 1997), an artificial eclogite/garnet clinopyroxenite made from a mixture of natural garnet and clinopyroxene in proportions that give a major element composition approximating that of subducted oceanic crust (G2; Pertermann & Hirschmann, 2003*a*, 2003*b*) and a natural phlogopite clinopyroxenite nodule with minor apatite and titanomagnetite (Lloyd *et al.*, 1985). All the experimental data were corrected to 6 wt % MgO by removal of Fo_{90} [composition taken from Deer *et al.* (1992)] from their major element composition and the totals were normalized to 100. The shaded fields for depleted peridotite KLB-1 and the fertile lherzolite HK-66 define the results of melting experiments carried out at conditions ranging from 0·2 to 3·0 GPa and 1100 to 1375°C at melt fractions of $<30\%$. The experimental data of Pertermann & Hirschmann (2003*a*, 2003*b*) define the shaded field labelled G2 and were generated at melting conditions of 3·0 GPa and temperatures ranging from 1250 to 1375°C. The experimental data of Lloyd *et al.* (1985),

which define the shaded field labelled phlogopite-clinopyroxenite, were carried out at melting conditions of 3 GPa and temperatures of 1200–1250°C.

Although it would clearly have been ideal to compare experiments on different starting materials at similar ranges of temperature and pressures (and hence proportions of melting), we were limited by the available data and it was only possible to contour the HK-66 and KLB-1 fields for pressure on the $Fe_2O_3^{*}{}_{(6)}$ vs $SiO_{2(6)}$ plot (Fig. 9d). It was not possible to contour these fields on the other diagrams as $CaO_{(6)}$ and $TiO_{2(6)}$ do not show clear dependence on temperature, pressure or melt fraction relative to $SiO_{2(6)}$. One problem that is especially pertinent to this study is the lack of data for very small degrees of melting for a range of starting bulk compositions, which is due to difficulties in analysing very small volumes of glass in an experimental charge. Therefore, we have opted for a broad range of conditions that we believe could be applicable to the petrogenesis of the Tibetan samples, and, in this comparison, we do not consider experimental data over 1400°C and over 3·0 GPa, as higher temperatures and pressures would produce large volumes of melt, which are not in accord with the sparse distribution of magmatism on the plateau.

In Fig. 9a–d, it is apparent that the southern and northern samples define two separate groups that do not overlap. Although a considerable degree of variation in major element compositions could be caused by partial melting processes, it is unlikely that they can explain the differences between the Tibetan sample groups, as the compositional range defined by both Tibetan groups is generally greater than the range in the melt compositions for any of the four starting materials. For example, $Fe_2O_3^{*}{}_{(6)}$ increases strongly with increasing pressure (contours in Fig. 9d). Moreover, if the southern and northern samples were to be explained by melting of a single source region then polybaric melting, from ~3·5 to ~1 GPa, would be required (for a source region with a KLB-1 composition and mineralogy) to generate the range of $Fe_2O_3^{*}{}_{(6)}$ and $SiO_{2(6)}$ compositions. This is unlikely as it would imply a long melting column, and hence larger degrees of melting than are compatible with the volumes of mafic lavas inferred to have erupted on the plateau. Thus, the contrasting major element systematics of the northern and southern samples must dominantly reflect differences in source region composition and mineralogy.

In the plot of $TiO_{2(6)}$ against $Fe_2O_3^{*}{}_{(6)}$ (Fig. 9a), it can be seen that both the southern and northern sample groups have $TiO_{2(6)}$ values that are substantially lower than the liquid (glass) compositions derived by partial melting of the phlogopite-clinopyroxenite and the artificial G2 eclogite starting materials. The enlargement of this plot (Fig. 9b) demonstrates that the displacement of the southern samples to lower $TiO_{2(6)}$ and $Fe_2O_3^{*}{}_{(6)}$ values relative to the northern samples echoes the displacement of the liquid compositions of KLB-1 (depleted peridotite) relative to HK-66 (fertile peridotite). This could indicate a more depleted source region for the southern samples, but this interpretation assumes peridotite source regions for both sets of samples, which may not necessarily be the case.

The plot of $CaO_{(6)}$ against $SiO_{2(6)}$ (Fig. 9c) demonstrates that the southern samples have significantly higher $SiO_{2(6)}$ and lower $CaO_{(6)}$ values relative to the northern samples. The northern samples with the highest $CaO_{(6)}$ values overlap the compositions of liquids derived by partial melting of HK-66 and KLB-1, but the northern sample array extends to lower $CaO_{(6)}$ and higher $SiO_{2(6)}$ values, which fall in the G2 field. The southern samples do not plot within any of the liquid composition fields. In Fig. 9d, the northern samples plot closest to liquids in equilibrium with the fertile peridotite HK-66, whereas the southern samples have lower $Fe_2O_3^{*}{}_{(6)}$ values and higher $SiO_{2(6)}$ values relative to the northern group, and plot closest to the field of melts in equilibrium with the depleted peridotite KLB-1. Both sample groups display lower $Fe_2O_3^{*}{}_{(6)}$ values compared with liquids in equilibrium with the eclogite G2, at similar $SiO_{2(6)}$ values. Neither the northern nor the southern sample group plots near the field of phlogopite-clinopyroxenite melts in any of the $MgO_{(6)}$ plots (Fig. 9a–d), effectively ruling out a pyroxenite source region for both groups.

Determining whether the source regions of the northern and southern samples have peridotite or eclogite lithologies (or both) is a more complex issue. The northern and southern samples have $TiO_{2(6)}$ values that are higher than those of peridotite (fertile and depleted) melts, yet lower than those of melts in equilibrium with the eclogite G2. The Tibetan samples also have very low $CaO_{(6)}$ values, which are more similar to melts in equilibrium with the eclogite G2 than to peridotite melts. The high $TiO_{2(6)}$ values of the sample groups relative to melts in equilibrium with fertile and depleted peridotites can be explained if Ti is behaving as an incompatible element and the Tibetan samples are derived by lower degrees of melting than the peridotite experimental melts. This is plausible, as the liquids in equilibrium with HK-66 and KLB-1 were derived by 6–20% partial melting, and it is unlikely that the Tibetan samples were produced by such high degrees of melting, given their sparse distribution on the Tibetan plateau and their high degree of incompatible element enrichment.

The high $TiO_{2(6)}$ values of partial melts of the eclogite G2 are a function of the relatively high $TiO_{2(6)}$

values of the starting material [2·04, higher than the Sun & McDonough (1989) primitive mantle value of 1·29]. None the less, direct comparisons between the $TiO_{2(6)}$ values of the Tibetan samples and G2 partial melts are valid, as the G2 composition is considered to be a reasonable approximation of the composition of subducted oceanic crust [see discussion by Pertermann & Hirschmann (2003*a*)], and its $TiO_{2(6)}$ value is representative of 'typical' eclogite compositions (Becker *et al*., 2000). Thus, the difference between the $TiO_{2(6)}$ values of the Tibetan samples and that of the G2 partial melts (north Tibet, average, 1·82 wt %; south Tibet average, 1·07 wt %; G2, 5·06 wt %) requires that Ti is retained in the source region during partial melting beneath Tibet. This can be achieved by the presence of residual Ti-bearing phase(s) in the source region(s) of the southern and northern samples. This could be a plausible explanation given that the G2 eclogite partial melts were derived by much higher degrees of partial melting (3·0–20% partial melting (Pertermann & Hirschman, 2003*a*) relative to the Tibetan samples (1–3%; Turner *et al*., 1996; Miller *et al*., 1999) because, if residual Ti-bearing phase(s) are present, then the retention of Ti in the source will be greatest for the smallest melt fractions. This hypothesis will be tested in the following section.

Although invoking the presence of eclogite source region(s) would explain the low $CaO_{(6)}$ values of the northern and southern groups, the low $CaO_{(6)}$ values of the Tibetan samples could also be reconciled by derivation from peridotite source regions that have low modal clinopyroxene contents compared with the peridotites HK-66 and KLB-1 (14% and 15%, respectively; Hirose & Kushiro, 1993). The low clinopyroxene contents are required because the degrees of melting that previous workers have invoked for the genesis of the Tibetan potassic magmas ($\sim$2–3%; Turner *et al*., 1996; Miller *et al*., 1999) are not sufficient to exhaust $\sim$15 modal % clinopyroxene from a peridotite (typically, clinopyroxene is consumed at 23–25% partial melting; McKenzie & Bickle, 1988; Walter, 1998).

To summarize, the major element data indicate that the northern and southern sample groups were derived by partial melting of sources that were distinct in terms of their composition and/or their mineralogy. Comparison of the normalized compositions of the Tibetan samples with those of liquids derived by partial melting of phlogopite clinopyroxenite, eclogite, fertile and depleted peridotite starting materials reveals that phlogopite clinopyroxenite is not a viable source region lithology for either group. However, it does not unambiguously rule out either peridotite or eclogite source regions in the petrogenesis of the northern and southern Tibetan samples.

Peridotite vs eclogite source regions and the role of residual Ti-bearing phases

In the previous section, it was argued that the low $TiO_{2(6)}$ contents of the Tibetan samples can be reconciled with their derivation from eclogite source region(s) only if it can be shown the Ti contents of small degree eclogite melts (below 2% partial melting) can be significantly lowered to compositions similar to the Tibetan samples by the presence of residual Ti-bearing phases.

If Ti* represents the expected content of Ti in a mafic rock, based on the logarithmic average of elements equally spaced before and after it on a primitive mantle normalized diagram, and Ti represents the observed concentration, then the Ti/Ti* value can be used as a measure of the magnitude of the 'Ti anomaly' on a primitive mantle normalized multi-element diagram. Plots of this parameter against other trace-element parameters can be used to determine whether negative Ti anomalies can be explained by negative anomalies in the mantle source or by partial melting processes. In Fig. 10a (and its enlargement, b) the Ti/Ti* values of the northern and southern samples are plotted against La/Yb(n). Partial melting curves have been plotted in Fig. 10a to evaluate changes in the Ti/Ti* value with La/Yb(n) and with the degree of partial melting in a source bearing residual rutile. It is stressed that, although a residual Ti-bearing phase is required to generate Ti anomalies, this phase does not actually have to be rutile: Ti-bearing amphiboles, micas or titanite could also serve to hold Ti back in the source region if they are residual during partial melting. Rutile was selected in this case as its presence on the solidus during eclogite melting has been experimentally demonstrated (Pertermann & Hirschmann, 2003*a*). It is also important to emphasize that the evolution of the Ti anomaly with La/Yb(n) is not dependent on the absolute concentration of Ti in the source, provided that the source composition modelled does not show a Ti anomaly when plotted on a primitive mantle normalized multi-element diagram.

The details of the model are given in the caption to Fig. 10. The model curves show that Ti/Ti* falls most sharply against La/Yb(n) between 20 and 5% partial melting, irrespective of the modal abundance of rutile in the source region. At degrees of melting between 5 and 1%, there is minimal change in the value of Ti/Ti* with respect to La/Yb(n) for all three model curves. For a source with 3% rutile, the Ti/Ti* value falls from 0·64 to 0·53 between 20 and 10% partial melting, to 0·49 at 5% partial melting, and then to 0·46 at 1% partial melting. Thus, the Ti/Ti* value decreases by less than one-third between 20% and 1% melting. This is not sufficient to explain the discrepancy between the

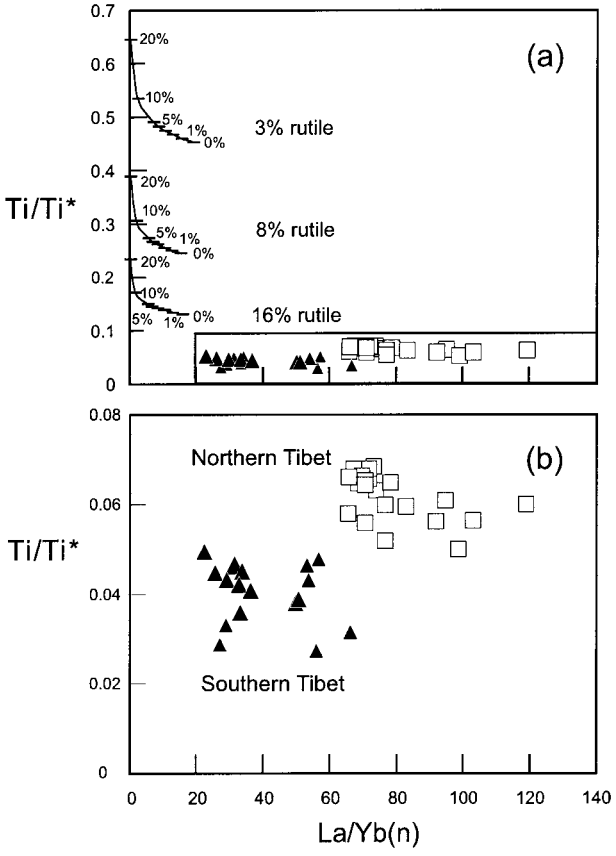

Fig. 10. (a) Plot of Ti/Ti* vs La/Yb(n); (b) enlargement of this plot. The sample groups and symbols are the same as in Fig. 9. La and Yb abundances have been corrected to 6 wt % MgO (see Appendix for regression statistics, slopes and intercepts) and normalized to primitive mantle (Sun & McDonough, 1989). Ti/Ti* is the ratio of the observed concentrations of Ti relative to those predicted by the logarithmic average of the primitive mantle normalized abundances of the two elements spaced equally on either side of Ti in a primitive mantle normalized spidergram. Here, the value of Ti* is calculated as $\sqrt{[Sm_{(N)} \times Tb_{(N)}]}$; Sm and Tb were selected as the pair of elements to reference Ti to as the alternative pair, Eu and Gd, is problematic because Eu has the potential to display negative anomalies in the presence of residual plagioclase feldspar. A fractional melting model with 1% residual melt (see caption to Fig. 8) and a primitive mantle source composition (Sun & McDonough, 1989) were used. Melt modes were calculated to allow for garnet exhaustion before clinopyroxene, and the presence of clinopyroxene and rutile on the solidus throughout the melting interval from 0 to 100%, as this has been observed in eclogite melting experiments (Pertermann & Hirschmann, 2003*a*). The modal abundances and melt modes (in parentheses) are: '3% rutile', rutile 0·03 (0·01), clinopyroxene 0·79 (0·40), garnet 0·17 (0·48), residual melt 0·01 (0·01); '8% rutile', rutile 0·08 (0·01), clinopyroxene 0·79 (0·40), garnet 0·12 (0·48), residual melt 0·01 (0·01); '16% rutile', rutile 0·08 (0·01), clinopyroxene 0·71 (0·40), garnet 0·12 (0·48), residual melt 0·01 (0·01). The partition coefficients used are given in the Appendix, the data sources are: Green *et al.* (2000) for the REE partition coefficients in clinopyroxene and garnet; Halliday *et al.* (1995) for Ti partition coefficients in clinopyroxene and garnet; Foley *et al.* (2000) for the REE partition coefficients in rutile; the partition coefficient of Ti in rutile was calculated after Ryerson & Watson (1987) as no direct measurements of the Ti partitioning between melt and rutile are yet available.

$TiO_{2(6)}$ values of the Tibetan samples (north, average $TiO_{2(6)} = 1{\cdot}82$ wt %; south, average = 1·07 wt %; for 1–3% partial melting, Turner *et al.*, 1996; Miller *et al.*, 1999) and the eclogite experimental liquids (average 5·06 wt %, for 3–20% partial melting). Although this model does not rule out the presence of a Ti-bearing phase in the source region of either the northern or southern sample groups, it does indicate that the presence of such a phase does not retain Ti sufficiently to explain the discrepancy between the $TiO_{2(6)}$ values of the Tibetan samples and the eclogite melts. Therefore, we conclude in this section that an eclogite source region for both the northern and southern Tibetan sample groups is not viable and we will focus exclusively on mantle peridotite source regions in the remainder of this paper. This conclusion is also evidence against the derivation of the southern Tibetan samples by partial melting of the subducting Indian slab, and thus suggests a metasomatized peridotite source region in the Asian SCLM. A metasomatized peridotite source with residual K-bearing phase(s) is consistent with crystallization temperatures of 1050–1100°C estimated from coexisting clinopyroxene and orthopyroxene for the northern samples (Turner *et al.*, 1996), which lie on or above the position of the hydrated peridotite solidus at 1040–1050°C and pressures of 1·8–2·5 GPa (Wallace & Green, 1991).

Thus, in the context of peridotite source regions, the lower $Fe_2O_3^{*}{}_{(6)}$, $TiO_{2(6)}$, $CaO_{(6)}$ and higher $SiO_{2(6)}$ values of the southern group relative to those of the northern group suggest that their mantle source region has lower modal proportions of clinopyroxene and had experienced a greater degree of depletion. A refractory mantle source for the southern mafic samples is consistent with the high Cr contents of the most primitive samples (Fig. 4d). This depletion of the northern and southern Tibetan SCLM source regions must have taken place prior to metasomatism. Such multi-stage source histories require the isolation of the source regions from the convecting asthenosphere, and provide further support for source regions located in the SCLM beneath Tibet.

Isotope geochemistry

Sr and Nd isotope geochemistry

The high incompatible element concentrations of the most primitive magmas (i.e. those that comprise the regression datasets with >2·8 wt % MgO) relative to average continental crust (Taylor & McLennan, 1995) render the trace element signatures of these Tibetan lavas highly insensitive to modification by crustal assimilation. For southern Tibet, the respective ranges in compositions, including published data, are: Th, 54–192 ppm; Ce, 116–290 ppm; Pb, 44–128 ppm;

Sr, 372–1115 ppm; Nd, 64–200 ppm. Corresponding ranges for the northern sample regression dataset are: Th, 9–50 ppm; Ce, 205–373 ppm; Pb, 25–41 ppm; Sr, 899–2120 ppm; Nd, 81–164 ppm. The minimal correlations between either $^{87}Sr/^{86}Sr_{(i)}$ or $\varepsilon Nd_{(i)}$ and SiO_2 (Fig. 6b) demonstrate that the isotopic signatures of the more primitive northern and southern samples used in the $MgO_{(6)}$ regression datasets are largely insensitive to assimilation processes, and therefore must reflect the composition of their source regions. The absence of significant Eu anomalies in the most primitive samples from the southern and northern groups, combined with their extremely high incompatible element concentrations relative to average continental crust, also argues against a crustal source. This is in agreement with the fact that the $^{87}Sr/^{86}Sr_{(i)}$ compositions (0·7123–0·739) of the south-west and Pabbai Zong samples are more radiogenic than the proxy for the time-integrated $^{87}Sr/^{86}Sr$ composition of the Lhasa Terrane crust (Fig. 6a: the Amdo orthogneiss of Harris *et al*., 1988). The radiogenic $^{87}Sr/^{86}Sr_{(i)}$ and unradiogenic $\varepsilon Nd_{(i)}$ signatures of these samples and their enrichment in the highly incompatible trace elements relative to primitive mantle point to an SCLM source region. This is in agreement with the inferences based on $MgO_{(6)}$-normalized major element data, that the Tibetan samples were derived by partial melting of mantle peridotite, rather than eclogite or pyroxenite, source regions.

In combination with the $Mg_{(6)}$-normalized major element values, which cannot be explained by the melting of a single mantle source region, the Sr and Nd isotope data suggest the presence of isotopically distinct source regions. The range in $^{87}Sr/^{86}Sr_{(i)}$ shown by the south-west and Pabbai Zong samples indicates variation in the Rb/Sr of the source, whereas the more restricted array of the more mafic northern samples in Sr–Nd space [Fig. 6; ranges for the regressed dataset are $^{87}Sr/^{86}Sr_{(i)}$ 0·7047–0·7102; $\varepsilon Nd_{(i)}$ −12·7 to −5·1] implies a source characterized by more variable Sm/Nd than Rb/Sr. Such isotopic heterogeneities may be interpreted in terms of the variable proportions of peridotite host and metasomatic vein material involved in partial melting processes (Foley, 1992*b*). The south-east and south–central samples are distinct from the south-west and Pabbai Zong groups (the latter are combined in the regressed south Tibet dataset) in that they form relatively vertical arrays and the south-east array extends to Bulk Earth $^{87}Sr/^{86}Sr_{(i)}$ and $eNd_{(i)}$ values.

Pb isotope geochemistry

The steep arrays defined by the northern and southern lavas on the $^{207}Pb/^{204}Pb_{(i)}$ and $^{208}Pb/^{204}Pb_{(i)}$ vs $^{206}Pb/^{204}Pb_{(i)}$ plots (Fig. 7a–d) cannot be produced by the closed-system decay of U, as this would result in highly radiogenic $^{206}Pb/^{204}Pb$ ratios (Nelson *et al*., 1985), as well as high $^{207}Pb/^{204}Pb_{(i)}$ values. This problem can be visualized by comparing the position of the 'HIMU' component with that of the southern and northern Tibetan samples on Fig. 7—whereas the most radiogenic southern samples approach HIMU ratios of $^{207}Pb/^{204}Pb_{(i)}$ and $^{208}Pb/^{204}Pb_{(i)}$, they have relatively low $^{206}Pb/^{204}Pb_{(i)}$ ratios. A single-stage extraction process cannot explain this. If derivation from a depleted mantle reservoir is assumed, the high $^{207}Pb/^{204}Pb_{(i)}$ and relatively low $^{206}Pb/^{204}Pb_{(i)}$ ratios shown by both groups suggests an early increase in μ, followed by a later decrease. U/Pb can be enriched in melts as a consequence of the greater incompatibility of U relative to Pb in melting and crystal fractionation processes. Thus, the U/Pb ratio of a mantle source region could be increased by the introduction of components such as small-degree mantle melts, fluids and/or melts of subducted sediments to the mantle source region. As pointed out by Nelson *et al*. (1985), a multi-stage model (more than two stages of μ change in the source region) is more probable than a two-stage model, because the latter would require an extremely ancient reservoir with correspondingly high μ values (e.g. a 4 Ga source would require a μ value of 10; a slightly younger 3 Ga source would require an even higher μ value of 13) to generate the extremely radiogenic $^{207}Pb/^{204}Pb$ values seen in the Tibetan samples. A multi-stage model would invoke an early reservoir with $\mu = 8{\cdot}0$ at 4·5 Ga, followed by an increase in μ between 4·5 and 2·1 Ga, then a decrease in μ. As recognized by Nelson *et al*. (1985), it is not possible to constrain the values of μ or the magnitude of the different time intervals of closed radiogenic ingrowth of Pb from the Pb isotope compositions of mafic rocks without independent constraints.

In this context, it is interesting to note that the south-west and Pabbai Zong samples have extremely high calculated μ values, ranging from 10·4 to 21·2, and that the Pabbai Zong samples also extend to slightly more radiogenic $^{206}Pb/^{204}Pb$ values compared with the rest of the southern samples (Fig. 7). These high μ values cannot have been a long-term feature of the source region of the south-west and Pabbai Zong samples, as this would give much more radiogenic $^{206}Pb/^{204}Pb$ values than are observed. The μ values of these samples and their $^{206}Pb/^{204}Pb$ compositions can be reconciled by invoking either considerable fractionation of μ in the sample relative to the mantle source during melting or crystal fractionation processes, or else extremely recent metasomatism and an increase in μ, leaving minimal time for ^{206}Pb ingrowth. The south–central and northern samples have more restricted ranges in μ and do not show the trends to higher values of $^{206}Pb/^{204}Pb_{(i)}$ seen in the south-west and Pabbai Zong groups.

$^{207}Pb/^{206}Pb^*$ model ages calculated for individual samples in both groups are 0·82–1·6 Ga for northern samples and 0·79–2·1 Ga for southern samples (Table 4). The sample Pb model ages are consistently older than the samples' respective Nd model ages (Table 3), suggesting that the two isotopic systems are decoupled. Moreover, the samples' $^{207}Pb/^{206}Pb^*$ model ages give exceptionally high Th/U values for their source region (7·8–8·0 for northern Tibet and 7·6–8·3 for southern Tibet; Table 4) which are probably unrealistic.

The model ages are therefore unlikely to be meaningful and cannot be used to place direct constraints on the timing of the melt extraction and metasomatic events affecting the mantle source regions. It is entirely possible that the ancient isotopic signatures of the northern and southern samples reflect the antiquity of the metasomatic components, the initial Nd and Pb isotopic compositions and the budgets of Sm/Nd, U/Pb and Th/Pb of the metasomatic agents and those of the mantle source regions, and the time intervals between episodes of melt extraction, metasomatism and magmatism. None the less, the Nd and Pb model ages do indicate that there is a clear and unambiguous difference between the source regions of samples from northern and southern Tibet, which is in agreement with the constraints from major elements discussed earlier.

Trace element modelling

Rare earth elements: forward modelling and limitations

On the plots of La/Yb vs La and Dy/Yb vs La/Yb (Fig. 11a and b), both northern and southern groups form positive arrays and have elevated Dy/Yb and La/Yb relative to primitive mantle. The southern magmas have lower abundances of La and a wider range of Dy/Yb at more restricted La/Yb compared with the north. As the trace element data have been corrected to 6 wt %

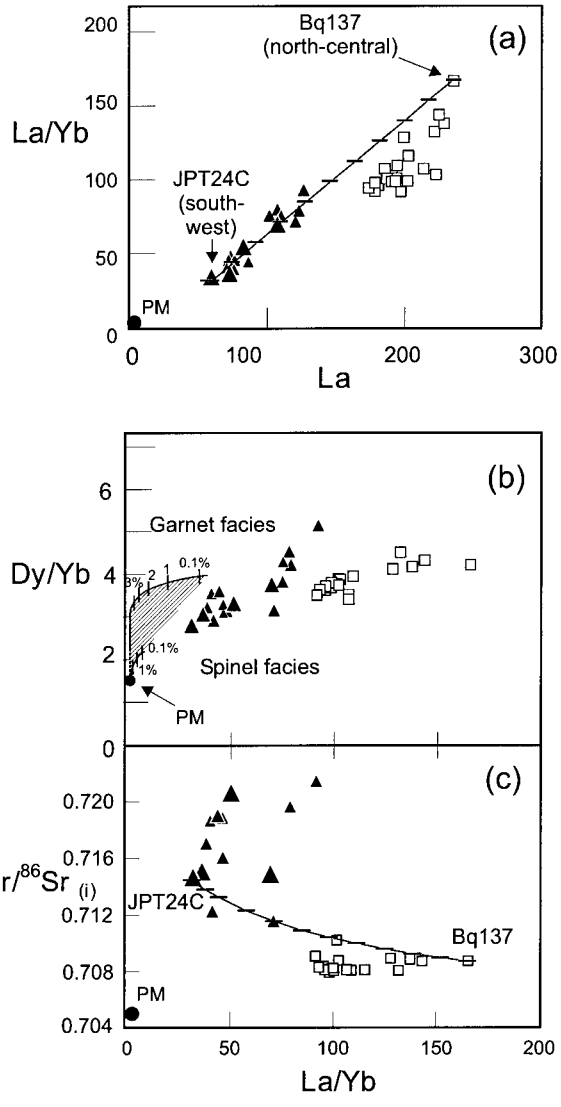

Fig. 11. (a) La/Yb vs La. The concentrations of La and Yb have been corrected to 6 wt % MgO to correct for the majority of AFC effects (the slopes, intercepts and r^2 values for all the regressions against MgO are tabulated in the Appendix). Symbols and data sources as in Fig. 9. PM, Primitive mantle (Sun & McDonough, 1989). The possibility that the near-linear trends defined by the north and south Tibetan rocks are produced by mixing of end-members from the two different sample groups is investigated with a simple binary mixing calculation using the northern sample with the highest La/Yb and La contents (Bq137, 235·6 ppm La; La/Yb 166, La and Yb normalized to MgO = 6 wt %) and the southern sample with the lowest La and La/Yb (JPT24C, 58·2 ppm La, La/Yb 31·2). The tick marks on the mixing curve are mixing proportions of 0·1 (10%). (b) Dy/Yb vs La/Yb (normalized to 6 wt % MgO). Non-modal factional melting curves with 1% residual melt (see caption to Fig. 8) of a peridotite source with a primitive mantle composition (PM; Sun & McDonough, 1989) are shown for comparison. The modal abundances and melt modes (given in parentheses) explored were: *garnet facies*: olivine 0·66 (0·2), orthopyroxene 0·21 (0·3), clinopyroxene 0·07 (0·38), garnet 0·05 (0·1), residual melt 0·01 (0·01); *spinel facies*: olivine 0·69 (0·2), orthopyroxene 0·21 (0·3), clinopyroxene 0·07 (0·38), spinel 0·02 (0·1), residual melt 0·01 (0·01). Partition coefficients are as in Fig. 10. It can be seen that the clinopyroxene modes are much smaller than the melt models for Fig. 10, and almost reach harzburgite levels. This is a deliberate modification that takes into account the constraints obtained from comparing the $CaO_{(6)}$ contents of the southern and northern samples with those of liquids derived by partial melting of peridotite starting minerals with 15 modal % clinopyroxene (see Fig. 9c). (c) Variation of $^{87}Sr/^{86}Sr_{(i)}$ vs La/Yb (corrected to 6 wt % MgO). A binary mixing curve is shown; the end-members are as in (a), their Sr concentrations and $^{87}Sr/^{86}Sr_{(i)}$ signatures are: Bq137, 1722 ppm Sr, $^{87}Sr/^{86}Sr_{(i)}$, 0·708745; JPT24C, 721 ppm Sr, $^{87}Sr/^{86}Sr_{(i)}$, 0·714451. As in (a), ticks show mixing proportion increments of 0·1. The binary mixing curve between JPT24C and Bq137 does not intersect the majority of the southern samples. This rules out a role for mixing between northern and southern Tibetan magmas in the generation of their geochemical signatures; it also emphasizes that the differences between the two groups are real—although their Sr isotope systematics appear to grade into each other at $^{87}Sr/^{86}Sr_{(i)}$ values of 0·710, they do not lie close to a mixing line between the two groups.

MgO, the arrays in Fig. 11a and b are unlikely to be the result of AFC processes or crystal accumulation. However, the correction to 6 wt % MgO does not remove variations in incompatible elements during melting, because of the large contrast in partition coefficients between the elements of interest and MgO. In Fig. 11a, both northern and southern groups form steep arrays, which could be caused by small degrees of partial melting. The arrays are inconsistent with crystal fractionation, which would produce a horizontal trend. On this diagram, it can be seen that the binary mixing line between a northern and a southern sample (see figure caption for details of the mixing calculations) almost matches the arrays defined by the northern and southern samples. However, in Fig. 11c [La/Yb vs $^{87}Sr/^{86}Sr_{(i)}$] it can be seen that a binary mixing curve, which uses the same end-members as in Fig. 11a, does not pass through the majority of sample compositions.

The data arrays in Fig. 11b roughly follow the shapes of melting curves calculated from anhydrous spinel and garnet peridotite sources with primitive mantle La, Dy and Yb concentrations using a model of non-modal fractionation melting where 1% of melt remains in full equilibrium with the source (see caption to Fig. 8 for explanation of the residual melt model; the details of the La/Yb and Dy/Yb ratios are given in the caption to Fig. 11). This indicates that melting processes exert the dominant control on the variations of La/Yb against Dy/Yb in the northern and southern groups. However, comparison of the sample data with these melting models demonstrates that the compositions of the northern and southern magmas cannot be reproduced by melting anhydrous peridotite sources with primitive mantle compositions, in either spinel or garnet facies, and that source(s) with higher La/Yb and Dy/Yb relative to primitive mantle are required. The separation of the northern and southern groups in La/Yb–Dy/Yb space is of a far greater magnitude than can be achieved by partial melting processes, as shown by comparison with the melting curves, which define the maximum range in Dy/Yb and La/Yb that can be achieved by melting a primitive mantle source. Thus, the southern and northern sample groups are likely to have been derived by partial melting of two distinct source regions, with contrasting La/Yb and Dy/Yb compositions that are elevated with respect to primitive mantle. This inference is in agreement with the Sr, Nd and Pb isotope compositions of the sample groups and the major element data. The absence of correlations between La/Yb and $^{87}Sr/^{86}Sr_{(i)}$ implies that melting processes (i.e. the degrees of melting and the source mineralogy), as opposed to source compositional heterogeneity, exert the dominant control on trace element variations within groups, whereas the compositional differences between the two groups are reflection of the composition and mineralogy of their respective source regions.

Inverse modelling

Methods of inverting trace element data for volcanic rocks, with the aim of reconstructing melting regimes, source mineralogy and composition, have been extensively discussed in the literature (Minster & Allègre, 1978; Albarède, 1983; Hofmann & Feigenson, 1983; McKenzie & O'Nions, 1991). Here we use a modified version of the approach adopted by Class & Goldstein (1997), employing the variations of trace elements against an index element in calculating relative *D* values. This approach is based on the assumption that the northern and southern shoshonite groups can be treated as two separate magma series, derived from two distinct mantle source regions. This is supported by the separation of the northern and southern groups on the $MgO_{(6)}$ corrected major element data plots (Fig. 9a–d), the lack of evidence for binary mixing within and between the sample groups (Fig. 8b and 11c, respectively) and the absence of correlations between fractionation-corrected incompatible element ratios and isotopic signatures (Fig. 11c).

Although the absolute degree of melting is not known, the relative degree of melting may be estimated based on the concentration of a highly incompatible index element, whose abundance is inferred to be inversely proportional to the degree of melting. The variation of the elements of interest relative to this index element will be a function of their bulk *D* values relative to the index element and the range in degree of melting, and will be independent of the source composition, provided the assumption is valid that the samples within the dataset are all derived from the same source. This assumption requires justification, as the northern and southern sample suites were emplaced hundreds of kilometres apart over long time intervals (10 Myr in the case of south-west and Pabbai Zong samples, which comprise the southern group; 18 Myr for the north–central and north-west samples, which together form the northern group). However, the southern and northern sample suites are distinct from each other in terms of their major and trace element systematics (Figs 4a–h, 9a–d, 11a and b) and show distinct isotopic signatures (Figs 6a, 7b and d, 10b and 11c) which can best be explained by derivation from two peridotite source regions located within the subcontinental lithosphere. For the most part, the differences between the isotopic and elemental signatures of the southern and northern groups considerably exceed the variations in these parameters within the two groups, justifying the assumption of separate source regions. The exception to this is the variation

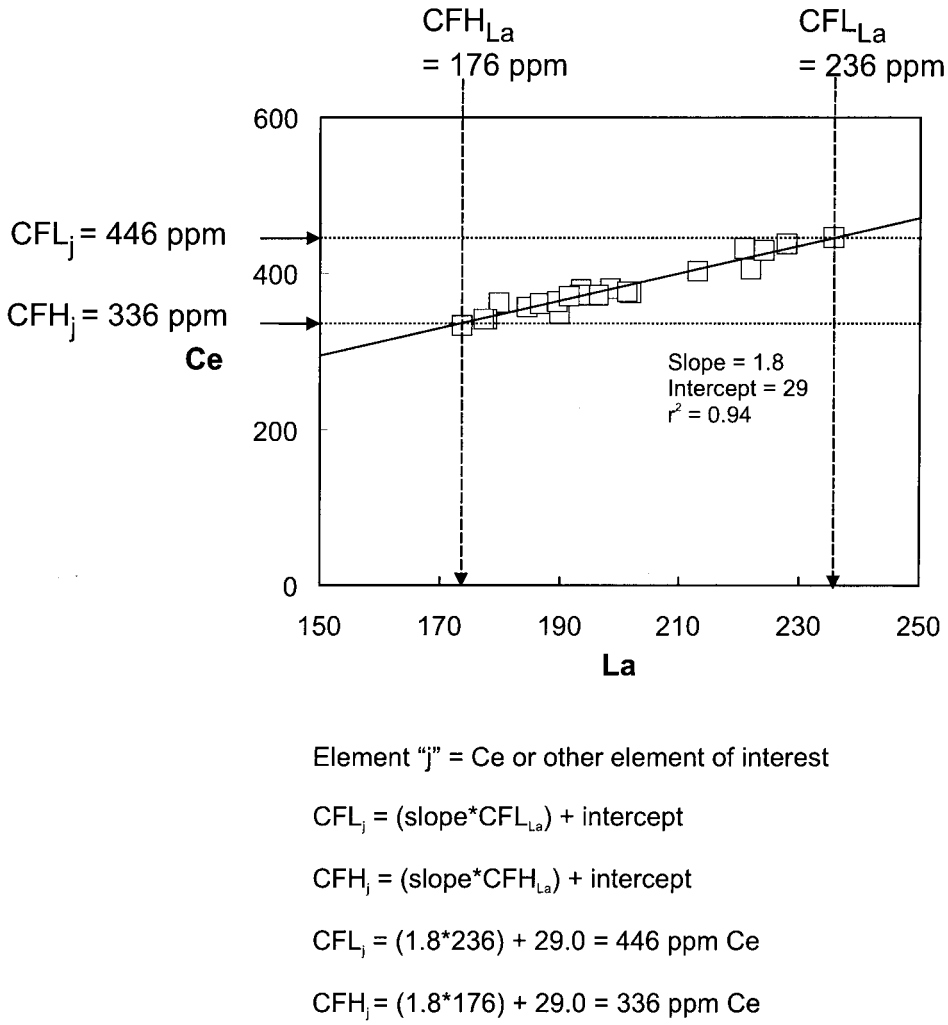

Fig. 12. Graphical illustration of the regression procedure used to calculate CFL_j and CFH_j, where j denotes the element of interest (corrected to 6 wt % MgO), which in this case is Ce, and CFL and CFH stand for the concentration of that element at low and high degrees of melting, respectively. For each sample series (the northern series is illustrated here, but the same calculations apply to the southern series) the highest and lowest values of La (corrected to 6 wt % MgO) define the limits of the lowest (FL) and highest (FH) degrees of melting that characterize the particular sample suite. Thus $CFL_{La} = 236$ ppm (sample Bq137) and $CFH_{La} = 174$ ppm (sample K9024) for the northern sample series (shown in the figure); for the southern series $CFL_{La} = 126$ ppm (sample TE011/93; Miller *et al.*, 1999) and $CFH_{La} = 58$ ppm (sample JPT24C). The values of Ce (i.e. CFL_j and CFH_j; j is Ce) that correspond to these contents of La are calculated using the slope and intercept of the regression line in combination with the values of CFL_{La} and CFH_{La}, as shown in the figure. This calculation procedure was used for all elements for both the northern and southern sample series.

seen in the $^{87}Sr/^{86}Sr_{(i)}$ compositions of the samples in the southern group. However, large variations in $^{87}Sr/^{86}Sr_{(i)}$ can be easily created by variable Rb/Sr ratios in the source region. This could simply reflect slight variations in the modes of the K-bearing phases phlogopite and/or pargasitic amphibole in the source region, as these phases have the potential to fractionate Rb from Sr because of their contrasting mineral–melt partition coefficients for these elements (pargasitic amphibole: $D_{Rb} = 0{\cdot}22$, $D_{Sr} = 0{\cdot}376$; Dalpe & Baker, 1994); phlogopite D_{Rb} 4·75, D_{Sr} 0·0879; Gregoire *et al.*, 2000).

In cogenetic mafic rock suites, the most incompatible elements form linear trends when plotted against a more incompatible index element (see Figs 12 and 13), and the variation of that element relative to the index element provides some measure of the relative value of the bulk D value for the element of interest relative to the index element (Class & Goldstein, 1997). The caveat to this is that the proportions of minerals entering the melt phase should not change dramatically over a range in degrees of melting. For the small degrees of melting typically invoked to explain the petrogenesis of potassic lavas, this assumption is

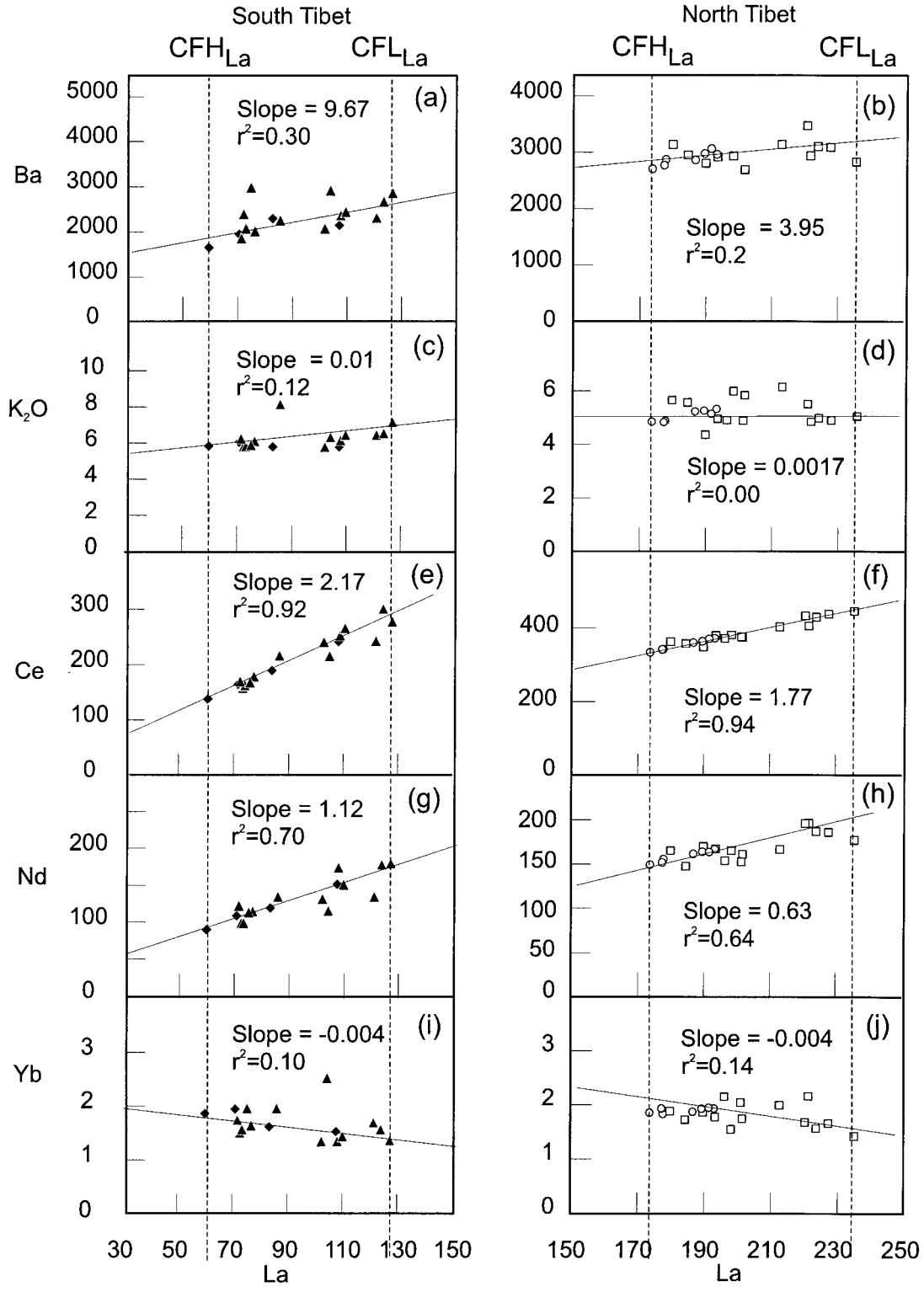

Fig. 13. Plots of the trace elements Ba, K (as K_2O), Ce, Nd and Yb vs La for the southern (a, c, e, g, i) and northern (b, d, f, h, j) sample series used to calculate CFL_j and CFH_j, as discussed in the main text and the caption to Fig. 12. Symbols as in Fig. 9. All data were normalized to MgO = 6 wt %. Units are ppm, with the exception of K_2O, which is given in wt %. The values of CFL_{La} and CFH_{La} for the northern and southern series are as in Fig. 12. The slopes and r^2 values are given for each regression and the tabulated series of regressions against La is given in the Appendix.

reasonable. La is the best available index element for the degree of melting in both northern and southern suites. It has been measured on all samples, behaves incompatibly in both sample suites, and is not easily modified by secondary alteration processes. La was selected over the more incompatible elements for a number of different reasons, given in parentheses: Cs (not measured on all samples and prone to alteration), Rb (compatible in phlogopite), Ba (compatible in pargasitic amphibole), U (easily modified by alteration processes), Th (displayed highly scattered trends), Nb and Ta (negative anomalies on primitive mantle normalized multi-element diagrams) and K (major element in the phlogopite and pargasitic amphibole, buffered with respect to SiO_2 in the northern samples).

Here we employ a modified version of the inverse modelling approach used by Class & Goldstein (1997). We used the minimum and maximum values of La in the northern and southern sample series to define the low and high degrees of melting for the two suites. Thus, CFL_{La} refers to the value of La that we have selected to define the lowest degree of melting (FL), CFH_{La} refers to the value of La that corresponds to the highest degree of melting (FH) characterizing the sample suite. This is illustrated in Fig. 12. It should be emphasized that, at this stage of the calculation, the absolute degrees of melting are unknown and the only constraints are the minimum and maximum values of La in the sample suite. It should be noted that it is now assumed that these values are a function of the degree of melting alone, as the melting assemblage, melt model (e.g. batch vs fractional melting) and partition coefficients remain the same from the lowest (FL) to the highest (FH) degrees of melting.

To describe the behaviour of an element relative to La, its values at the index values of La are calculated by linear regression on a plot of La vs j, where j refers to the element of interest. This is shown in Fig. 12, where the element of interest is Ce. The concentrations of the element j at the index values of La, and thus at the 'low' and 'high' degrees of melting, are expressed as CFL_j and CFH_j, respectively. To express the melting behaviour of any element relative to La the ratio of the element at low degrees of melting to that at high degrees of melting (i.e. CFL_j/CFH_j) is calculated. Following Class & Goldstein (1997) we term this ratio the 'enrichment ratio' (E) as it effectively corresponds to the enrichment of the element of interest in the melt, relative to La. The ratio E is a function of the bulk-rock D value for that element over the range in degrees of melting specified by the maximum and minimum La values of the sample suite. Although it may seem non-intuitive, E for La is not equal to unity, but is equal to CFL_{La}/CFH_{La}. This becomes clear after examination of Fig. 12 and the method of obtaining CFL_j and CFH_j: in a plot of La vs La the slope and intercept will be equal to unity and zero, respectively, so the calculated values of CFL_j and CFH_j will reduce to CFL_{La} and CFH_{La}.

Equation (1) [modified after Class & Goldstein (1997)] is based on the fractional melting equations of Shaw (1970), where FH (highest degree of melting) and FL (lowest degree of melting) substitute for the degree of melting in the original equation, and CFL_j and CFH_j substitute for the concentration of the element in the melt. The starting composition of the source is cancelled out by dividing the expressions for the concentration of an element in the melt at one degree of melting with an expression for the concentration of the element in the melt at a different degree of melting. This is the most important property of these calculations—no assumptions regarding the initial source composition are required. Differences in E values between elements calculated for the sample series therefore relate to differences in bulk D values between two elements; that is, for two elements, j and k, if $E_j < E_k$, then $D_j > D_k$. Examining equation (1), it can be that as D tends toward zero, E will approach FH/FL, i.e. the ratio in the degrees of melting. This ratio effectively defines the melting range and the maximum degree of incompatible element enrichment seen in a sample suite.

This is expressed below, using fractional melting as an example:

$$E = \frac{CFL_j}{CFH_j} = \frac{(1-FL)^{1/D-1}}{(1-FH)^{1/D-1}}. \qquad (1)$$

As D tends towards infinity E will approach (but never reach) unity, even though the more compatible elements may show flat or negative trends against La (Fig. 13d, i and j) and their E ratios, as calculated from the regression slopes, can fall below unity. Thus, E ratios of unity can be obtained for many elements from the actual sample data, but the lowest E ratio that can be modelled is unity. In Fig. 13e and f, Ce is tightly correlated with La in both the northern and southern groups ($r^2 = 0{\cdot}94$ for the north, and 0·92 for the south) as would be expected for elements of similar compatibility.

REE modelling. The enrichment (E) ratios of the REE for the northern and southern suites as calculated by regression of the sample series are shown in Fig. 14 as continuous grey curves. These curves illustrate the calculated enrichment of REE in the melt relative to the index values of La and do not correspond to the expected compositions of any model source. The black curves superimposed on the grey curve are the theoretical E ratios calculated by anhydrous melting of peridotite sources with variable modal mineralogies (spinel and garnet facies, see caption to Fig. 14 for mineral and

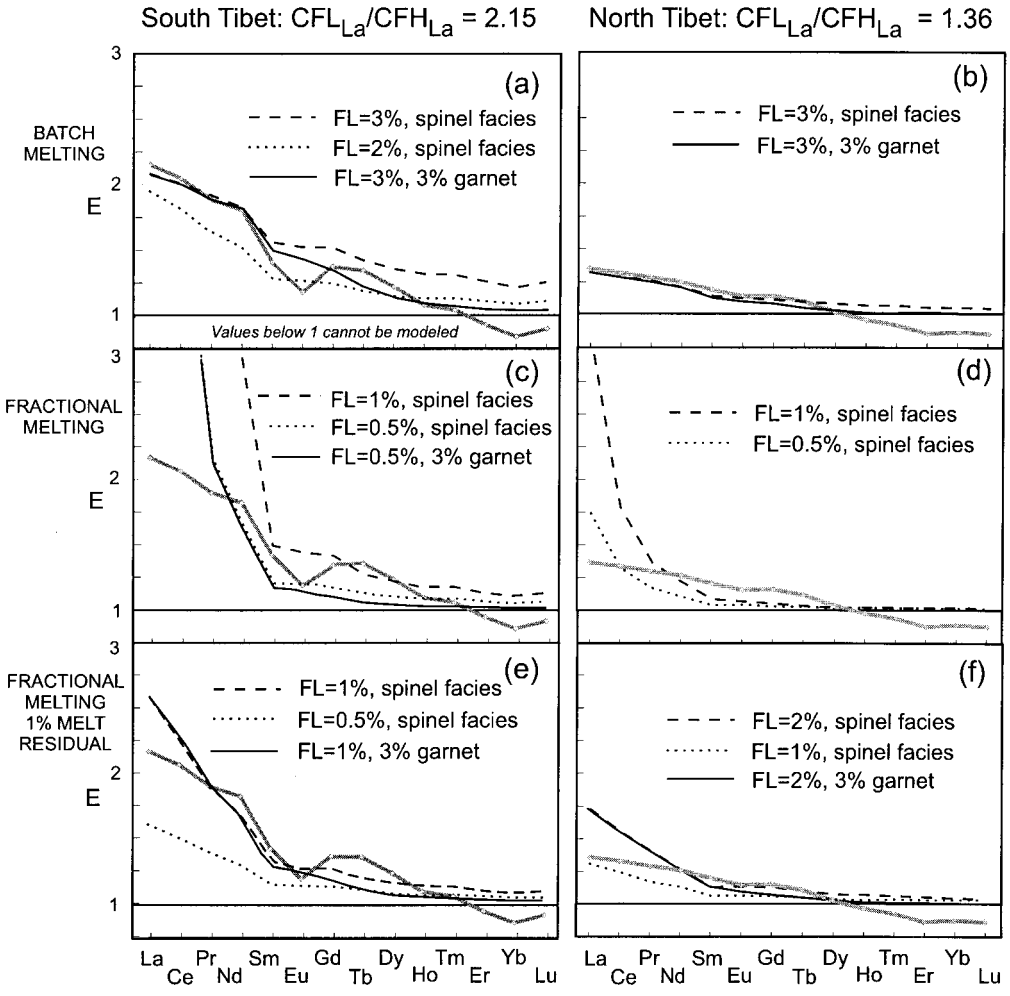

Fig. 14. *E* ratios for the REE calculated for the northern and southern Tibetan series from the actual sample data (normalized to 6 wt % MgO) are shown as continuous grey lines, and are compared with different melting models for phlogopite peridotites (harzburgites, as the clinopyroxene modal abundance is 3%), which are detailed below, and tabulated in the Appendix. The models plotted here are those that gave the closest matches to the *E* ratio curves of northern and southern Tibet, plotting either on, just above or just below the continuous grey curves. Mineral modal abundances (melt modes in parentheses) for non-modal batch and fractional models for southern Tibet without residual melt: *spinel facies*: olivine 0·69 (0·18), orthopyroxene 0·10 (0·19), clinopyroxene 0·03 (0·27), phlogopite 0·17 (0·35), spinel 0·01 (0·01); *garnet facies*: olivine 0·69 (0·15), orthopyroxene 0·10 (0·17), clinopyroxene 0·03 (0·27), phlogopite 0·14 (0·35), spinel 0·01 (0·01), garnet 0·03 (0·05); Non-modal fractional melting with 1% residual melt for southern Tibet: *spinel facies*: olivine 0·68 (0·18), orthopyroxene 0·10 (0·18), clinopyroxene 0·03 (0·27), phlogopite 0·17 (0·35), spinel 0·01 (0·01), residual melt 0·01 (0·01); *garnet facies*: olivine 0·68 (0·14), orthopyroxene 0·10 (0·17), clinopyroxene 0·03 (0·27), phlogopite 0·14 (0·35), spinel 0·01 (0·01), garnet 0·03 (0·05), residual melt 0·01 (0·01). Non-modal batch and fractional models for northern Tibet without residual melt: *spinel facies*: olivine 0·69 (0·18), orthopyroxene 0·10 (0·19), clinopyroxene 0·05 (0·27), phlogopite 0·15 (0·35), spinel 0·01 (0·01); *garnet facies*: olivine 0·69 (0·15), orthopyroxene 0·10 (0·17), clinopyroxene 0·05 (0·27), phlogopite 0·12 (0·35), spinel 0·01 (0·01), garnet 0·03 (0·05). Non-modal fractional melting with 1% residual melt for northern Tibet: *spinel facies*: olivine 0·68 (0·17), orthopyroxene 0·10 (0·18), clinopyroxene 0·05 (0·27), phlogopite 0·15 (0·35), spinel 0·01 (0·01), residual melt 0·01 (0·01); *garnet facies*: olivine 0·68 (0·13), orthopyroxene 0·10 (0·17), clinopyroxene 0·03 (0·27), phlogopite 0·12 (0·35), spinel 0·01 (0·01), garnet 0·03 (0·05), residual melt 0·01 (0·01). Partition coefficients and their sources are tabulated in the Appendix.

melt modes; partition coefficients are given in the Appendix) using models of non-modal batch melting, non-modal fractional melting, and non-modal fractional melting with 1% of residual melt present. The inputs into the melting equations are the lowest degree of melting (FL) the range in degrees of melting [FH/FL, which is calculated from the sample data as CFL_{La}/CFH_{La}, because we assume that La in the most incompatible element and because equation (1) states that as D tends towards zero, CFL_j/CFH_j tends towards FH/FL], which then allows FH to be calculated in the model, the mineral assemblages, melt modes and partition coefficients. The mineral assemblages and melt modes for the models in this paper are given in the captions to Figs 13 and 14, and the partition coefficients are given in the Appendix.

The E ratios were calculated using equation (1) for both the fractional melting models; the batch melting calculations are similar, and involve the same substitutions into the batch melting equation of Shaw (1970). The E ratio for La was also calculated, both from the sample data by regression (grey curve) and in the models (black curves). It should be noted that, as discussed above, there is no requirement for the E ratio of La to be equal to unity. This is important, as the difference between the E ratio of a given element and that for La is a measure of that element's bulk D value relative to La. For example, E_{La} in the northern group is 1·36, and E_{Ce} in the northern group is 1·33, indicating that the bulk D value for Ce is marginally higher than that of La.

In Fig. 14, the E ratios calculated from the regressions (i.e. the actual data, grey curve) for the southern group form a steep slope from the LREE to the HREE, with a slight Eu anomaly. In contrast, the northern trace shows much less fractionation between the LREE and the MREE or HREE. These contrasts suggest different melt regimes, i.e. source mineralogy, degrees of melting and depth, but not source composition, as equation (1) shows that the initial composition of the source is not a required input for calculating E. The curves of E ratios calculated from real data are compared with partial melting models in Fig. 14. We can thus quantify the two most important parameters for determining the enrichment of the REE in mantle melts: the degree of melting (specified in Fig. 14 as FL; FH is then calculated by dividing CFL_{La}/CFH_{La} by FL, as $CFL_{La}/CFH_{La} = FL/FH$); and the modal abundance of garnet (or its complete absence) in the source regions for north Tibetan lavas. These are first-order constraints, and are required before progressing to more complex models involving the LILE and HFSE.

To minimize the number of unknown factors in the inverse modelling of the REE, we use phlogopite as the only hydrous K-bearing phase during melting. Although it is possible that the main host of K in the source regions of the Tibetan samples is amphibole rather than phlogopite, the inclusion of one rather that the other does not exert a strong control on the partitioning of the REE during mantle melting, as the D values for the REE in pargasitic amphibole and phlogopite are very small (Dalpe & Baker, 1994; Gregoire *et al.*, 2000). Although phases such as the phosphates (apatite, monazite) and zircon do have high D values for the REE, they are not considered here because we did not observe any correlation between the REE and P_2O_5 or Zr. Ti-bearing phases such as rutile and titanite are not incorporated at this stage because they do not strongly affect the REE melting budget. In Fig. 14, enrichment ratios are compared with non-modal batch (Fig. 14a and b), non-modal fractional (Fig. 14c and d), and non-modal fractional melting models where residual melt remains present (Fig. 14e and f), for both spinel- and garnet-facies phlogopite-bearing peridotites. In the case of non-modal fractional melting with 1% residual melt present (discussed in the caption to Fig. 8), the trapped melt is treated as a phase in equilibrium with the bulk melting assemblage, and is given a partition coefficient of unity and a melting mode of 1% (Pearce & Parkinson, 1993). This increases the bulk D values for all elements, having the greatest effect on the most incompatible elements, and provides an intermediate between pure batch and fractional melting models.

In Fig. 14, the melt models that best fitted the natural data (continuous grey lines) are shown. Modal mineralogies with $>3\%$ garnet were considered, but these depressed the E values of the model curves for the MREE far below the E values calculated for the actual data, and it was not possible to obtain a fit, irrespective of the value of FL used, or whether batch or fractional melting models were used. The model curves for depleted peridotites (harzburgites) with modal mineralogies of 3% clinopyroxene, 68–69% olivine, 10–18% orthopyroxene, 12–17% phlogopite, 1% spinel or 3% garnet (see caption to Fig. 14) gave fits to the MREE and HREE that were most compatible with the sample data, and most consistent with the low $CaO_{(6)}$ values of the samples. In Fig. 14d, no garnet curves are plotted, because these gave extremely large mismatches to the real data, and plotted partially off-scale.

The curves produced by the different melting models for the garnet- and spinel-facies peridotites were compared using different values of FL. We have plotted the curves that best approximate the E values calculated from the real data. In general, it was not possible to achieve a perfect fit, so the curves that best bracketed the real data are shown. For example, a fractional melting model with FL $<0{\cdot}5\%$ would not produce a significant range in incompatible element compositions in the melt, and one with over 1% melting would produce too great a range in concentrations for the elements more incompatible than Ho. This seems counter-intuitive at first because classic melting equations (Shaw, 1970) predict that the highly incompatible elements are most enriched in the smallest degrees of melting. However, E values may in some cases be higher for larger values of FL because E values do not describe the absolute concentrations of incompatible elements in the melt, but rather define the range in the concentrations of an incompatible element in a cogenetic magma suite. The latter may increase or decrease depending on the range in degrees of melting, source mineralogy and partition coefficients. Thus, a greater range in concentrations may be produced by a larger FL, which will in turn generate a larger

FH, and potentially a greater spread in the enrichment of trace elements in the melt, although not necessarily higher absolute concentrations of the element of interest in the melt.

E values for the REE as a whole are higher in the southern group than in the northern group, suggesting a greater range in the degree of melting. In Fig. 14, it can be seen that models of 1–2·15% non-modal fractional melting with residual melt present in the spinel facies are the best approximation to the overall pattern of the enrichment of the REE in the southern Tibetan suite, and lower degrees of melting do not fit the sample data (Fig. 14e). For northern Tibet, models of non-modal batch melting and non-modal fractional melting with 1% residual melt present best fit the relatively flat trend of the enrichment ratios. However, neither of the two pure fractional melting models fitted the northern Tibet data, as they always produced too great a contrast in the *E* values of the LREE (La to Pr) relative to the MREE (Nd to Dy). Melt models with

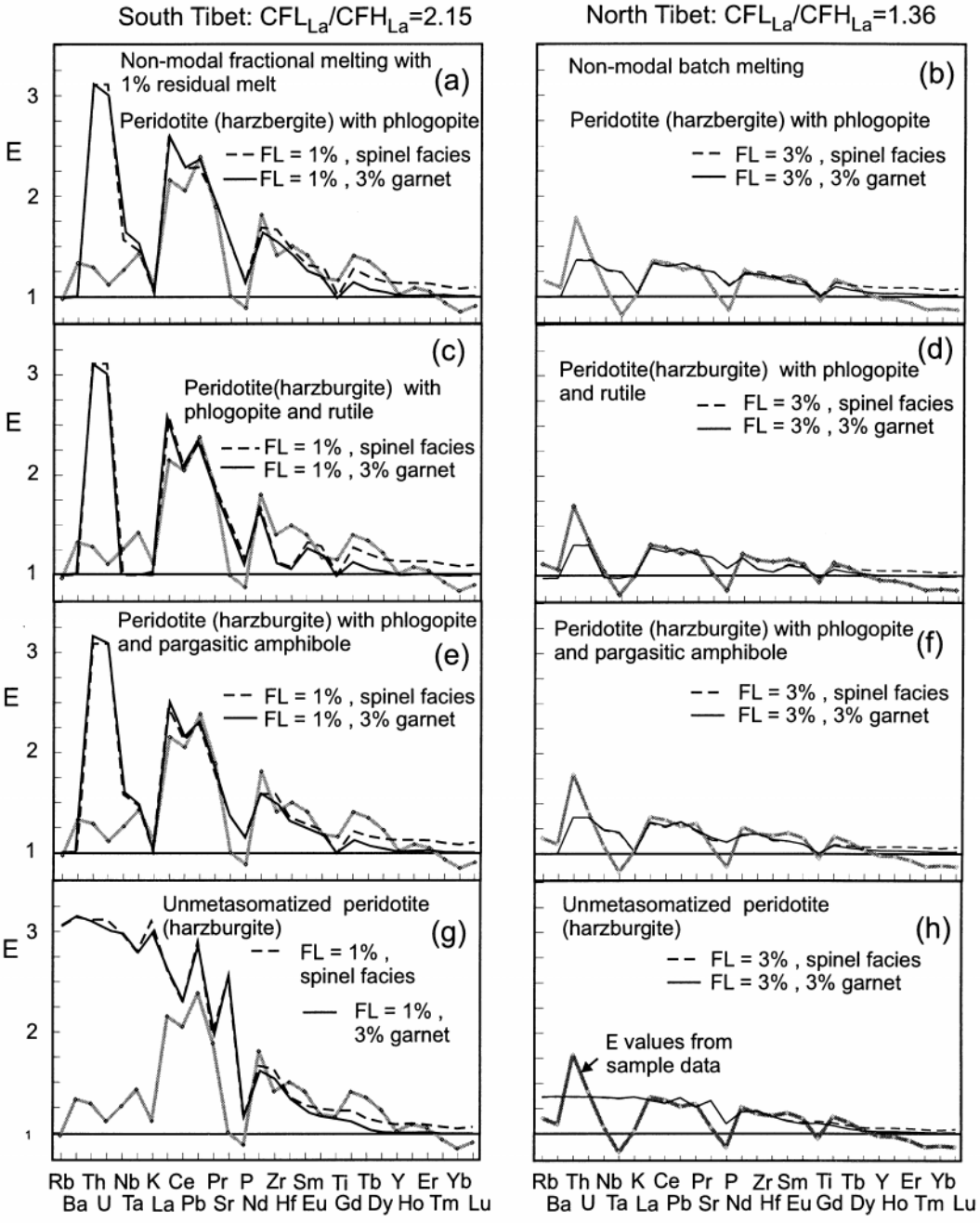

over 3% garnet did not fit the E values of the northern samples. The inverse modelling is limited by the fact that the modelled E values cannot fall below unity, even though the E values calculated directly from the sample data clearly do so.

For both southern and northern Tibet, the partial melting models for the REE do not clearly distinguish whether or not garnet is present in the source region. None the less, models with more than 3% garnet in the source region could not be fitted to the southern Tibet E values. Given that 3% garnet is the maximum permitted by the models, it is likely that melting takes place in the garnet–spinel transition zone in both northern and southern Tibet.

LILE and HFSE modelling. Given the broad constraints obtained on the melting regime and modal mineralogy of the source regions for northern and southern Tibet, the modelling is now expanded to consider the LILE and HFSE, with the aim of determining whether or not residual amphibole is present in addition to/instead of residual phlogopite, and whether or not there are residual Ti-bearing phases present. Rutile was selected as the most probable Ti-bearing phase as it is stable at high temperatures and pressures; titanite is only stable at temperatures up to 750°C at pressures of 0·5 GPa, and at higher pressures (1·2 GPa) it is not stable above 450°C (Frost *et al*., 2001), whereas ilmenite is also unstable at pressures $>0{\cdot}5$ GPa (Frost *et al*., 2001). Enrichment ratios calculated for melts derived from anhydrous peridotite sources should form smooth patterns on multi-element diagrams such as in Fig. 15, in which the sequence of elements, from left to right, reflects increasing element compatibility in an anhydrous spinel or garnet peridotite source. The enrichment ratio pattern of the southern suite shows troughs for U, K, Sr, P, Zr, Eu and Ti relative to the elements on either side of them in the multi-element diagrams in Fig. 15. In contrast, the northern group has negative anomalies for Rb, Ba, Nb, Ta, K, Sr, P, and Ti. The curve of E values derived from real data (continuous grey curve in Fig. 15a–h) for south Tibet is steeper than that for northern Tibet between Ce and Y, showing both higher values and greater variation in enrichment ratios.

Negative anomalies suggest the presence of residual phase(s) other than the 'normal' anhydrous mantle assemblages. As E values are independent of the initial composition of the mantle source [equation (1)], they depend only on the mineralogy, melting regime and mineral–melt partition coefficients and do not reflect the source composition itself. This is in contrast to primitive mantle normalized multi-element diagrams, where negative anomalies can be inherited from the source region and may signify nothing about the source mineral assemblage.

In Fig. 15g and h, it can be seen that the E values of the elements Nb, Ta, Rb, Ba, K and Sr of the anhydrous peridotite model curves are considerably greater than those determined directly from the northern and southern sample data. This indicates that there must be additional residual phases in the source regions of the northern and southern Tibetan samples that retain these elements during partial melting. Such phases include pargasitic amphibole, phlogopite and rutile. In the case of southern Tibet, the spinel-facies harzburgite model with residual pargasitic amphibole and phlogopite is the most appropriate in terms of matching the E values of Rb and the elements lying to the right of Ta on the multi-element E-value diagram, including the MREE from Gd to Dy (Fig. 15e). This

Fig. 15. (opposite) Enrichment ratios for the northern and southern Tibetan series plotted on multi-element diagrams and compared with different peridotite melting models. Non-modal fractional melting with 1% residual melt is used for southern Tibet; a simple non-modal melting model is used for north Tibet as this gave a slightly better fit to the REE data. The modal abundances used take the optimal abundances of olivine, orthopyroxene, clinopyroxene from Fig. 14, and both spinel- and garnet-facies peridotites with phlogopite ± pargasitic amphibole ± rutile are compared. All assemblages for southern Tibet (a, c, e, g) also contain 1% residual melt with a melting mode of 0·01. The mineral assemblages used in the different models are given below, and the melt modes are given in parentheses: (a) *spinel facies*: olivine 0·68 (0·15), orthopyroxene 0·1 (0·18), clinopyroxene 0·03 (0·3), spinel 0·01, phlogopite 0·17 (0·35); *garnet facies*: olivine 0·68 (0·14), orthopyroxene 0·1 (0·17), clinopyroxene 0·03 (0·27), spinel 0·01, phlogopite 0·14 (0·35), garnet 0·03 (0·05). (b) *Spinel facies*: olivine 0·69 (0·18), orthopyroxene 0·1 (0·19), clinopyroxene 0·05 (0·27), spinel 0·01 (0·01), phlogopite 0·15 (0·35); *garnet facies*: olivine 0·69 (0·15), orthopyroxene 0·1 (0·17), clinopyroxene 0·05 (0·27), spinel 0·01 (0·01), phlogopite 0·12 (0·35), garnet 0·03 (0·05). (c) *Spinel facies*: olivine 0·69 (0·15), orthopyroxene 0·1 (0·18), clinopyroxene 0·03 (0·3), spinel 0·01 (0·01), phlogopite 0·15 (0·33), rutile 0·02 (0·02); *garnet facies*: olivine 0·65 (0·13), orthopyroxene 0·1 (0·18), clinopyroxene 0·03 (0·27), spinel 0·01 (0·01), phlogopite 0·15 (0·33), garnet 0·03 (0·05), rutile 0·02 (0·02). (d) *Spinel facies:* olivine 0·67 (0·18), orthopyroxene 0·1 (0·16), clinopyroxene 0·05 (0·3), spinel 0·01 (0·01), phlogopite 0·15 (0·33), rutile 0·02 (0·02); *garnet facies*: olivine 0·64 (0·16), orthopyroxene 0·1 (0·16), clinopyroxene 0·05 (0·27), spinel 0·01 (0·01), phlogopite 0·15 (0·33), garnet 0·03 (0·05), rutile 0·02 (0·02). (e) *Spinel facies*: olivine 0·68 (0·1), orthopyroxene 0·1 (0·1), clinopyroxene 0·03 (0·2), spinel 0·01 (0·01), phlogopite 0·15 (0·28), pargasitic amphibole 0·02 (0·3); *garnet facies*: olivine 0·65 (0·1), orthopyroxene 0·1 (0·1), clinopyroxene 0·05 (0·2), spinel 0·01 (0·01), phlogopite 0·15 (0·33), garnet 0·03 (0·05), pargasitic amphibole 0·02 (0·25). (f) *Spinel facies*: olivine 0·67 (0·1), orthopyroxene 0·1 (0·1), clinopyroxene 0·05 (0·2), spinel 0·01 (0·01), phlogopite 0·15 (0·29), pargasitic amphibole 0·02 (0·3); *garnet facies*: olivine 0·64 (0·1), orthopyroxene 0·1 (0·1), clinopyroxene 0·05 (0·2), spinel 0·01 (0·01), phlogopite 0·15 (0·29), garnet 0·03 (0·05), pargasitic amphibole 0·02 (0·25). (g) *Spinel facies*: olivine 0·75 (0·24), orthopyroxene 0·2 (0·24), clinopyroxene 0·03 (0·5), spinel 0·01 (0·01); *garnet facies*: olivine 0·75 (0·21), orthopyroxene 0·17 (0·22), clinopyroxene 0·03 (0·5), spinel 0·01 (0·01), garnet 0·03 (0·05). (h) *Spinel facies*: olivine 0·74 (0·24), orthopyroxene 0·2 (0·25), clinopyroxene 0·05 (0·5), spinel 0·01 (0·01); *garnet facies*: olivine 0·74 (0·22), orthopyroxene 0·17 (0·22), clinopyroxene 0·03 (0·5), spinel 0·01 (0·01), garnet 0·03 (0·05). Partition coefficients are given in the Appendix.

model (and the other models for southern Tibet with different source mineralogies) does not match the E values of Ba (e.g. this model gives an E value of unity, the value from the real data is 1·33), or Th, U and Nb. However, residual phlogopite alone (Fig. 15a) does not explain the behaviour of Sr, La and Ce as well as the model with residual amphibole and phlogopite. Moreover, incorporating residual rutile (Fig. 15c) does not allow for the enrichment of Zr and Hf in the melt, as well as giving much lower E values for Nb and Ta than have been calculated from the real data. The more compatible behaviour of Th and U with respect to Ce and that of Zr with respect to Nd and Hf in the southern group may reflect the presence of residual zircon. This is not incorporated in the trace-element modelling because of the large uncertainties for the appropriate D values for Th, U and Pb between zircon and melt in mafic systems.

For northern Tibet a model of non-modal batch melting is used, as this gave a slightly better fit to the data than the non-modal fractional model with 1% residual melt in Fig. 14. The E values determined by the linear regression of the northern Tibet samples lie between the melt model for a phlogopite harzburgite source with 3% garnet and the melt model curve for a spinel facies phlogopite harzburgite. The spinel facies model fits the E values of Gd and Tb better than the garnet-facies model, although it overestimates the E values of Dy slightly. None of the garnet or spinel-facies models can reproduce the E values (as calculated from sample data) to the right of Y on the multi-element diagrams in Fig. 15. This is a consequence of the partial melting equations used [see equation (1)], which do not permit E to fall below unity. Despite this limitation, we consider that the spinel-facies phlogopite peridotite model fits the E values of the northern Tibet samples the best. Therefore, we conclude that melting took place dominantly in the spinel facies for northern Tibet. However, Cooper *et al.* (2002) measured significant excesses of ^{230}Th relative to ^{238}U in Quaternary mafic lavas from the Ashikule region (Fig. 1) of northern Tibet, which they interpreted in terms of melting in the presence of significant amounts of residual garnet (7·5 modal % of a phlogopite peridotite). These results are somewhat difficult to reconcile with the conclusions drawn above. One possibility, recognized by Cooper *et al.* (2002), is that melting takes place in the garnet-bearing lithologies in the lower crust. Another explanation is that the Ashikule lavas measured by Cooper *et al.* are anomalous with respect to the older samples studied here, and possibly result from an entirely different geodynamic process. It should be emphasized that the conclusions drawn on the basis of the inverse trace element modelling are of a very broad nature as the southern and northern Tibetan samples have been treated as two time-averaged and spatially averaged cogenetic lava suites.

None of the melt models for northern Tibet explored above successfully explain the significant negative Nb and Ta anomalies seen in the E value curves derived from the real sample data for both northern and southern Tibet. Although partitioning data for amphibole and mica (Adam *et al.*, 1993; Dalpe & Baker, 1994; LaTourette *et al.*, 1995; Foley *et al.*, 1996; Schmidt *et al.*, 1999) suggest low D_{Nb} and D_{Ta} values, high concentrations of Nb and Ta have been observed in amphibole and phlogopite within metasomatic veins (Ionov & Hofmann, 1995). On this basis, Ionov & Hofmann (1995) suggested that these phases could be important reservoirs for Nb and Ta within the SCLM, and that the currently available partition coefficients for these phases could be underestimates. This would account for the discrepancy between the models and the enrichment ratio traces for southern and northern Tibet.

DISCUSSION

SCLM composition and evolution

The contrasting major element compositions and Sr–Nd–Pb isotope systematics of the southern and northern shoshonites can be related to derivation from the separate, tectonically juxtaposed lithospheric terranes which comprise the Tibetan plateau (Fig. 1). One option is that the southern SCLM corresponds to the Lhasa Terrane, the northern to the Songpan–Ganze and Kunlun terranes. However, there are not enough primitive samples from northern Tibet to model and thus attempt to distinguish between the geochemical signatures of these two terranes. None the less, the normalized [to $MgO_{(6)}$] major element data, which suggest that the southern samples were derived from a source with lower $Fe_2O_{3(6)}$ compared with the northern samples, are consistent with recent seismic tomography data. The latter indicate that the lithospheric mantle of southern Tibet is less dense, and hence lower in Fe and more refractory than that of northern Tibet (Kosarev *et al.*, 1999).

The constraints on melt fraction and source modal mineralogy obtained in the previous section can be used in combination with the compositions of the northern and southern magmas to estimate their source region compositions, using the lowest melt fraction (FL), the trace element compositions of the two samples with the highest La concentrations that were initially used to define the values of FL for the northern and southern series (north: sample Bq137, 236 ppm; south: sample TE011/93, 126 ppm; Miller *et al.*, 1999), and the modal mineralogies determined from the inverse

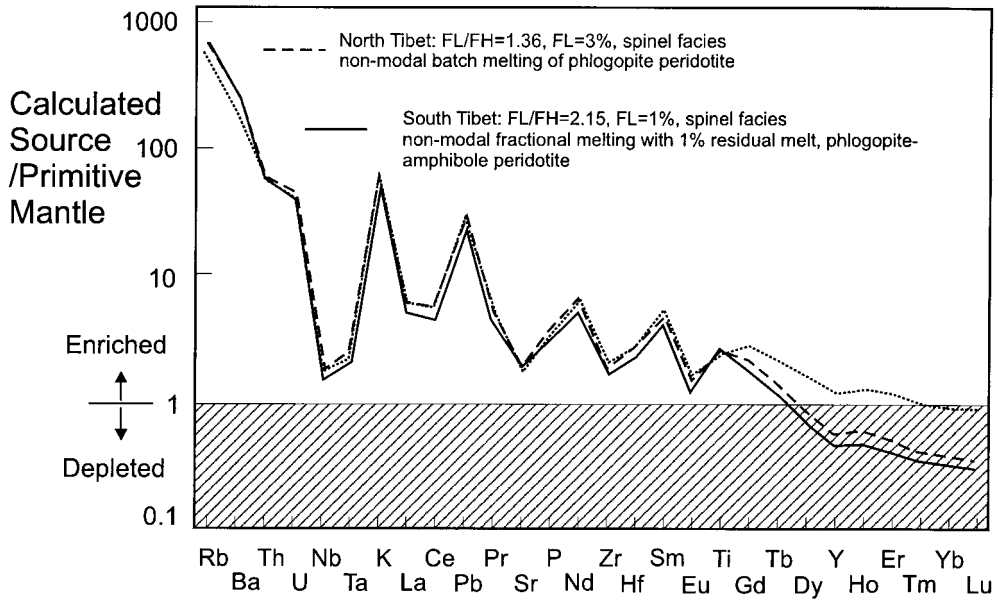

Fig. 16. Calculated mantle source compositions for the northern and southern samples, normalized to primitive mantle (Sun & McDonough, 1989). The source compositions were calculated using the melt models, source mineralogies and values of FL in Fig. 15. For northern Tibet, this amounts to FL = 3%, non-modal batch melting (melt modes in parentheses) of a spinel-facies phlogopite peridotite: olivine 0·69 (0·17), orthopyroxene 0·10 (0·19), clinopyroxene 0·05 (0·27), phlogopite 0·15 (0·35), spinel 0·01 (0·01). For southern Tibet, a model of non-modal (melt modes in parentheses) fractional melting with 1% residual melt of a spinel facies phlogopite–amphibole peridotite was used: olivine 0·68 (0·1), orthopyroxene 0·10 (0·1), clinopyroxene 0·03 (0·2), phlogopite 0·15 (0·28), pargasitic amphibole 0·02 (0·3), spinel 0·01 (0·01), residual melt 0·01 (0·01). FL was 1%, as in Fig. 15. The trace element compositions (normalized to 6 wt % MgO) of the samples Bq137 and TE011/93 were used as the lowest-degree melts of the northern and southern mantle sources, respectively, and the source compositions were calculated from these 'melt compositions'; the values of FL and the mineralogies melting modes given above. The partition coefficients are the same as in Figs 14 and 15, and are given in the Appendix.

modelling (a phlogopite spinel peridotite for northern Tibet, and a phlogopite–amphibole spinel peridotite for southern Tibet). Comparison of the source compositions presented on primitive mantle (PM) normalized multi-element diagrams (Fig. 16) indicates that the source regions are extremely similar in terms of their incompatible element signatures; both are considerably enriched in the LILE and LREE–MREE relative to PM (Sun & McDonough, 1989) and for the spinel-facies models, both sources show similar depletions in the HREE. Mass balance calculations for the partial melting of a mantle reservoir with a PM composition (Sun & McDonough, 1989) can be used to place constraints on the amount of melt extraction that must have taken place prior to metasomatism. A model of non-modal batch partial melting with a modal mineralogy (melt modes in parentheses) of: olivine 0·67 (0·2); orthopyroxene 0·15 (0·2); clinopyroxene 0·17 (0·48); spinel 0·01 (0·12) was used to calculate the degree of melt extraction required to generate the low HREE contents of the northern and southern SCLM. This model demonstrates that ~30% melt extraction is required to explain the low HREE contents of the southern Tibet and spinel-facies northern Tibet sources, although it assumes a single-stage melt extraction process, and does not allow for any later enrichment of the HREE during metasomatic processes. None the less, it is consistent with the high Cr contents of the southern Tibetan samples, which require a source higher in Cr than the primitive mantle (see caption and discussion of Fig. 8).

The refractory nature and the large degrees of melt extraction inferred for the northern and southern Tibetan SCLM source regions from this model are in agreement with models of SCLM formation by melt extraction from the convecting mantle and segregation of the buoyant residua (Jordan, 1978; Pollack, 1986). Although there are no constraints on the timing of stabilization of these source regions, the isotope data data clearly indicate that they have contrasting time-integrated histories. This is rather paradoxical considering the strong similarities between the calculated incompatible element conncentrations of the two source regions. The calculated incompatible element compositions of the southern and northern shoshonite both give a classical 'subduction signature' of negative Nb–Ta, and Zr coupled to LREE/HREE enrichment (Gill, 1981). This suggests metasomatism by silicate melts or fluids derived from subducted sediments. The similarities in the incompatible element

compositions of the source regions could be reconciled with their contrasting major element and isotopic signatures if metasomatism resulted from similar processes but took place at different times. An equally plausible alternative is that the source regions were enriched by metasomatic components with different ages (and hence isotopic compositions) but with similar incompatible element signatures.

The origin of HFSE depletions relative to the REE and LILE in island-arc volcanics and in continental potassic magmas has attracted considerable attention. Because of their high D values for the HFSE, Ti-bearing phases, particularly rutile, have been assigned a major role in the generation of HFSE anomalies (e.g. Foley & Wheller, 1990; Green, 1995). Despite their negative Nb–Ta anomalies (Fig. 16), the Tibetan mantle sources are enriched in Nb and Ta relative to primitive mantle. Mechanisms for HFSE transport and addition to the SCLM include release of aqueous fluids following slab dehydration (Brenan *et al*., 1994), metasomatism by carbonatite melts (Yaxley *et al*., 1991), and hybridization of the mantle wedge by silicic melts derived from subducted altered oceanic crust or pelagic or terrigenous sediments. As experimental studies (Brenan *et al*., 1994) indicate that the concentrations of Nb and Ta in an aqueous fluid in equilibrium with rutile are negligible, it is unlikely that the HFSE signature results from slab-derived fluids. However, Ta and Nb partition more readily into silicate melts (Green & Pearson, 1986; Green, 1995), and silicic melts of either altered oceanic crust or sedimentary material are a plausible source for the HFSE enrichment. Residual Ti-bearing phases or residual amphibole in the slab give a metasomatic component with a HFSE-depleted signature, even though the absolute abundances of these elements in the SCLM are increased with respect to primitive mantle as a consequence of metasomatism.

Metasomatism by silicate melts is also a plausible explanation for the negative Eu anomalies (with respect to Sm and Gd) in both northern and southern Tibet, indicating generation of the metasomatizing melts in the presence of residual plagioclase. Indeed, Turner *et al*. (1996) suggested that ancient subduction processes were responsible for the metasomatism of the north Tibetan SCLM, and that melts and fluids derived from subducted sediments were the most likely metasomatic agents. Similarly, Miller *et al*. (1999) and Maheo *et al*. (2002) both invoked pelagic sediment components in the source of the southern Tibetan volcanics, and it is probable that several different metasomatic components were involved in the enrichment of both source regions. Maheo *et al*. (2002) suggested, on the basis of Sr–Nd isotopic data for Neogene magmatic rocks in the south Karakorum, that the southern Tibet SCLM had been contaminated by Precambrian crust and used this information to infer than the southern Tibet SCLM had been metasomatized by melts derived from subducted Indian continental material. However, the lack of a direct proxy for this material makes this hypothesis difficult to test. In any case, the sediment components responsible for metasomatism must have had an average isotopic composition considerably different from that of globally subducted average sediment (Plank & Langmuir, 1998), as no clear mixing trends with GLOSS and the Tibetan samples or any other mantle end-members are apparent in Fig. 7.

Discussion in the context of recent geodynamic models

As has been discussed in the previous sections, the samples from the Pabbai Zong and south-west groups in southern Tibet, and from the north-west and north–central groups in northern Tibet were derived by small degrees of melting of metasomatized, depleted peridotite source regions within the SCLM. Residual garnet is not required to generate the trace element compositions of the southern and northern Tibetan samples and the pressures of melt generation are thus constrained to be in the region of the garnet–spinel transition (around 1·8 GPa, Wallace & Green, 1991; Robinson & Wood, 1998; Klemme & O'Neill, 2000). The differences in the melting models (north Tibet, 3–4% partial non-modal batch melting of a phlogopite- and spinel-bearing harzburgite; south Tibet, 1–2% partial non-modal fractional melting with 1% residual melt present of a phlogopite-, pargasitic amphibole- and spinel-bearing harzburgite) invoked for the northern and southern suites are barely resolvable, but, if real, they could reflect the mineralogy and fertility of the source region. Alternatively, they could be a consequence of different geodynamic processes operating in the northern and southern regions of the Tibetan plateau. Although not included in the inverse modelling datasets, the south-east, south–central and north–central samples also exhibit shallow slopes from Gd to Lu on primitive mantle normalized diagrams (Fig. 5a and b), which precludes a significant role for residual garnet in their petrogenesis and implies depths of melting at least as shallow as the more mafic samples.

The principal debates surrounding post-collisional potassic magmatism and the Neogene extension of the Tibetan plateau centre on several issues: (1) whether post-collisional potassic magmatism is related to the geodynamic processes responsible for the uplift of the Tibetan plateau (Turner *et al*., 1996), or whether it simply reflects processes such as shear heating in the

crust and subcontinental mantle lithosphere (Kincaid & Silver, 1996); (2) whether magmatism and extension are genetically related (Williams *et al.*, 2001), or whether extension merely represents the local accommodation of plate boundary forces by the upper crust (McCaffrey & Nabelek, 1998); and thus (3), to what extent can constraints on the magma source regions (composition, mineralogy), melting regimes (melt fraction, pressure, temperature) and the spatial and temporal distribution of potassic, post-collisional lavas across the Tibetan plateau be used to discriminate between competing geodynamic models that describe the evolution of the Tibetan plateau.

Shear heating

The process of shear heating (Kincaid & Silver, 1996)—heating through viscous dissipation in the upper-mantle lithosphere and lowermost crust—has been suggested as a mechanism for the generation of small-degree melts within the mantle lithosphere. The maximum temperatures realized by viscous heating (1050°C, at depths >90 km, for an ambient mantle temperature of 1350°C) lie on the solidus of metasomatized peridotite (1040–1050°C at 1·8–2·5 GPa; Wallace & Green, 1991) and heat is generated most effectively at the crust–mantle interface and is either transferred to the crust by advection, or by the migration of magmas derived from melting in the subcontinental mantle. However, as recognized by Kincaid & Silver (1996), heating and melting reduce viscosity and shear stress, limiting the effectiveness of viscous heating to short periods (~12–15 Myr). Other workers, e.g. Kameyama *et al.* (1999) have argued that the duration of a thermal anomaly produced by shear heating is even lower, ~5 kyr. Given that magmatism in southern and northern Tibet spans durations of 24 Myr and 18 Myr, respectively, we consider shear heating as an unlikely mechanism for inducing melting. Furthermore, neither Kincaid & Silver (1996) nor Kameyama *et al.* (1999) considered the viscosity effects of hydrous mineral phases such as pargasitic amphibole and phlogopite, which have been shown to be present in significant modal proportions in the mantle lithosphere of northern and southern Tibet.

Extension, plateau elevation and potassic magmatism

Field observations (Armijo *et al.*, 1986) and earthquake fault plane solutions (Molnar & Tapponnier, 1978) indicate the continuing east–west extension of the Tibetan plateau. The magnitude of this extension is <1% (Armijo *et al.*, 1986). The onset of normal faulting and graben formation has been constrained to ~14 Ma in southern Tibet (Coleman & Hodges, 1995), ~13·5 Ma in central Tibet (Blisniuk *et al.*, 2001) and ~4·5 Ma in NW Tibet (Zheng *et al.*, 2000). This extension has been interpreted to be related to either the increase in the potential energy of the plateau following uplift, or else to plate boundary forces that may be unrelated to plateau formation. Although the data are scarce, the wide distribution of extension calls into question models that relate extension to boundary processes such as oroclinal bending (Klootwijk *et al.*, 1985) and radial convergence (McCaffrey & Nabelek, 1998) that relate to the curved shape of the indenting Indian plate. In contrast, recent palaeoelevation constraints indicating that southern Tibet had reached its current elevation by ~15 Ma (Garzione *et al.*, 2000; Rowley *et al.*, 2001; Spicer *et al.*, 2003) lend support to the view that the onset of crustal thinning at ~14 Ma is in some way related to plateau uplift. The presence of ~18 Ma north–south-trending dykes (the Pabbai Zong dykes) in southern Tibet suggests that there is some link between extension and magmatism (Williams *et al.*, 2001). However, the magnitude of extension in southern Tibet is insufficient to cause melting of normal potential temperature mantle (McKenzie & Bickle, 1988), and other mechanisms of inducing melting in the sub-continental lithospheric mantle are required.

Assessment of competing models for the uplift of the Tibetan plateau

Geodynamic models for the uplift and geodynamic evolution of the Tibetan plateau include stepwise growth by south-directed intracontinental subduction on reactivated terrane boundaries (Tapponnier *et al.*, 2001); delamination of the entire mantle lithosphere beneath Tibet (Bird, 1979); slab break-off (Davies & von Blanckenburg, 1995; Chemenda *et al.*, 2000); partial thinning and removal of the lowermost lithospheric mantle as a result of convective instabilities (England & Houseman, 1988; Houseman & Molnar, 1997; Conrad & Molnar, 1999). Of these models, only delamination and convective removal predict the association of magmatism with extension and plateau uplift, as plateau uplift is caused by the asthenosphere replacing the thinned mantle lithosphere.

Although models of continental subduction are not in themselves implausible, it is difficult to envisage how continental subduction could cause lithospheric mantle melting in northern Tibet, as the subduction of Asian mantle lithosphere beneath northern Tibet and the associated crustal thickening will not elevate the geotherm—rather, the rapid thickening of the continental lithosphere will cause the equilibrium thermal gradient to decrease in the same proportions as the lithosphere is thickened (Platt & England, 1994). Thus, the processes of continental subduction do not

supply heat to the mantle lithosphere and cannot cause its melting, even though the process of intracontinental subduction may well cause metasomatic enrichment of the north Tibetan SCLM via fluid release from the subducting plate. Although it has been argued that the process of continental subduction in northern Tibet could cause crustal melting in response to the introduction of volatiles from the subducting material into the lower crust, the pattern of magmatism on the Tibetan plateau is not in agreement with the stepwise subduction of continental lithosphere underneath the boundaries delimiting the Kunlun, Songpan–Ganze, Qiangtang and Lhasa terranes (Fig. 1) as this would result in sub-parallel bands of calc-alkaline magmatism, which are not observed. Moreover, Cooper *et al.* (2002) pointed out that that the absence of ^{238}U excesses relative to ^{230}Th in Quaternary volcanics from the Ashikule Basin in NW Tibet is inconsistent with a model in which melting is triggered by late fluid influx.

Models of delamination and convective removal share the assumption that the continental lithosphere behaves as a continuum and that plate convergence is accommodated by the distributed deformation and thickening of the entire lithosphere, which thermally destabilizes the SCLM with respect to the asthenosphere, resulting in its subsequent removal (Houseman *et al.*, 1981). However, this process has been depicted in different ways. In the delamination model, the entire SCLM is peeled off as a slab and replaced by hot asthenosphere that comes into direct contact with the base of the crust (Bird, 1979). This results in decompression melting of the asthenosphere, and the generation of considerable volumes of basaltic magmas, with associated crustal melting. Such large volumes of mafic magmas are not observed on the plateau and, in any case, the degrees of melting required to produce the northern and southern mafic magmas are extremely low, ruling out delamination as a viable geodynamic mechanism for the origin of the Tibetan plateau. In addition, this model predicts a migrating front of SCLM removal, which is not supported by the age distribution of magmatism on the plateau (Fig. 1). Houseman *et al.* (1981) proposed partial removal of the SCLM by convective thinning at its base as a consequence of the homogeneous shortening of the upper conducting layer of the SCLM and the thermal boundary layer. This model differs from that of Bird (1979) in that only the lower part of the SCLM is removed, and the asthenosphere does not come into contact with the base of the crust. In this model, plateau uplift is simply an isostatic response to the removal of part of the relatively cold and dense SCLM, and its replacement with hotter asthenosphere. However, the convergent boundary forces cannot support the

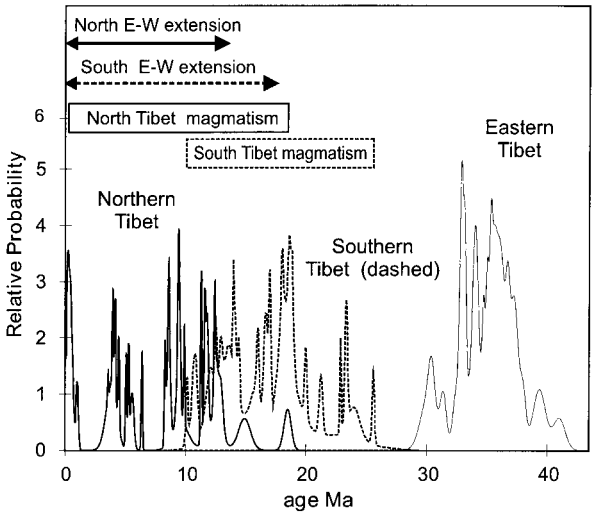

Fig. 17. Age distribution of Tibetan magmatism. Cumulative probability of the timing of shoshonite magmatism in northern, southern and eastern Tibet. Cumulative probabilities were calculated using the Isoplot program (Ludwig, 1999); the calculation involves summing the individual ages and their associated errors within each group and then normalizing to the number of samples in the group (so that the area under the probability curve is equal for each group, allowing their probabilities to be directly compared with each other). It is assumed that the errors on individual ages (2 SD) have a Gaussian distribution around the quoted age. Data from this study, Wanming (1991), Turner *et al.* (1996), Chung *et al.* (1998), Miller *et al.* (1999) and Williams *et al.* (2001). Also shown are geochronological constraints for the onset of east–west extension in southern Tibet (Williams *et al.*, 2001) and in northern Tibet (Yin *et al.*, 1999; Zheng *et al.*, 2000; Blisniuk *et al.*, 2001).

increase in potential energy and elevation resulting from convective removal of the lowermost part of the SCLM and, following thermal relaxation, the potential energy excess is dissipated by normal faulting (England & Houseman, 1989).

The replacement of the lowermost part of the SCLM with asthenosphere results in a transient elevation in the thermal structure of the remaining SCLM, and allows the geotherm to cross the hydrated peridotite solidus, permitting partial melting of metasomatized regions within the SCLM. On this basis, Turner *et al.* (1993, 1996), Chung *et al.* (1998) and Miller *et al.* (1999) invoked convective removal as the most likely mechanism for explaining the petrogenesis of the northern and southern post-collisional lavas. Convective thinning is consistent with the shallow depths of magmatism inferred for the northern and southern samples in this paper, and can also explain the association of extension with post-collisional magmatism in southern and northern Tibet; the initiation of extension postdates the onset of magmatism in southern and north–central Tibet by 7 Myr and 5 Myr, respectively (Fig. 17, references in caption). However, synchronous removal of the lower part of the SCLM (Houseman

et al., 1981) is inconsistent with this pattern of volcanism and extension. Moreover, several studies have suggested that convective thinning should be an event with a time scale no greater than ~5 Myr (Lenardic & Kaula, 1995), considerably shorter than any of the documented phases of magmatism. One means of reconciling prolonged phases of SCLM-derived magmatism with the short time scales inferred for convective thinning (Lenardic & Kaula, 1995) is to invoke more episodic Rayleigh–Taylor instabilities in the asthenospheric mantle beneath the plateau, with variable length scales and amplitudes (Conrad & Molnar, 1999).

In Fig. 17, it can be seen that there are three overlapping 'pulses' of magmatism corresponding to magmatism in the northern (including the central plateau region), southern and eastern regions of the Tibetan plateau. One possible explanation for this is that different geodynamic processes operated in these different regions of the plateau. Recently, Maheo *et al.* (2002) invoked the process of slab break-off to explain the generation of Neogene granitoids and lamprophyres in the Karakorum, which have similar trace element and isotopic characteristics of the southern Tibetan samples, and that of younger (<10 Ma) magmatic rocks that have depleted mantle Nd and Hf isotopic signatures indicative of a depleted mantle source. Maheo *et al.* (2002) interpreted this magmatic sequence in terms of the formation of a slab window after the break-off of most of the subducting slab, followed by the progressive deepening of the window as a result of the continuing convergence of the Indian plate. In the sequence of events, the shallowest levels of the lithospheric mantle would melt first (at the Moho, ~65 km for southern Tibet), followed by progressively deeper melts sourced at the base of the lithospheric mantle (>100 km), and then by melts derived, at least in part, from the convecting asthenosphere. A role for slab break-off is supported by recent tomographic data, which suggest that the subducting Indian lithosphere is actively destroyed as it underthrusts Tibet (Kosarev *et al.*, 1999; Van der Voo *et al.*, 1999). However, slab break-off does not explain the association of potassic magmatism with east–west extension in southern Tibet.

In the context of the slab break-off model, the occurrence of melts with depleted mantle signatures in southern Tibet is surprisingly rare. Although the south-east sample series contains samples that plot close to Bulk Earth values (Fig. 6a), these samples are all fairly evolved (Fig. 6b) and cannot be regarded as primitive melts. None the less, the scarcity of asthenospheric melts does not in itself rule out slab break-off, but could simply indicate that the Indian slab had switched from a deep subduction mode to underthrusting by this time, as discussed below.

In the model of Maheo *et al.* (2002), there is no lithospheric thinning, and thus we would expect to see magmas with a strong garnet signature succeeding the spinel-facies magmas. However, it has been demonstrated earlier that the southern Tibet mafic magmas do not have garnet signatures, and that they were derived by melting at depths of 65–80 km in the SCLM. This absence of garnet-facies melts does not rule slab break-off out as a viable mechanism, but does indicate that if slab break-off has operated beneath the southern margin of the Tibetan plateau, then it must have been associated with lithospheric thinning. This would also explain the association of potassic magmatism and extension in southern Tibet. Thinning of the lithospheric mantle could result from asthenospheric upwelling and thermal erosion following break-off and the creation of a slab window (Davies & von Blanckenburg, 1995, 1997; Von Blanckenburg & Davies, 1995). Recent analogue modelling (Pysklywec *et al.*, 2000) demonstrates that the SCLM can exhibit a range of transitional deformation modes during convergence, including Rayleigh–Taylor type instabilities, ablative SCLM consumption and slab break-off, lending support to a combination of slab break-off and Rayleigh–Taylor convective removal processes in southern Tibet.

If we accept such a combined slab break-off–SCLM erosion model for southern Tibet, then the earliest dated mafic magmatism indicates that 'break-off' and local thinning of the overlying SCLM occurred by 25 Ma (Miller *et al.*, 1999), followed by plateau uplift and extension and dyke emplacement at ~18 Ma (Williams *et al.*, 2001). This is consistent with several lines of evidence that indicate that southern Tibet was at its present altitude by ~15 Ma (Garzione *et al.*, 2000; Rowley *et al.*, 2001; Spicer *et al.*, 2003). In this scenario, the cessation of mafic magmatism in southern Tibet at 10 Ma (Maheo *et al.*, 2002) and the scarcity of mafic, asthenosphere-derived melts could reflect the change in the behaviour of underthrusting Indian slab from near vertical subduction at ~60 Ma (O'Brien *et al.*, 1999; de Sigoyer *et al.*, 2000) to its present-day underthrusting behaviour (Kosarev *et al.*, 1999). The underthrusting Indian plate would shield the remaining SCLM against further erosion and would also provide a 'lid' on decompression melting of the asthenosphere

Therefore, although elements of episodic convective removal envisaged by Conrad & Molnar (1999) and slab detachment (Chemenda *et al.*, 2000) can be applied to north and south Tibet, respectively, their mechanisms and interaction with each other are more complex than accounted for in any of the present models. This may reflect the different nature of the SCLM beneath southern and northern Tibet—the

more refractory southern source is likely to be more buoyant and thus resistant to convective processes. A combination of both slab break-off and convective removal is plausible—consistent with the patterns of surface volcanism on the plateau and evidence for diachronous plateau uplift (Copeland *et al*., 1987; Copeland & Harrison, 1990; Mock *et al*., 1999; Zheng *et al*., 2000) and seismic constraints (Kosarev *et al*., 1999). Although it is difficult to constrain the absolute timing of SCLM thinning in response to these processes, it is clear that it must pre-date the oldest shoshonitic magmatism, constrained to be 25 Ma in southern Tibet (Miller *et al*., 1999) and 19 Ma in the north (Turner *et al*., 1996). The belt of 30–37 Ma potassic volcanism in eastern Tibet (Chung *et al*., 1998) cannot be explained by convective thinning in response to distributed shortening, as the lithosphere in this region was not thickened by ~35 Ma (Leloup *et al*., 1995).

CONCLUSIONS

Potassic mafic magmatism in north and south Tibet is derived from two distinct metasomatized lithospheric mantle source regions, both characterized by contrasting major element and isotopic signatures. Inverse modelling of trace element data reveals that both source regions are characterized by LILE enrichment relative to the HFSE and are depleted in the HREE relative to primitive mantle. The LILE enrichment can be related to metasomatism during earlier subduction events; the HREE depletion is indicative of prior melt extraction, probably related to initial stabilization of the SCLM. The similarity of the source region trace-element compositions can be reconciled with their contrasting isotopic and major element signatures if metasomatism was a consequence of similar processes (e.g. subduction), albeit at different times with components of different ages. The shallow depths of SCLM melting require significant lithospheric thinning, but the different degrees of partial melting inferred for the northern and southern Tibetan mafic samples suggest important differences in source fertility and/or the geodynamic processes operating in northern and southern Tibet. These melting regimes, the temporal association of melting with extension and the spatial–temporal distribution of magmatism on the Tibetan plateau can be related to episodic convective removal in northern Tibet and to lithospheric erosion associated with slab break-off in the south. Therefore, the uplift of the Tibetan plateau can be related to more than one geodynamic process and is likely to have been diachronous in nature. This information must be taken into account in models that link Cenozoic climate to plateau uplift (Harrison *et al*., 1993; Molnar *et al*., 1993).

ACKNOWLEDGEMENTS

We are grateful to N. Rogers, I. Parkinson and M. Petermann for helpful discussions, and we thank C. Otley, D. Vance, P. Van Calsteren, M. Gilmour, H. Chapman and M. Bickle for their analytical assistance. Extremely helpful and constructive comments from N. Arnaud and two anonymous reviewers are gratefully acknowledged. The Executive Editor, M. Wilson, is thanked for many helpful comments in her handling of this manuscript. H.M.W. was funded by NERC studentship GT4/97/213, S.P.T. by the Royal Society.

SUPPLEMENTARY DATA

Supplementary data for this paper are available on *Journal of Petrology* online.

REFERENCES

Adam J., Green, T. H. & Sie, S. H. (1993). Proton microprobe determined partitioning of Rb, Sr, Ba, Y, Zr, Nb and Ta between experimentally produced amphiboles and silicate melts with variable F content. *Chemical Geology* **109**, 29–49.

Ahmad, T., Harris, N., Bickle, M., Chapman, H., Bunbury, J. & Prince, C. (2000). Isotopic constraints on the structural relationships between the Lesser Himalaya Series and the High Himalayan Crystalline Series, Garhwal Himalaya. *Geological Society of America Bulletin* **112**(3), 467–477.

Albarède, F. (1983). Inversion of batch melting equations and the trace element pattern of the mantle. *Journal of Geophysical Research* **88**(B12), 10573–10583.

Anderson, A. T. & Greenland, L. P. (1969). Phosphorus fractionation diagram as a quantitative indicator of crystallization differentiation of basaltic liquids. *Geochimica et Cosmochimica Acta* **33**(4), 493–505.

Armijo, R., Tapponier, P., Mercier, J. L. & Han, T.-L. (1986). Quartenary extension in Southern Tibet: field observations and tectonic implications. *Journal of Geophysical Research* **91**(B14), 13803–13872.

Arnaud, N. O. (1992). Apport de la thermochronologie $^{40}Ar/^{39}Ar$ sure feldspath potassique connaissance de la tectonique Cénozoïque d'Asie. Ph.D. thesis, Université de Clermont-Ferrand.

Arnaud, N. O., Vidal, P., Tapponnier, P., Matte, P. & Deng, W. M. (1992). The high K_2O volcanism of northwestern Tibet: geochemistry and tectonic implications. *Earth and Planetary Science Letters* **111**, 351–367.

Becker, H., Jochum, K. P. & Carlson, R. W. (2000). Trace element fractionation during dehydration of eclogites from high-pressure terranes and the implications for element fluxes in subduction zones. *Chemical Geology* **163**(1–4), 65–99.

Bird, P. (1979). Continental delamination and the Colorado Plateau. *Journal of Geophysical Research* **84**, 7561–7571.

Blisniuk, P. M., Hacker, B. R., Glodny, J., Ratschbacher, L., Bi, S., Wu, Z., McWilliams, M. O. & Calvert, A. (2001). Normal faulting in central Tibet since at least 13·5 Myr ago. *Nature* **412**(6847), 628–632.

Brenan, J. M., Shaw, H. F., Phinney, D. L. & Ryerson, F. J. (1994). Rutile–aqueous fluid partitioning of Nb, Ta, Hf, Zr, U and Th:

implications for high field strength depletions in island-arc basalts. *Earth and Planetary Science Letters* **128**, 327–339.

Brunet, F. & Chazot, G. (2001). Partitioning of phosphorus between olivine, clinopyroxene and silicate glass in a spinel lherzolite xenolith from Yemen. *Chemical Geology* **176**(1–4), 51–72.

Chemenda, A. I., Burg, J.-P. & Mattauer, M. (2000). Evolutionary model of the Himalaya–Tibet system: geopoem based on new modelling, geological and geophysical data. *Earth and Planetary Science Letters* **174**, 397–409.

Chung, S.-L., Lo, C.-H., Lee, T.-Y., Zhang, Y., Xie, Y., Li, X., Wang, K.-L. & Wang, P.-L. (1998). Diachronous uplift of the Tibetan plateau starting from 40 My ago. *Nature* **394**, 769–773.

Class, C. & Goldstein, S. L. (1997). Plume–lithosphere interactions in the ocean basins: constraints from the source mineralogy. *Earth and Planetary Science Letters* **150**, 245–260.

Coleman, M. & Hodges, K. (1995). Evidence for Tibetan plateau uplift before 14 My ago from a new minimum age for east–west extension. *Nature* **374**, 49–52.

Conrad, C. P. & Molnar, P. (1999). Convective instability of a boundary layer with temperature- and strain-dependent viscosity in terms of 'available buoyancy'. *Geophysical Journal International* **131**, 51–68.

Cooper, K. M., Reid, M. R., Dunbar, N. W. & McIntosh, W. C. (2002). Origin of mafic magmas beneath northwestern Tibet: constraints from ^{230}Th–^{238}U disequilibria. *Geochemistry, Geophysics, Geosystems (G-cubed)* **3**(1), 10.1029/2002GC000332.

Copeland, P. & Harrison, T. M. (1990). Episodic rapid uplift in the Himalaya revealed by ^{40}Ar/^{39}Ar analysis of detrital K-feldspar and muscovite, Bengal fan. *Geology* **18**, 354–357.

Copeland, P., Harrison, T. M., Kidd, W. S. F., Xu, R. & Zhang, Y. (1987). Rapid early Miocene acceleration of uplift in the Gangdese belt, Xizang (southern Tibet), and its bearing on accommodation mechanisms of the India–Asia collision. *Earth and Planetary Science Letters* **86**, 240–252.

Coulon, C., Maluski, H., Bollinger, C. & Wang, S. (1986). Mesozoic and Cenozoic volcanic rocks from central and southern Tibet: ^{39}Ar/^{40}Ar dating, petrological characteristics and geodynamical significance. *Earth and Planetary Science Letters* **79**, 281–302.

Dalpe, C. & Baker, D. R. (1994). Partition coefficients for rare-earth elements between calcic amphibole and Ti-rich basanite glass at 1·5 GPa, 1100°C. (Goldschmidt Conference Extended Abstracts.) *Mineralogical Magazine* **58A**, 207–208.

Davies, J. H. & von Blanckenburg, F. (1995). Slab breakoff: a model of lithosphere detachment and its test in the magmatism and deformation of collisional orogens. *Earth and Planetary Science Letters* **129**, 85–102.

Davies, J. H. & von Blanckenburg, F. (1997). Thermal controls on slab breakoff and the rise of high-pressure rocks during continental collisions. In: Hacker, B. R. & Liou, J. G. (eds) *When Continents Collide: Geodynamics and Geochemistry of Ultrahigh Pressure Rocks*, *Vol. 1*. Dordrecht: Kluwer Academic, pp. 97–115.

Deer, W. A., Howie, R. A. & Zussmann, J. (1992). *An Introduction to the Rock-forming Minerals*, 2nd edn. Harlow: Longman, 696 pp.

Deng, W. (1991). Cenozoic volcanism and intraplate subduction at the northern margin of the Tibetan Plateau. *Chinese Journal of Geochemistry* **10**(2), 140–152.

Deng, W. (1997). Cenozoic volcanism and lithosphere tectonic evolution in the northern Tibetan plateau, China. In: Li, Z. (ed.) *30th International Geological Conference*. Zeist, Netherlands: VSP, pp. 3–12.

DePaulo, D. J. (1981). Trace element and isotopic effects of combined wall rock assimilation and fractional crystallisation. *Earth and Planetary Science Letters* **53**, 189–202.

de Sigoyer, J., Chavagnac, V., Blichert-Toft, J., Villa, I. M., Luais, B., Guillot, S., Cosca, M. & Mascle, G. (2000). Dating the Indian continental subduction and collisional thickening in the northwest Himalaya: multichronology of Tso Morari eclogites. *Geology* **28**(6), 487–490.

Dewey, J. F. (1988). Extensional collapse of orogens. *Tectonics* **6**, 1123–1139.

England, P. & Houseman, G. (1988). The mechanics of the Tibetan plateau. *Philosophical Transactions of the Royal Society of London, Series A* **326**, 301–320.

England, P. & Houseman, G. (1989). Extension during continental convergence, with application to the Tibetan plateau. *Journal of Geophysical Research* **94**(B12), 17561–17579.

Foley, S. (1992*a*). Petrological classification of the source components of potassic magmas: geochemical and experimental constraints. *Lithos* **28**, 187–204.

Foley, S. F. (1992*b*). Vein-plus-wall-rock melting mechanisms in the lithosphere and the origins of potassic alkaline magmas. *Lithos* **28**, 435–453.

Foley, S. F. & Wheller, G. E. (1990). Parallels in the origin of the geochemical signatures of island arc volcanics and continental potassic igneous rocks: the role of residual titanites. *Chemical Geology* **85**, 1–18.

Foley, S. F., Jackson, S. E., Fryer, B. J., Greenough, J. D. & Jenner, G. A. (1996). Trace element partition coefficients for clinopyroxene and phlogopite in an alkaline lamprophyre from Newfoundland by LAM–ICP-MS. *Geochimica et Cosmochimica Acta* **60**(4), 629–638.

Foley, S. F., Barth, M.G. & Jenner, G.A. (2000). Rutile/melt partition coefficients for trace elements and an assessment of the influence of rutile on the trace element characteristics of subduction zone magmas. *Geochimica et Cosmochimica Acta* **64**(5), 933–938.

Frost, B. R., Chamberlain, K. R. & Schumacher, J. C. (2001). Sphene (titanite): phase relations and role as a geochronometer. *Chemical Geology* **172**(1–2), 131–148.

Garzione, C. N., Dettman, D. L., Quade, J., DeCelles, P. G. & Butler, R. F. (2000). High times on the Tibetan Plateau: Palaeoelevation of the Thakkola Graben, Nepal. *Geology* **28**(4), 339–342.

Gill, J. B. (1981). *Orogenic Andesites and Plate Tectonics*. Berlin: Springer, 390 pp.

Green, T. H. (1995). Significance of Nb/Ta as an indicator of geochemical processes in the crust–mantle system. *Chemical Geology* **120**, 347–359.

Green, T. H. & Pearson, N. J. (1986). An experimental study of Nb and Ta partitioning between Ti-rich minerals and silicate liquids at high pressure and temperature. *Geochimica et Cosmochimica Acta* **51**, 55–62.

Green, T. H., Blundy, J. D., Adam, J. & Yaxley, G. M. (2000). SIMS determination of trace element partition coefficients between garnet, clinopyroxene and hydrous basaltic liquids at 2–7·5 GPa and 1080–1200°C. *Lithos* **53**, 165–187.

Gregoire, M., Moine, B. N., O'Reilly, S. Y., Cottin, J. Y. & Giret, A. (2000). Trace element residence and partitioning in mantle xenoliths metasomatised by highly alkaline, silicate- and carbonate-rich melts (Kerguelen Islands, Indian Ocean). *Journal of Petrology* **41**(4), 477–509.

Hacker, B. R., Gnos, E., Ratschbacher, L., Grove, M., McWilliams, M. & Wan, J. (2000). Hot and dry xenoliths from the bottom of Tibet. *Science* **287**, 2463–2466.

Halliday, A. N., Lee, D.-C., Tommasini, S., Davies, G. R., Paslick, C. R., Fitton, J. G. & James, D. E. (1995). Incompatible trace elements in OIB and MORB and source enrichment in the sub-oceanic mantle. *Earth and Planetary Science Letters* **133**, 379–395.

Harris, N. B. W., Xu, R., Lewis, C. L., Hawkesworth, C. J. & Zhang, Y. (1988). Isotope geochemistry of the 1985 Tibet Geotraverse, Lhasa to Golmud. *Philosophical Transactions of the Royal Society of London, Series A* **327**, 263–285.

Harrison, T. M., Copeland, P., Hall, S. A., Quade, J., Burner, S., Ohja, T. P. & Kidd, W. S. F. (1993). Isotopic preservation of Himalayan/Tibetan uplift, denudation and climatic histories of two molasse deposits. *Journal of Geology* **101**, 157–175.

Hart, S. R. (1984). A large-scale isotope anomaly in the Southern Hemisphere mantle. *Science* **309**, 753–757.

Hart, S. R. (1988). Heterogeneous mantle domains: signatures, genesis and mixing chronologies. *Earth and Planetary Science Letters* **90**(3), 273–296.

Hirose, K. (1997). Melting experiments on lherzolite KLB-1 under hydrous conditions and generation of high-magnesian andesitic melts. *Geology* **25**(1), 42–44.

Hirose, K. & Kawamoto, T. (1995). Hydrous partial melting of lherzolite at 1 GPa: the effect of H_2O on the genesis of basaltic magmas. *Earth and Planetary Science Letters* **133**, 463–473.

Hirose, K. & Kushiro, I. (1993). Partial melting of dry peridotites at high pressures: determination of compositions using aggregates of diamond. *Earth and Planetary Science Letters* **114**, 477–489.

Hofmann, A. W. & Feigenson, M. D. (1983). Case studies on the origin of basalt I. Theory and reassessment of Grenada basalts. *Contributions to Mineralogy and Petrology* **84**, 382–389.

Houseman, G. A. & Molnar, P. (1997). Gravitational (Rayleigh–Taylor) instability of a layer with non-linear viscosity and convective thinning of continental lithosphere. *Geophysical Journal International* **128**, 125–150.

Houseman, G. A., McKenzie, D. P. & Molnar, P. (1981). Convective instability of a thickened boundary layer and its relevance for the thermal evolution of continental convergent belts. *Journal of Geophysical Research* **86**(B7), 6115–6132.

Ionov, D. A. & Hofmann, A. W. (1995). Nb–Ta-rich mantle amphiboles and micas: implications for subduction-related metasomatic trace element fractionations. *Earth and Planetary Science Letters* **131**, 341–356.

Jenner, G. A., Foley, S. F., Jackson, S. E., Green, T. H., Fryer, B. J. & Longerich, H. P. (1994). Determination of partition coefficients for trace elements in high pressure–temperature experimental run products by laser ablation microprobe–inductively-coupled-plasma-mass-spectrometry. *Geochimica et Cosmochimica Acta* **58**, 5099–5103.

Jordan, T. H. (1978). Composition and development of the continental tectosphere. *Nature* **274**, 544–548.

Kameyama, M., Yuen, D. A. & Karato, S.-I. (1999). Thermal–mechanical effects of low-temperature plasticity (the Peierls mechanism) on the deformation of a viscoelastic shear zone. *Earth and Planetary Science Letters* **168**, 159–172.

Kelley, S. P. (1995). Ar–Ar dating by laser microprobe. In: Potts, P. J., Bowles, J.F.W., Reed, S.J.B. & Cave, M.R. (eds) *Microprobe Techniques in the Earth Sciences*. London: Chapman and Hall, pp. 327–358.

Kelley, S. P. & Wartho, J.-A. (2000). Rapid kimberlite ascent and the significance of Ar–Ar ages in xenolith phlogopites. *Science* **289**, 609–611.

Kincaid, C. & Silver, P. (1996). The role of viscous dissipation in the orogenic process. *Earth and Planetary Science Letters* **142**, 271–288.

Klein, E. M. & Langmuir, C. M. (1987). Global correlations of ocean ridge basalt chemistry with axial depth and crustal thickness. *Journal of Geophysical Research* **B8**, 8089–8115.

Klemme, S. & O'Neill, H. S. (2000). The near-solidus transition from garnet lherzolite to spinel lherzolite. *Contributions to Mineralogy and Petrology* **138**, 237–248.

Klootwijk, C. T., Conaghan, P. J. & Powell, C. M. (1985). The Himalayan Arc: large-scale continental subduction, oroclinal bending and back-arc spreading. *Earth and Planetary Science Letters* **75**, 167–183.

Kosarev, G., Kind, R., Sobolev, S. V., Yuan, X., Hanka, W. & Oreshin, S. (1999). Seismic evidence for a detached Indian lithospheric mantle beneath Tibet. *Science* **283**, 1306–1309.

LaTourette, T., Hervig, R. L. & Holloway, J. R. (1995). Trace element partitioning between amphibole, phlogopite and basanite melt. *Earth and Planetary Science Letters* **135**, 13–30.

Le Bas, M. J. & Le Maitre, R. W. (1986). A chemical classification of volcanic rocks based on the total alkali–silica diagram. *Journal of Petrology* **27**, 27.

Leloup, P. H., Lacassin, R., Tapponier, P., Scharer, U., Dalai, Z., Xiaohan, L., Liangshang, Z., Shaocheng, J. & Trinh, P. T. (1995). The Ailao Shan–Red River shear zone (Yunnan, China), Tertiary transform boundary of Indochina. *Tectonophysics* **251**, 3–84.

Le Maitre, R. W., Bateman, P., Dudek, A., Keller, J., Lameyre, J., Le Bas, M. J., Sabine, P. A., Schmid, R., Sorensen, H., Streckeisen, A., Woolley, A. R. & Zanettin, B (1989). *A Classification of Igneous Rocks and a Glossary of Terms*. Oxford: Blackwell.

Lenardic, A. & Kaula, W. M. (1995). More thoughts on convergent crustal plateau formation and mantle dynamics with regard to Tibet. *Journal of Geophysical Research* **B8**, 15193–15203.

Liu, J. & Maimaiti, Y. (1989). Distribution and ages of Ashikule volcanoes on the West Kunlun mountains, west China. *Bulletin of Glacier Research* **7**, 193–196.

Lloyd, F. E., Arima, M. & Edgar, A. D. (1985). Partial melting of a phlogopite–clinopyroxenite nodule from south-west Uganda: an experimental study bearing on the origin of highly potassic continental rift volcanics. *Contributions to Mineralogy and Petrology* **91**, 321–329.

Ludwig, K. R. (1999). *Isoplot/Ex: a Geochronological Toolkit for Microsoft Excel*. Berkeley, CA: Berkeley Geochronology Center.

Maheo, G., Guillot, S., Blichert-Toft, J., Rolland, Y. & Pecher, A. (2002). A slab breakoff model for the Neogene thermal evolution of South Karakorum and South Tibet. *Earth and Planetary Science Letters* **195**(1–2), 45–58.

Mahnes, G., Minster, J. F. & Allegre, C. J. (1978). Comparative uranium–thorium–lead and rubidium–strontium study of the Saint Severin amphoterite: consequences for early solar system chronology. *Earth and Planetary Science Letters* **95**, 53–72.

McCaffrey, R. & Nabelek, J. (1998). Role of oblique convergence in the active deformation of the Himalayas and southern Tibet plateau. *Geology* **26**(8), 691–694.

McKenna, L. W. & Walker, J. D. (1990). Geochemistry of crustally derived igneous rocks from the Ulugh Muztagh area, Northern Tibet, and their implications for the formation of the Tibetan plateau. *Journal of Geophysical Research* **95**(B13), 21483–21502.

McKenzie, D. P. & Bickle, M. J. (1988). The volume and composition of melts generated by extension of the lithosphere. *Journal of Petrology* **29**, 625–679.

McKenzie, D. & O'Nions, R. K. (1991). Partial melt distributions from inversion of rare earth element concentrations. *Journal of Petrology* **35**(5), 1021–1091.

Michard, A., Gurriet, P., Soudant, M. & Albarède, F. (1985). Nd isotopes in French Phanerozoic shales: external vs internal aspects of crustal evolution. *Geochimica et Cosmochimica Acta* **49**, 601–610.

Miller, C., Schuster, R., Klotzli, U., Mair, V., Frank, W. & Purtscheller, F. (1999). Post-collisional potassic and ultrapotassic magmatism in SW Tibet: geochemical, Sr–Nd–Pb–O isotopic

constraints for mantle source characteristics and petrogenesis. *Journal of Petrology* **40**(9), 1399–1424.

Minster, J. F. & Allègre, C. J. (1978). Systematic use of trace elements in igneous processes. Part III: Inverse problem of batch partial melting in volcanic suites. *Contributions to Mineralogy and Petrology* **68**, 37–52.

Mock, C., Arnaud, N. O. & Cantagrel, J.-M. (1999). An early unroofing in northwestern Tibet? Constraints from ^{40}Ar–^{39}Ar thermochronology on granitoids from the eastern Kunlun range (Qianghai, NW China). *Earth and Planetary Science Letters* **171**, 107–122.

Molnar, P. & Tapponnier, P. (1978). Active tectonics of Tibet. *Journal of Geophysical Research*, **83**(B11), 5361–5375.

Molnar, P., England, P. & Martinod, J. (1993). Mantle dynamics, uplift of the Tibetan plateau, and the Indian Monsoon. *Reviews of Geophysics* **31**(4), 357–396.

Nelson, D. R., McCulloch, M. & Sun, S. S. (1985). The origins of ultrapotassic rocks as inferred from Sr, Nd and Pb isotopes. *Geochimica et Cosmochimica Acta* **50**, 231–245.

O'Brien, P., Zotov, N., Law, R., Khan, M. A. & Jan, M. Q. (1999). Coesite in eclogite from the Upper Kaghan Valley, Pakistan: a first record and implications. In: Sobel, E., Appel, E. & Ratschbacher, L. (eds) *Terra Nova 99/2. 14th Himalayan–Karakorum–Tibet Workshop*. Kloster-Ettal, Germany, pp. 109–110.

Pearce, J. A. & Mei, H. (1988). Volcanic rocks of the 1985 Tibet Geotraverse: Lhasa to Golmud. *Philosophical Transactions of the Royal Society of London, Series A* **327**, 169–201.

Pearce, J. A. & Parkinson, I. J. (1993). Trace element models for mantle melting: application to volcanic arc petrogenesis. In: Prichard, H. M., Alabaster, T., Harris, N. B. W. & Neary, C. R. (eds) *Magmatic Processes and Plate Tectonics*, *Geological Society, London, Special Publications* **76**, 373–403.

Pertermann, M. & Hirschmann, M. M. (2003*a*). Partial melting experiments on a MORB-like pyroxenite between 2 and 3 GPa: constraints on the presence of pyroxenite in basalt source regions from the solidus location and melting rate. *Journal of Geophysical Research* **108**(B2), 2125–2137.

Pertermann, M. & Hirschmann, M. M. (2003*b*). Anhydrous partial melting experiments on MORB-like eclogite: phase relations, phase compositions and mineral/melt partitioning of major elements at 2–3 GPa. *Journal of Petrology* **44**, 2173–2201.

Plank, T. & Langmuir, C. H. (1998). The chemical composition of subducting sediment and its consequences for the crust and mantle. *Chemical Geology* **145**, 325–394.

Platt, J. P. & England, P. C. (1994). Convective removal of lithosphere beneath mountain belts: thermal and mechanical consequences. *American Journal of Science* **294**, 301–336.

Pollack, H. S. (1986). Cratonisation and thermal evolution of the mantle. *Earth and Planetary Science Letters* **80**, 175–182.

Potts, P. J., Webb, P. C. & Watson, J. S. (1984). Energy dispersive X-ray fluorescence of silicate rocks for major and trace elements. *X-ray Spectrometry* **13**, 2–15.

Pysklywec, R. N., Beaumont, C. & Fullsack, P. (2000). Modelling the behaviour of the continental mantle lithosphere during plate convergence. *Geology* **28**, 655–658.

Renne, P. R., Swisher, C. C., Deino, A. L., Karner, D. B., Owens, T. L. & DePaolo, D. J. (1998). Intercalibration of standards, absolute ages and uncertainties in dating. *Chemical Geology* **145**(1–2), 117–152.

Richard, P., Shimizu, N. & Allègre, C.J. (1976). $^{143}Nd/^{144}Nd$, a natural tracer: an application to oceanic basalts. *Earth and Planetary Science Letters* **31**, 269–278.

Robinson, J. A. C. & Wood, B. J. (1998). The depth of the spinel to garnet transition at the peridotite solidus. *Earth and Planetary Science Letters* **164**, 277–284.

Rowley, D. B., Pierrehumbert, R. T. & Currie, B. S. (2001). A new approach to stable isotope-based paleoaltimetry: implications for paleoaltimetry and paleohypsometry of the High Himalaya since the Late Miocene. *Earth and Planetary Science Letters* **188**, 253–268.

Ryerson, F. J. & Watson, E. B. (1987). Rutile saturation in magmas: implications for Ti–Nb–Ta depletions in arc island-arc basalts. *Earth and Planetary Science Letters* **86**, 225–239.

Schmidt, K. H., Bottazi, P., Vannucci, R. & Mengel, K. (1999). Trace element partitioning between phlogopite, clinopyroxene and leucite lamproite melt. *Earth and Planetary Science Letters* **168**, 287–299.

Shaw, D. M. (1970). Trace element fractionation during anatexis. *Geochimica and Cosmochimica Acta* **84**, 237–243.

Silver, P. G., Carlson, R. W. & Olson, P. (1988). Deep slabs, geochemical heterogeneity, and the large-scale structure of mantle convection. *Annual Review of Earth and Planetary Sciences* **16**, 477–541.

Spera, F. J. (1987). Dynamics of translithospheric migration of metasomatic fluid and alkaline magma. In: Menzies, M. A. & Hawkesworth, C. J. (eds) *Mantle Metasomatism*. London: Academic Press, pp. 1–18.

Spicer, R. A., Harris, N. B. W., Widdowson, M., Herman, A. B., Guo, S., Valdes, P., Wolfe, J. A. & Kelley, S. P. (2003). Constant elevation of southern Tibet over the past 15 million years. *Nature* **421**, 622–624.

Sun, S. & McDonough, W. F. (1989). Chemical and isotopic systematics of oceanic basalts: implications for mantle composition and processes. In: Saunders, A. D. & Norry, M. J. (eds) *Magmatism in the Ocean Basins*. *Geological Society, London, Special Publications* **42**, 313–345.

Takahashi, E. (1986). Melting of dry peridotite KLB-1 up to 14 GPa: implications on the origin of peridotitic upper mantle. *Journal of Geophysical Research* **91**(B9), 9367–9382.

Tapponnier, P., Xu, Z., Roger, F., Meyer, B., Arnaud, N., Wittlinger, G. & Yang, J. (2001). Oblique stepwise rise and growth of the Tibet Plateau. *Science* **294**, 1671–1677.

Taylor, S. R. & McLennan, S. (1995). The geochemical composition of the continental crust. *Reviews of Geophysics* **33**(2), 241–265.

Tsuruta, K. & Takahashi, E. (1998). Melting study of an alkali basalt JB-1 up to 12·5 GPa: behavior of potassium in the deep mantle. *Physics of the Earth and Planetary Interiors* **107**(1–3), 119–130.

Turner, S. & Hawkesworth, C. (1995). The nature of the subcontinental mantle: constraints from the major-element compositions of continental flood basalts. *Chemical Geology* **120**, 295–314.

Turner, S., Sandiford, M. & Foden, J. (1992). Some geodynamic and compositional constraints on 'postorogenic' magmatism. *Geology* **20**, 931–934

Turner, S., Hawkesworth, C., Liu, J., Rogers, N., Kelley, S. & Van Calsteren, P. (1993). Timing of Tibetan uplift constrained by analysis of volcanic rocks. *Nature* **364**, 50–53.

Turner, S., Arnaud, N., Liu, J., Rogers, N., Hawkesworth, C., Harris, N., Kelley, S., Van Calsteren, P. & Deng, W. (1996). Post-collision, shoshonitic volcanism on the Tibetan plateau: implications for convective thinning of the lithosphere and the source of ocean island basalts. *Journal of Petrology* **27**(1), 45–71.

Van der Voo, R., Spakman, W. & Bijwaard, H. (1999). Tethyan subducted slabs under India. *Earth and Planetary Science Letters* **171**, 7–20.

Von Blanckenburg, F. & Davies, H. J. (1995). Slab breakoff: a model for syncollisional magmatism and tectonics in the Alps. *Tectonics* **14**(1), 120–131.

Wallace, M. E. & Green, D. T. (1991). The effect of bulk rock composition on the stability of amphibole in the upper mantle: implications for solidus peridotites and mantle metasomatism. *Mineralogy and Petrology* **44**, 1–19.

Walter, M. J. (1998). Melting of garnet peridotite and the origin of komatiite and depleted lithosphere. *Journal of Petrology* **39**(1), 29–60.

Williams, H., Turner, S., Kelley, S. & Harris, N. (2001). Age and composition of dikes in Southern Tibet: new constraints on the timing of east–west extension and its relationship to post-collisional magmatism. *Geology* **29**(4), 339–342.

Yaxley, G. M., Crawford, A. J. & Green, D. H. (1991). Evidence for carbonatite metasomatism in spinel peridotite xenoliths from western Victoria, Australia. *Earth and Planetary Science Letters* **107**, 305–317.

Yin, A., Kapp, P. A., Murphy, M. A., Manning, C. E., Harrison, T. M., Grove, M., Ding, L., Deng, X.-G. & Wu, C.-M. (1999). Significant Late Neogene east-west extension in northern Tibet. *Geology* **27**(9), 787–790.

Zheng, H., Powell, C. M., An, Z., Zhou, J. & Dong, G. (2000). Pliocene uplift of the northern Tibetan Plateau. *Geology* **28**(8), 715–718.

Zindler, A. & Hart, S. (1986). Chemical geodynamics. *Annual Review of Earth and Planetary Sciences* **14**, 493–571.

APPENDIX

This Appendix provides details of the regression and inverse modelling procedures documented in the main text. Table A1 lists the samples from the various subgroups in northern and southern Tibet that were combined to form the two datasets used in the regressions to 6 wt % MgO and the inverse modelling. Table A1 also lists the MgO contents (given in wt %) and La contents (ppm, corrected to 6 wt % MgO) for each sample used. The data sources cited in Table A1 are given in the reference list of the main text.

The raw trace element data (presented in Table 2 of the main text, or else available in the references cited below and given in full in the main text) were first corrected to 6 wt % MgO by linear regression in Microsoft Excel. The details of this regression, i.e. slopes, intercepts and r^2 values, are given in Table A2 for northern Tibet, and in Table A3 for southern Tibet.

The corrected trace element compositions were then plotted against La (also corrected to 6 wt % MgO; the $La_{(6)}$ values for each sample are given in Table A1). Linear regression lines were fitted to the trends defined by the trace elements of interest against La. From these regressions, a slope and intercept were obtained for each element, for both the northern and southern regression groups. The slopes, intercepts and r^2 values for the regressions against La are given in Tables A2 (northern Tibet) and A3 (southern Tibet). These

Table A1: Sample subsets used in inverse modelling

Series	Location	Data source	Sample	MgO (wt %)	$La_{(6)}$ (ppm)
South Tibet					
S.-W.	Shiquanhe	1	JPT24A	2·8	105·8
S.-W.	Shiquanhe	1	JPT24B	5·4	69·2
S.-W.	Shiquanhe	1	JPT24C	6·0	58·2
P.Z.	Pabbai Zong	1	JPT7	4·6	70·9
P.Z.	Pabbai Zong	2	T3B/98	5·4	102·6
P.Z.	Pabbai Zong	2	T4A/98	7·2	119·5
P.Z.	Pabbai Zong	2	T5A/98	4·7	71·8
P.Z.	Pabbai Zong	1	T5B/98	3·9	81·5
S.-W.	Xungba	3	TE008/93	5·1	122·2
S.-W.	Xungba	3	TE011/93	5·1	25·5
S.-W.	Jarga	3	TE117/93	6·9	70·0
S.-W.	Jarga	3	TE118/93	6·8	75·0
S.-W.	Xungba	3	TE125/93	5·0	84·3
S.-W.	Xungba	3	TE126/93	7·1	106·3
S.-W.	Xungba	3	TE127/93	6·8	108·2
S.-W.	Xungba	3	TE131/93	7·0	100·5
S.-W.	Xungba	3	TE138/93	7·3	73·6
North Tibet					
N.-W.	Ashikule	1	912	4·3	179·8
N.-W.	Ashikule	4	K702	4·3	189
N.-W.	Ashikule	4	K703	4·0	221·8
N.-W.	Tienchuhai	4	K89G185	5·8	193·6
N.-W.	Tienchuhai	4	K89G186	4·1	220·8
N.-W.	Tienchuhai	6	K89G191	3·8	184·5
N.-W.	Tienchuhai	6	K89G192	3·4	213·0
N.-W.	Tienchuhai	6	K89G193	3·7	201·8
N.-W.	Tienchuhai	4	K89G200	4·4	198·3
N.-C.	Heshebei	4	KP47-2	4·1	196·3
N.-C.	Heshebei	4	KP47-5	4·4	201·3
N.-C.	Heshebei	4	Bb124	2·9	227·8
N.-C.	Heshebei	4	Bb121	2·7	224·1
N.-C.	Heshebei	5	Bq137	3·8	235·6
N.-C.	Kunlun	4	K9024	3·3	173·7
N.-C.	Kunlun	4	K9026	2·8	193·3
N.-C.	Kunlun	4	K9027	2·9	186·7
N.-C.	Kunlun	4	K9028	2·9	177·7
N.-C.	Kunlun	4	k9029	2·8	189·5
N.-C.	Kunlun	4	K9031	3·4	177·3
N.-C.	Kunlun	4	K9032	2·9	191·6

Data sources: 1, this study; 2, Williams *et al*. (2001); 3, Miller *et al*. (1999); 4, major element data from Turner *et al*. (1996), new ICP-MS data in this study; 5, major element data from Pearce & Mei (1988) and ICP-MS data from this study; 6, data from Turner *et al*. (1996). Samples with MgO $<2{\cdot}8$ wt % were excluded from the regressions. Samples T2A (Williams *et al*., 2001) and TE137/98 (Miller *et al*., 1999) were excluded from the southern regression dataset as there was evidence for the presence of mafic xenoliths in both samples. In the case of northern Tibet only samples from volcanic provinces of known age were included.

Table A2: Regression details for the northern Tibet dataset

Element	Regression against MgO			Regression against La and enrichment ratios					
	Slope	Intercept	r^2	Slope	Intercept	r^2	CFH_j	CFL_j	E
SiO_2	−2·24	65·17	0·37						
TiO_2	0·09	1·29	0·12	0·00	2·14	0·02	1·86	1·76	0·95
Al_2O_3	−0·70	17·52	0·54						
Fe_2O_3	0·85	4·25	0·43						
MnO	0·02	0·04	0·33						
CaO	0·79	3·69	0·11						
Na_2O	−0·03	3·84	0·00						
K_2O	0·31	3·07	0·27	0·00	4·87	0·00	5·17	5·27	1·02
P_2O_5	0·27	−0·02	0·46	0·00	2·40	0·18	1·72	1·48	0·86
Rb	13·54	90·18	0·08	0·39	94·97	0·04	161·87	185·73	1·15
Ba	403·29	537·36	0·75	3·94	2172·6	0·17	2857·4	3101·7	1·09
Th	1·88	23·38	0·01	0·33	−31·39	0·24	26·26	46·83	1·78
U	0·63	2·39	0·10	0·04	−0·78	0·20	5·30	7·47	1·41
Nb	0·00	41·59	0·00	0·07	56·18	0·13	68·91	73·45	1·07
Ta	−0·05	2·26	0·02	−0·01	3·25	0·21	2·12	1·72	0·81
K	0·31	3·07	0·27	0·00	4·87	0·00	5·17	5·27	1·02
La	22·06	66·62	0·47	1·00	0·00	1·00	173·66	235·61	1·36
Ce	44·00	116·89	0·51	1·77	28·96	0·94	336·11	445·67	1·33
Pb	2·45	23·04	0·17	0·14	8·92	0·41	34·05	43·01	1·26
Pr	6·21	8·77	0·60	0·19	7·63	0·84	41·15	53·11	1·29
Sr	363·69	−45·13	0·66	1·91	1757·7	0·03	2088·8	2206·9	1·06
P	0·27	0·0	0·46	0·00	2·40	0·18	1·72	1·48	0·86
Nd	23·90	23·55	0·66	0·63	42·27	0·64	151·11	189·93	1·26
Zr	−7·28	454·50	0·00	1·18	177·06	0·07	381·11	453·90	1·19
Hf	0·12	9·17	0·00	0·03	4·82	0·10	9·27	10·85	1·17
Sm	3·83	1·77	0·70	0·07	10·26	0·46	22·91	27·42	1·20
Eu	0·83	0·36	0·72	0·01	3·00	0·29	5·07	5·81	1·15
Ti	0·09	1·29	0·12	0·00	2·14	0·02	1·86	1·76	0·95
Gd	2·38	2·12	0·63	0·04	8·39	0·29	15·38	17·88	1·16
Tb	0·22	0·38	0·62	0·00	1·15	0·14	1·64	1·81	1·11
Dy	0·75	2·50	0·56	0·00	6·43	0·01	6·92	7·09	1·03
Y	2·65	15·37	0·42	−0·01	34·17	0·01	31·65	30·75	0·97
Ho	0·09	0·54	0·48	0·00	1·20	0·03	1·09	1·05	0·97
Er	0·16	1·52	0·26	0·00	3·05	0·07	2·53	2·34	0·93
Tm	0·01	0·24	0·09	0·00	0·44	0·19	0·32	0·28	0·86
Yb	0·06	1·45	0·06	0·00	2·62	0·14	1·94	1·70	0·88
Lu	0·00	0·22	0·01	0·00	0·38	0·15	0·27	0·23	0·86

slopes and intercepts were then used to calculate the concentrations of the element of interest at the index values of La (i.e. CFL_{La} and CFH_{La}) for the two sample datasets (CFL_j is the concentration of j at CFL_{La}; CFH_j is the concentration of j at CFH_{La}, where j denotes the element of interest). The ratio CFL_j/CFH_j is termed the enrichment ratio (E). The values of these parameters are also given in Tables A2 and A3, and their definition and calculation are explained in the main text and shown graphically

Table A3: Regression details for the southern Tibet dataset

Element	Regression against MgO		Regression against La and enrichment ratios						
	Slope	Intercept	r^2	Slope	Intercept	r^2	CFH_j	CFL_j	E
SiO_2	−2·38	73·0	0·7						
TiO_2	0·10	0·5	0·3	0·00	0·9	0·07	1·0	1·1	1·2
Al_2O_3	0·01	13·3	0·0						
Fe_2O_3	0·64	2·3	0·6						
MnO	0·01	0·1	0·3						
CaO	0·15	4·3	0·0						
Na_2O	0·06	1·9	0·0						
K_2O	0·31	4·5	0·30	0·01	5·4	0·12	6·0	6·6	1·1
P_2O_5	0·11	0·2	0·73	0·00	2·4	0·18	2·2	1·9	0·9
Rb	12·53	163	0·22	−0·21	487	0·00	474·6	460·3	1·0
Ba	353·05	170	0·60	9·67	1409	0·30	1972·0	2622·4	1·3
Th	29·28	−45	0·68	0·49	86	0·16	114·8	147·8	1·3
U	2·68	4·4	0·37	0·03	17·6	0·02	19·5	21·6	1·1
Nb	3·54	6·0	0·30	0·09	19	0·08	24·1	30·4	1·3
Ta	0·21	0·49	0·16	0·01	0·9	0·10	1·4	2·1	1·4
K	0·31	4·5	0·30	0·01	5·4	0·12	6·0	6·6	1·1
La	11·84	19·9	0·34	1·00	0·0	1·00	58·2	125·5	2·2
Ce	29·73	32	0·39	2·17	13	0·92	139·4	285·6	2·0
Pb	5·84	34·1	0·08	0·85	−8·3	0·50	41·3	98·6	2·4
Pr	4·76	0·3	0·53	0·27	4·7	0·93	20·1	38·0	1·9
Sr	81·18	295	0·37	−0·02	783	0·00	782·3	781·1	1·0
P	0·11	0·16	0·73	0·00	2·4	0·18	2·2	1·9	0·9
Nd	24·49	−16·8	0·57	1·12	28	0·74	93·5	169·1	1·8
Zr	67·55	34·6	0·52	2·22	238	0·32	367·5	516·6	1·4
Hf	1·92	0·9	0·41	0·07	5·7	0·27	10·0	15·0	1·5
Sm	4·63	−3·2	0·64	0·12	13·3	0·35	20·5	28·9	1·4
Eu	0·71	−0·4	0·73	0·01	3·0	0·13	3·5	4·1	1·2
Ti	0·10	0·50	0·31	0·00	0·9	0·07	1·0	1·1	1·2
Gd	1·97	1·75	0·62	0·07	7·4	0·51	11·4	15·9	1·4
Tb	0·16	0·4	0·48	0·01	0·9	0·37	1·2	1·7	1·3
Dy	0·47	3·1	0·36	0·02	4·3	0·21	5·3	6·5	1·2
Y	0·98	20·1	0·15	0·01	25·5	0·00	25·8	26·2	1·0
Ho	0·03	0·7	0·10	0·00	0·8	0·03	0·8	0·9	1·1
Er	0·07	1·8	0·11	0·00	2·1	0·01	2·2	2·3	1·0
Tm	−0·01	0·3	0·03	0·00	0·3	0·02	0·3	0·3	0·9
Yb	−0·04	1·9	0·03	0·00	2·1	0·10	1·8	1·5	0·8
Lu	0·00	0·3	0·02	0·00	0·3	0·06	0·3	0·2	0·9

in Fig. 12. The E values are then modelled using modified conventional melting equations and the details of this process are given in the main text.

The details of the peridotite melting models including the mineral assemblages and melting modes are given in the main text. In Table A4, the partition coefficients used are listed. In many cases, there were several possible partition coefficients to choose from, and it was not possible to find a single set of partition coefficients that originated from the same set of experiments, or the same natural sample. In the selection of partition coefficients, we chose those most appropriate

Table A4: Partition coefficients used in modelling

Mineral:	olivine	orthopyroxene	clinopyroxene	amphibole	rutile	phlogopite	garnet
Data source:	1, 2	1, 2	1, 2, 3	1, 4, 5	6, 7, 8	1, 5, 9, 10	2, 3
Rb	0·0003	0·0002	0·0004	0·22	0·0076	4·7588	0·0002
Ba	0·000005	0·000006	0·00018	0·278	0·0043	3·9139	7E − 12
Th	0·000007	0·00002	0·0021	0·0039		0·0014	0·0021
U	0·000009	0·00004	0·001	0·0041	0·0011	0·011	
Nb	0·00005	0·0013	0·0067	0·05	52·6	0·0853	0·00054
Ta	0·00005	0·0025	0·022	0·074	99·5	0·1069	0·0025
K	0·00002	0·0001	0·001	1·36		1·5	0·013
La	0·0002	0·0008	0·057	0·039	0·0055	0·0004	0·0014
Ce	0·00007	0·0016	0·12	0·067	0·087	0·0007	0·0029
Pb	0·0003	0·0014	0·0075	0·019		0·019	0·005
Pr	0·0003	0·0032	0·2	0·1045	0·04775	0·0013	0·0083
Sr	0·00004	0·0012	0·066	0·376	0·036	0·0879	0·0023
P	0·1	0·03	0·05		0·05		0·15
Nd	0·0003	0·0056	0·33	0·142	0·0085	0·0019	0·03
Zr	0·001	0·032	0·18	0·124	3·07	0·0151	0·12
Hf	0·0029	0·06	0·31	0·331	4·61	0·0053	0·07
Sm	0·01	0·015	0·58	0·188	0·00164	0·0045	0·18
Eu	0·0005	0·03	0·77	0·351	0·0037	0·0095	0·33
Ti	0·015	0·086	0·4	0·717	11	2·8671	0·6
Gd	0·0015	0·034	0·77	0·368	0·0037	0·0096	0·75
Tb	0·0021	0·054	0·95	0·387	0·0069	0·0139	1·5
Dy	0·0027	0·077	1·1	0·406	0·0101	0·0182	2·4
Y	0·0082	0·095	1·1	0·333	0·007	0·036	3·9
Ho	0·01	0·1	1·1	0·3295	0·01	0·0187	3·7
Er	0·009	0·12	1·1	0·326	0·01	0·0192	4·4
Tm	0·0165	0·17	1·15	0·3375	0·01	0·0261	5·45
Yb	0·024	0·22	1·2	0·349	0·0093	0·033	6·5
Lu	0·024	0·22	0·98	0·246	0·016	0·0395	6·7

Spinel *D* values were taken as 0·01 following McKenzie & O'Nions (1991). Data sources and comments on choice of partition coefficients: (1) Halliday *et al*. (1995); (2) Brunet and Chazot (2001), the only currently available partition coefficients for P in mafic systems. (3) Green *et al*. (2000), a consistent set of REE partition coefficients for clinopyroxene and garnet in a hydrous system. (4) Dalpe & Baker (1994). (5) LaTourette *et al*. (1995). (6) Foley *et al*. (2000), the most consistent set of REE partition coefficients for rutile. (7) Jenner *et al*. (1994), the most consistent set of Nb and Ta *D* values in rutile [compare Foley *et al*. (2000), who gave only Nb *D* values]. (8) Anderson & Greenland (1969), the only available partition coefficient for P in garnet. The partition coefficient for P in ilmenite from this paper is applied to rutile in this study, as there are no published partition coefficients for P in rutile available at present. (9) Gregoire *et al*. (2000), the most complete REE compilation for phlogopite. (10) Foley *et al*. (1996), the partition coefficients for Nb and Ta in phlogopite are used here as they are consistent with the majority of other studies. However, the value for Nb is very low compared with that of Gregoire *et al*., 2000 (3·9). Unfortunately, there is no corresponding Ta partition coefficient given by Foley *et al*. (1996) to allow a direct comparison to be made.

for this study. The criteria we applied were that: (1) the partition coefficients used should be calculated from the mineral compositions of natural peridotites, where possible; (2) these partition coefficients should be those that are the most consistent with other natural or experimental studies; (3) partition coefficients for elements that are used together in geochemical modelling should be as consistent as possible and ideally from the same source. Examples are the REE and the Nb and Ta pair. The data sources for all partition coefficients are listed in Table A4; the full references are given in the reference list of the main paper.